UNIVERSITY OF COPENHAGEN
FACULTY OF SCIENCE

MASTER'S THESIS

ANDERS PAASKE DRACHMANN

DUST PRODUCTION IN LATE-TYPE HIGH-MASS STARS

THE SIGNIFICANCE AND CONTRIBUTION TO THE ISM

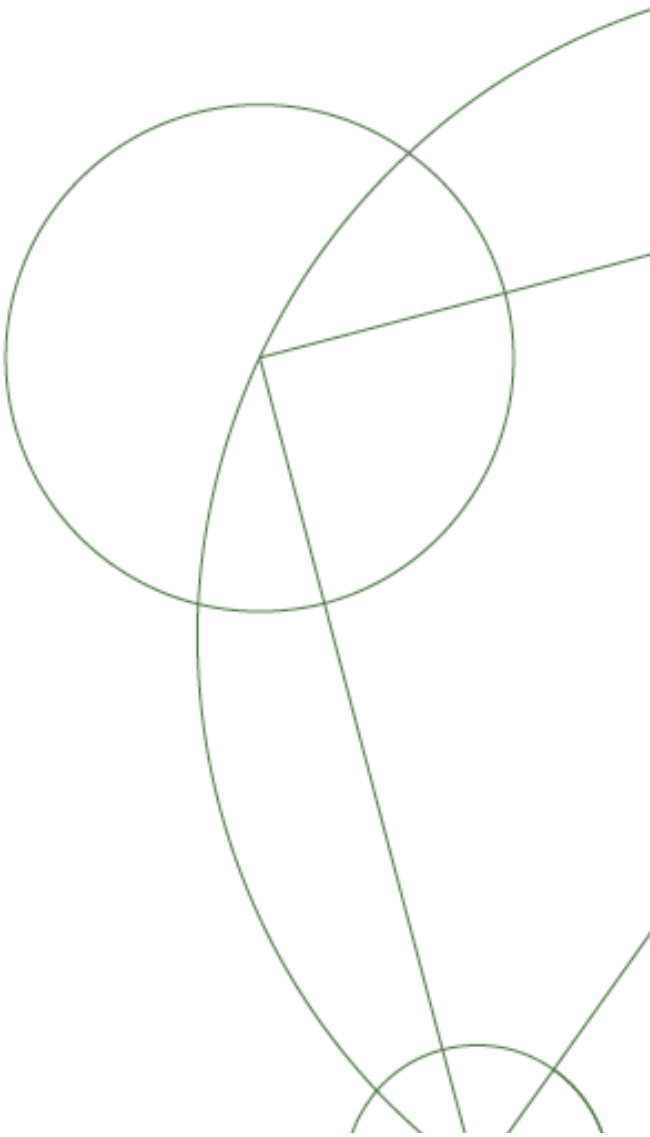

SUPERVISOR: ANJA C. ANDERSEN
DARK COSMOLOGY CENTER, NIELS BOHR INSTITUTE
DATE OF SUBMISSION: MARCH 1st, 2016

Dark Cosmology Centre
Niels Bohr Institute, University of Copenhagen
Juliane Maries Vej 30
2100 Copenhagen Ø
Denmark

Phone: +45 353 25 991
Fax: +45 353 20 573
Email: dark_info@dark-cosmology.dk

Abstract

Cosmic dust, that dominate the solid phase of matter in the universe, not only shapes what we observe – observations of star formation, quasars, supernovae and hence dark energy –are all profoundly affected by dust, but the presence of dust also dictates the formation of low- and high-mass stars, the making of planets, and the formation of molecules in space. Yet, we do not know the formation site of most dust. Recent observations by infrared (IR) space telescopes have made it easier to investigate probable production sites of dust such as supernova remnants (SNR) which show promising results of dust production. However, recent observations and theoretical studies suggests that the reverse shock from the supernova (SN) might be destroying significant amounts of the dust.

Lately, a large population of dusty shells around high mass stars in our Galaxy has been found, which indicate that high mass stars could be contributing to the overall dust budget as well. From a sample of 10 *Spitzer* identified high mass stars with circumstellar dust shells I use new photometric data from the *Herschel Space Observatory* to determine their spectral energy distribution (SED). By fitting each SED with a two-component black-body function I find the dust masses and temperature of the shells using silicate- and carbon-based models. With a dust minimum of 0.1 $M_{\odot}$ per SN to explain for the majority of dust produced in early galaxies, the results suggests that late-type high mass stars indeed could be able to produce noticeable amounts of dust. It seems that high mass stars could be an important contributor to the dust budget of the ISM, perhaps on the same level as SNRs.

Acknowledgments

First of all I would like to thank my supervisor, Anja C. Andersen, for taking me under her wings as her master student and offering an interesting, challenging project. For providing constant and valuable guidance and for keeping my eyes on the ball. Despite her busy schedule Anja has always managed to find the time to see me, whether it be regarding academic questions or conversations about everything.

Secondly I would like to thank the staff and students at the Dark Cosmology Center for providing a good work environment. A thank you should also go to DARK itself and the Niels Bohr Institute for making the facilities available, but most of all for the easy and very much important access to coffee.

A special thanks to the boys from the *Dark Matter Crew* without whom I probably would not have made it this far. The academic and highly professional collaboration since the first year project and throughout the years has been invaluable, as well as all the time shared away from the studies.

I would also like to thank Johan Fynbo and Darach Watson for always making themselves available to answer whatever questions I might have had and for engaging interesting and educational conversations.

Thanks to Anders Hammer Holm, Søren Borg Nielsen and Mikkel Theiss Kristensen for helping me remember that lunch and coffee breaks are important and for keeping me company during these.

Last but not least I would like to thank my lovely family and girlfriend for never loosing their faith in me and to always be there when I needed it the most.

Contents

List of Figures

List of Tables

List of Acronyms

AGB	Asymptotic Giant Branch
APT	Aperture Photometry Tool
BSG	Blue Supergiant
cLBV	candidate Luminous Blue Variable
CCSN	Core Collapse Supernova
CSM	Circumstellar Medium
FIR	Far-infrared
HIPE	*Herschel* Interactive Processing Environment
IR	Infrared
LBV	Luminous Blue Variable
LTE	Local Thermodynamic Equilibrium
MIPS	Multiband Imaging Photometer for *Spitzer*
PACS	Photodetecting Array Camera and Spectrometer
PISN	Pair-Instability Supernova
PN	Planetary Nebula
RLOF	Roche-Lobe Overflow
RSG	Red Supergiant
SED	Spectral Energy Distribution
SN	Supernova
SNR	Supernova Remnant
SPIRE	Spectral and Photometric Imaging Receiver
UV	Ultra Violet
WR	Wolf-Rayet
YSG	Yellow Supergiant
ZAMS	Zero Age Main Sequence

To my beloved grandmother

Anna Thordahl Drachmann

1 Introduction

Dust. For the past year when people have asked me about my thesis project, the usual reaction to cosmic dust being my topic has been: *"Dust? We've got a lot of that at home"*. But it is not just in our everyday lives that we see dust everywhere. In astronomy dust is also observed in almost any direction and it has a grave impact on how we see the universe. All that astronomers have to work with is light, which is blocked, absorbed, scattered and re-emitted by dust. And since we do not have a cosmic vacuum cleaner at this point to remove it, it's important to understand the properties and features as well as the formation sites of dust. In that way we can better study the rest of space.

But dust is not just important because of its interfering nature. Dust also plays a significant role in the matter of star formation which depends on efficient cooling, provided by dust and molecular gas. Formation of planets are also critically dependent on dust and it's properties. It has a grave impact on how supernova (SN) explosions expand and how much dust they destroy and create. Dust is formed within and drives steady stellar wind outflows of old stars of lower mass as well as in violent outbursts in the late stages of high mass stars. Some high mass stars experience extreme mass-loss in short episodic events where high amounts of dust and gas are shed away in explosions. Some of these event are sometimes so luminous that they are mistaken to be a supernova, but are later observed still to have it's progenitor star. The mechanisms and

triggers behind these events are still unknown, and raises great questions in high mass stellar evolution.

For years astronomers thought that evolved, old low mass stars were responsible for producing most of the dust that we see in the Galaxy. It takes some billions of years for these stars to reach the phase where they start to shed material on a slow but steady basis. But recent observations of very early galaxies (Bertoldi et al., 2003; Maiolino et al., 2004) with ages less than 1 Gyr show large amounts of dust which makes it unlikely to have originated from low mass stars, since they have not had enough time to reach the end stages required. This calls for a more short term solution which have led astronomers to investigate supernovae and supernova remnants (SNR) as dust production sites. These do in fact seem to be promising candidates of quick dust injection but new observations (Lau et al., 2015; Lakićević et al., 2015) as well as theoretical studies (Bianchi and Schneider, 2007; Nozawa et al., 2007) show that the supernova explosion might destroy too much dust to be able to account for the amount we see.

Recent developments in infrared telescopes and instruments have given us better opportunities to study dust in the infrared part of the spectrum. Namely *Herschel* Space Observatory and the *Spitzer* Space Telescope, but also the ground based ALMA telescope in the Atacama desert. Recently, new observations of massive stars with dusty shells have been made (Gvaramadze et al., 2010; Wachter et al., 2010) where about ~150 stars were identified as part of a general survey of the Milky Way plane with *Herschel*. It was not at the time expected that the survey would contain such a relatively large fraction of dust enshrouded high mass stars, indicating that massive stars with circumstellar dust shells are more frequent than initially thought.

This thesis has been dedicated to taking a closer look at dust formation around late-type high-mass stars. By looking at a sample of 10 stars, which show signs of circumstellar dust shells (also referred as dust puffs), I investigate the amount of dust as well as the dust temperature. The aim is to show whether or not high mass stars might be a noteworthy contributor to the overall interstellar medium (ISM) dust budget in galaxies. Thereby shedding light on the current dust problem at high redshift. In the following section I will introduce some of the general quantities and the theoretical background. Sect. 3 concerns the data and my thoughts behind the target selection. In Sect. 4 I present the methods I use to obtain my results, which are presented in the following section (Sect. 5). In Sect. 6 I will discuss how the results are affected by various choices I have made and compare my results with similar studies. Sect. 7 contains a short summary and my final conclusions as well as a paragraph about how this project could proceed with new satellite data being released this summer of 2016.

Figure 1.1: Image of the M16 Eagle Nebula (*Pillars of Creation*) taken by the *Hubble Space Telescope* in visible and infrared. Credit: NASA, ESA, and the Hubble Heritage Team (STScI/AURA).

"I always thought they [stars] were balls of gas burning billions of miles away."

– Pumbaa, *The Lion King*.

2

Theoretical Background

In the upcoming section I will introduce some basic concepts and quantities that I will use throughout the thesis. Sect. 2.2 will shortly address the early evolutionary stages of stars (Sect. 2.2.1) as well as the later evolutionary stages (Sect. 2.2.2) emphasizing high mass stars. In Sect. 2.2.3 I will take a quick tour through the astronomical zoo and explain some of the basic features of the stellar phases that high mass stars encounter at the end of their life and what fate they face in the end as supernovae (Sect. 2.2.4). Mass loss during the stellar evolution and some basic properties of dust will be described in Sect. 2.3 and 2.4, respectively. The following sections are in general based on the books of Longair (2011), Draine (2011), Prialnik (2011) and Christensen-Dalsgaard (2008) as well as an annual review by Smith (2014).

2.1 Spectral Classes

Depending on the stars spectral characteristics the star is classified with a spectral type. This *spectral class* is an indication of the star's temperature following the letter system from hottest to coldest *O, B, A, F, G, K* and *M*. Each of these letters are accompanied by a single digit from 0 to 9 (also hot to cold), meaning a F5 star is hotter than a F7, but cooler than a A6. This is the so-called *Morgan-Keenan* (MK) system. The system

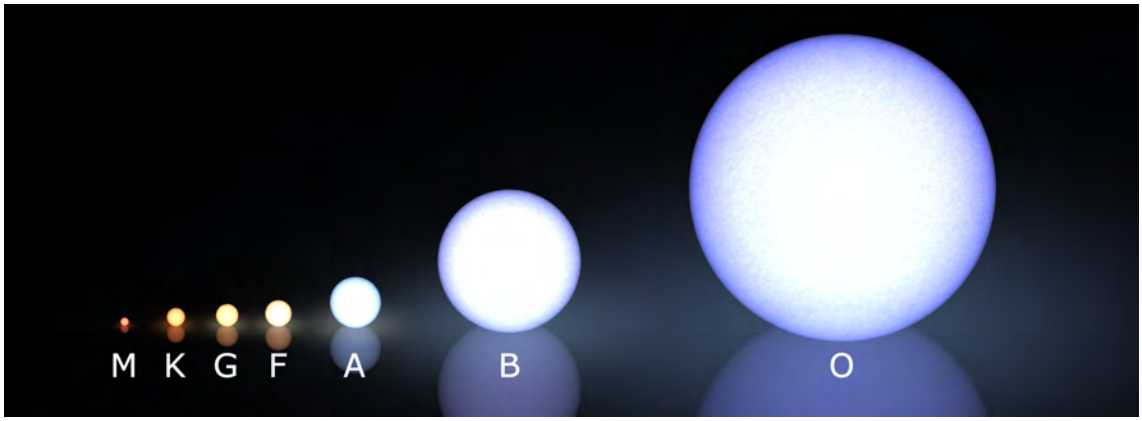

Figure 2.1: Illustration of the Morgan-Keenan spectral class system with respective sizes and colors. The temperature increases with size to the right. Image Credit: Rursus (Own work) [https://upload.wikimedia.org/wikipedia/commons/8/8b/Morgan-Keenan_spectral_classification.png].

has been expanded to include a roman number in the end to denote the current "state of evolution", e.i. *III* means the star is a *Giant* and *V* stands for a main-sequence star (Sect. 2.2.1). The Sun is classified as a G2V star, indicating it is on the main-sequence. Since the most massive and largest stars are the ones with highest temperatures, the spectral class also gives an indication of the size of the star. An illustration of this is provided in Fig. 2.1.

The stars are classified from their spectra. Depending on the type of star, i.e. what temperature the star has, it emit light mainly at certain wavelengths. Hotter stars emit light with shorter wavelengths (higher energies) and so the spectrum of an O star is dominating in the ultraviolet (UV) region. With lower temperature the main photon energy decreases and the spectrum peak "moves" toward longer wavelengths. This is illustrated in Fig. 2.2, where the spectra of different spectral classes are shown in the left and middle plot.

The right side of the figure is a *Hertzsprung-Russell* (HR) diagram. The HR-diagram is a good indicator of what stage of evolution the star is in. The various subclasses are indicated on the plot as well (Ia/Ib/II/III/BI/V). In this case it is shown with magnitude[1] vs. the color index (B-V). Another, and equivalent, way is to plot the luminosity vs. the effective temperature, since the magnitude is an indication of how much energy is emitted by a star and the color index is an indication of the temperature. The

[1]The magnitude system dates back about 2000 years and classifies the stars by it's apparent brightness. The brighter the star, the higher magnitude (but lower value, which can be confusing at times).

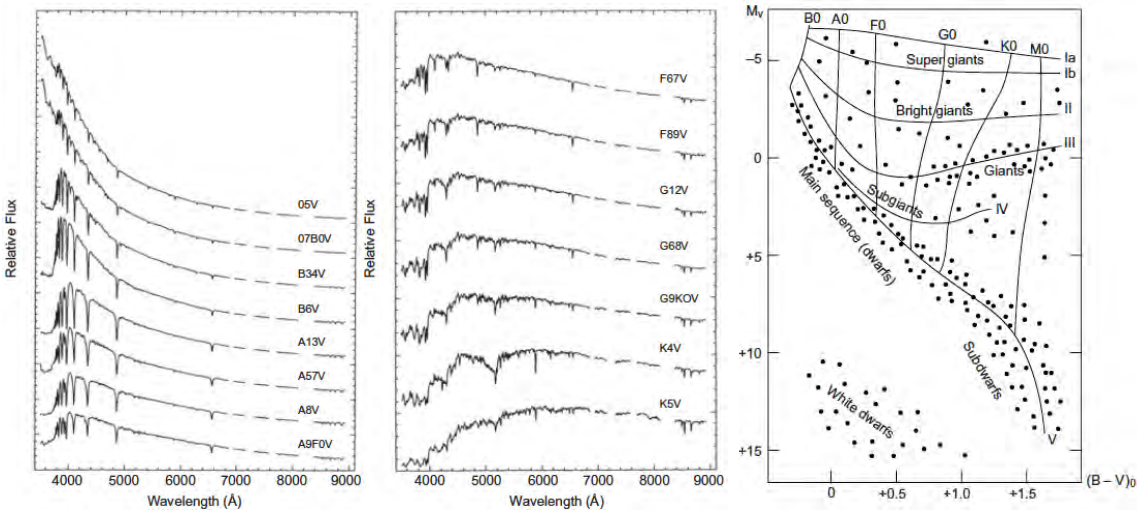

Figure 2.2: Left and middle: Spectra from different spectral classes. The spectra get more and more red the smaller and cooler the stars get. Right: HR-diagram showing the various subclasses such as main-sequence (V), subgiants (IV), giants (III), bright giants (II), supergiants (Ia and Ib) and white dwarfs as well as the spectral classes. From Longair (2011).

luminosity, which is the total energy emitted per unit time (or power), is given as:

$$L = 4\pi R^2 \sigma T_{\text{eff}}^4, \tag{2.1}$$

where R is the star's radius, σ is the *Stefan-Boltzmann* constant and T_{eff} is the effective temperature. That means the temperature of a black-body of the same radius as the star emitting the same luminosity. Since stars are not perfect black-body objects this is an approximation providing the temperature at the bottom of the stellar photosphere.

Another useful quantity, I will be using later on, is the *flux density*, which is the power per unit area. It is defined as:

$$F_\nu = \frac{L_\nu}{4\pi R^2}. \tag{2.2}$$

Typically, when dealing with the *infrared* (IR) part of the spectrum, the flux density is given in the units of Jansky (Jy) which is defined as:

$$1\,\text{Jy} = 10^{-26}\frac{\text{W}}{\text{m}^2\,\text{Hz}} = 10^{-23}\frac{\text{erg}}{\text{s}\,\text{cm}^2\,\text{Hz}}. \tag{2.3}$$

2.2 Stellar Evolution

The life of a star is a very complex story. Especially when it comes to high mass stars. The most important factor in stellar evolution is exactly the mass. The smaller the star the less eventful is it's life, although a lot longer. In order to remain in hydrostatic equilibrium the massive stars need to keep a higher radiation pressure compared to the smaller stars to prevent gravitational collapse. They therefore use more "fuel" (i.e. they keep a higher fusion rate of hydrogen) on a shorter time-scale and runs out of hydrogen a lot faster. Small stars, like the sun, therefore live some billion years whereas a star with 20 times the mass of the sun only lives some ten times a million years.

2.2.1 Main Sequence

After the star has established its hydrostatic equilibrium through fusion of hydrogen it now begins the longest evolutionary phase of its lifetime. This phase is called the *Main Sequence*. The main sequence is the phase where the star is maintaining its radiation pressure through hydrogen burning. Small stars burn hydrogen through the so-called PP-chain (proton-proton) reaction:

$$4\,{}^{1}\mathrm{H} \rightarrow {}^{4}\mathrm{He} + 2\mathrm{e}^{+} + 2\nu_{\mathrm{e}}, \tag{2.4}$$

where 4 hydrogen fuses into 1 helium and releases the additional 2 positrons and 2 electron neutrinos. This process is the dominant reaction for stars with a central temperature of less than 1.7×10^{7} K. For larger stars, who has much higher temperatures than the smaller ones due to the higher gravitational pressure, the dominant nuclear process is the CNO cycle (Carbon-Nitrogen-Oxygen) in which they form ^{4}He through heavier nuclei and proton capture. One of the CNO-cycles looks as follows:

$$\begin{aligned}
{}^{12}\mathrm{C} + \mathrm{p} &\rightarrow {}^{13}\mathrm{N} + \gamma \\
{}^{13}\mathrm{N} &\rightarrow {}^{13}\mathrm{C} + \mathrm{e}^{+} + \nu_{\mathrm{e}} \\
{}^{13}\mathrm{C} + \mathrm{p} &\rightarrow {}^{14}\mathrm{N} + \gamma \\
{}^{14}\mathrm{N} + \mathrm{p} &\rightarrow {}^{15}\mathrm{O} + \gamma \\
{}^{15}\mathrm{O} &\rightarrow {}^{15}\mathrm{N} + \mathrm{e}^{+} + \nu_{\mathrm{e}} \\
{}^{15}\mathrm{N} + \mathrm{p} &\rightarrow {}^{12}\mathrm{C} + {}^{4}\mathrm{He}.
\end{aligned} \tag{2.5}$$

Figure 2.3 compares the nuclear energy generation rate of the p-p chain and CNO

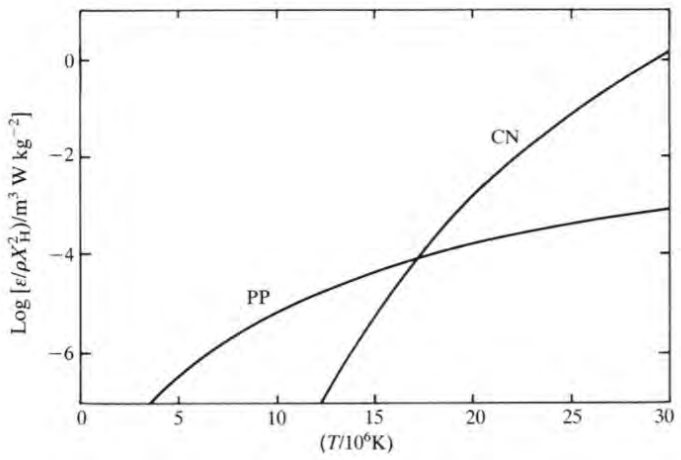

Figure 2.3: The overall energy generation rates for the p-p chain and the CNO cycle as a function of temperature. From Longair (2011).

cycle as functions of the temperature. As mentioned before, the p-p chain dominates at the temperatures below T$\simeq 1.7 \times 10^7$, whereas the CNO cycle dominates at temperatures above. The energy generation rate for the p-p chain goes as $\varepsilon_{pp} \propto T^4$ and the corresponding energy generation rate for the CNO cycle goes as $\varepsilon_{CNO} \propto T^{17}$.

2.2.2 Post Main Sequence

When the hydrogen fusion stops the hydrostatic equilibrium disappears and an overall contraction of the star begins. The released potential energy is somewhat used to heat up the central parts of the star. A hydrogen burning shell is established at some point with the increasing temperature, and the so-called shell-burning law takes effect: when the nuclear processes in a shell is dominant the inner parts will contract and the outer parts will expand. This continues until the core starts to burn helium efficiently. Depending on the the mass of the star this starts sooner or later. Low and intermediate mass stars take longer time to reach this point and may encounter a *degenerate* core, where the electron pressure can outbalance the force of gravity, before the helium burning takes over.

This is not the case for the high mass stars which reaches the temperatures needed for further nuclear fusion before the core becomes degenerate. The same is the case for the nuclear processes that follows helium burning. The result is an onion-shaped structure with multiple shells. A schematic of the structure is shown in Fig. 2.4, where the composition and nuclear reactions are shown for each layer along with some typi-

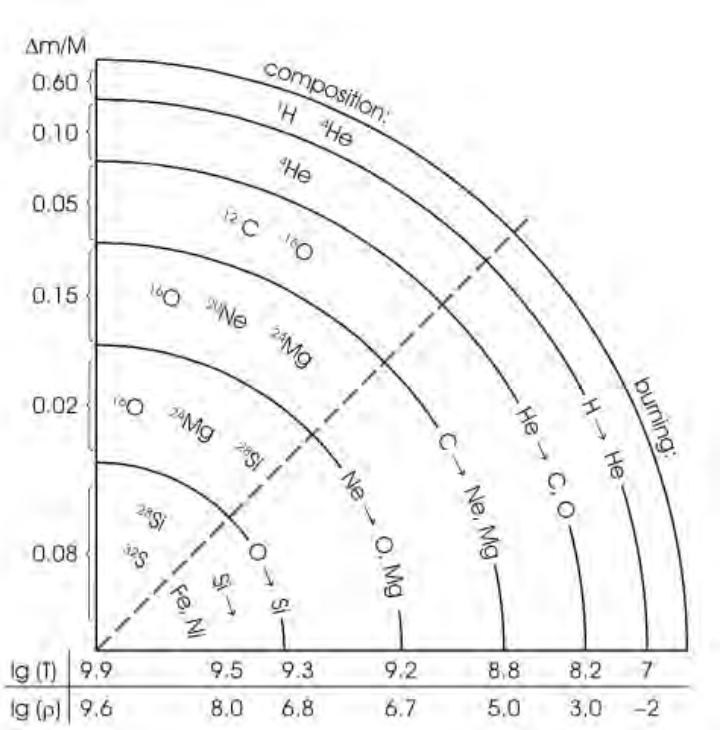

Figure 2.4: A schematic illustration of the onion-shell structure of an evolved high mass star. Pressure and temperature are indicated horizontally and the mass fraction vertically (some typical values), with the composition and fusion process indicated on each layer. Not to scale. From Christensen-Dalsgaard (2008).

cal values for pressure ($\mathrm{g\,cm^{-3}}$), temperature (K) and stellar mass fraction.

The fusion processes will continue until the final reaction that creates iron is reached. Reactions beyond this point is no longer desirable since they need energy to fuse instead of releasing energy. This is due to the fact that Fe (iron) has the highest binding energy per nucleon. This stage of evolution, or these processes, are referred to as the *silicon burning* phase, which can be misleading.

2.2.3 Later Stages

By now, there are a lot of different types of phases in the later evolutionary stages of massive stars. Depending on stellar winds (mass-loss, Sect. 2.3), stellar companions and – of course – the mass, the star can undergo a wealth of different phases and maybe even multiple times. Typically, after consuming all the hydrogen within its core, the star expands to many times it's regular radius and becomes a *red supergiant* (RSG), *blue supergiant* (BSG) or a *yellow supergiant* (YSG), depending on how much it expands.

SUPERGIANTS – After the termination of hydrogen core burning and the shell burning has started, the star expands as a consequence of the shell law. The RSGs are some of the coolest evolved massive stars, whereas the BSG are much hotter. The rare and short lived phase of the YSG is somewhat in between. Typically, the BSGs are newly evolved from the main sequence and have very high luminosities and high mass loss. They tend to transit to the LBV phase, but some (in the lower end of the mass spectrum) continues to expand and become RSGs, moving quickly through the YSG phase on the way. The RSGs can, if massive enough, blow away some of the outer layers, evolve back into a BSG and possibly, in time, onwards to a *Wolf-Rayet* (WR) star. This can happen a number of times, depending on the mass of the RSG, in a so-called blue loop. Because of the shed atmospheres the stars can sometimes be self-obscured by dust, which reddens the stars even more. An example of a RSG is the well-known and famous *Betelgeuse* shown in the left figure of Fig. 2.5.

WOLF-RAYET – If the stellar wind are strong enough the star are able to shed the outer most layers consisting of hydrogen. This type of star is the Wolf-Rayet star and their spectra are mainly dominated by helium (which is the next layer below hydrogen) and other heavier elements such as carbon, nitrogen or oxygen. This leads to further three subcategories depending on the presence and/or absence of various spectral lines: the ones with dominant nitrogen lines and carbon lines are classified as WN and WC, respectively. The last class denoted WO is distinguished from the WC class if oxygen lines are more pronounced than the carbon lines, although they might be comparable. All of these classes are further denoted with a number depending on specific characteristics of the emission lines.

LUMINOUS BLUE VARIABLE – An unstable variant of the supergiant is the *luminous blue variable* (LBV). This type of star has many variations both photometric and spectroscopic due to violent outbursts and larger eruptions, which happen infrequently. These outbursts and strong stellar winds are the cause of the formation of surrounding nebulae of gas and dust. As the name indicates LBVs are more luminous, during their outbursts, than most stars. The initial masses are still not known, but their luminosities suggests masses greater than 25 $M_\odot$ when comparing to single-star evolutionary tracks (Smith et al., 2003). Some of the most luminous LBVs are about 10^6 times more luminous than the Sun and have masses

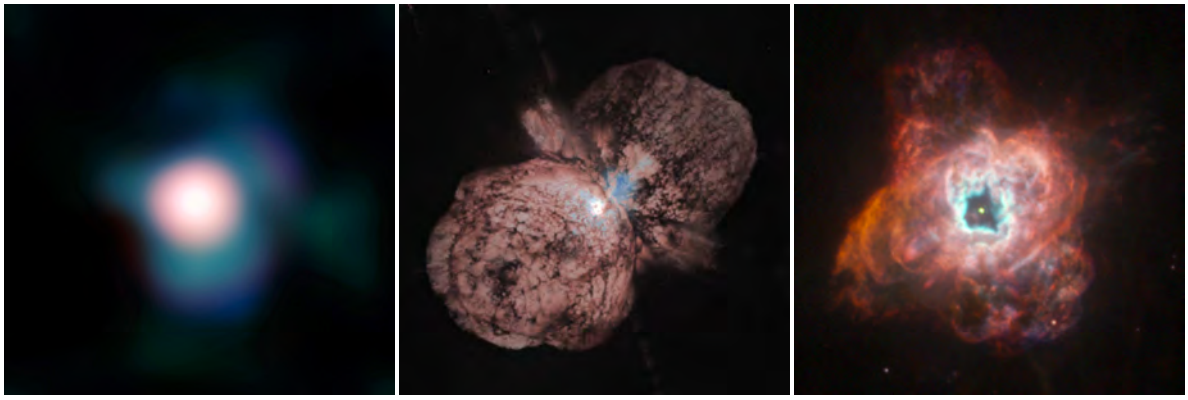

Figure 2.5: Examples of later evolutionary stages of massive stars. Left: Betelgeuse, a well known red supergiant. Credit: ESO/P. Kervella. Middle: Eta Carinae, LBV. Credit: Jon Morse (University of Colorado)/NASA Hubble Space Telescope. Right: NGC5315, Wolf-Rayet star. Credit: NASA/ESA/Hubble Heritage Team (STScI/AURA). Pay in mind the size difference of the objects. As a star Betelgeuse corresponds only to a small central point of Eta Carinae and NGC5315.

of about 100 $M_\odot$. Because the outburst and winds shed the outer layers containing mostly hydrogen the stars show higher amounts of helium and nitrogen. Candidates for the LBV class (cLBV) are typically stars of spectral type WN9 or early B supergiants, but these candidates have not yet shown the signature variability. They are observed with some spectroscopic features as LBVs as well as being surrounded by massive dust shells. Sometimes the eruptions are so violent that some LBVs have been confused with supernovae, simply because of the significant increase in luminosity. These are referred to as supernova imposters.

In general, the evolutionary track of a high mass star depends very much on the initial mass, as always, but also to a large extent on how much mass it succeeds to get rid off during the various phases. An example of an evolutionary scheme for a 100 $M_\odot$ star could be:

$$\text{O star} \rightarrow \text{Of/WNH} \rightarrow \text{LBV} \rightarrow \text{WN} \rightarrow \text{WC} \rightarrow \text{SN Ibc.} \tag{2.6}$$

This path is slightly different for a star which has an initial mass between 30 $M_\odot \leq M_{ZAMS} \leq 40\ M_\odot$ (Guha Niyogi et al., 2014):

$$\text{O star} \rightarrow \text{BSG} \rightarrow (\text{RSG}) \rightarrow \text{LBV} \rightarrow \text{WR} \rightarrow \text{SN.} \tag{2.7}$$

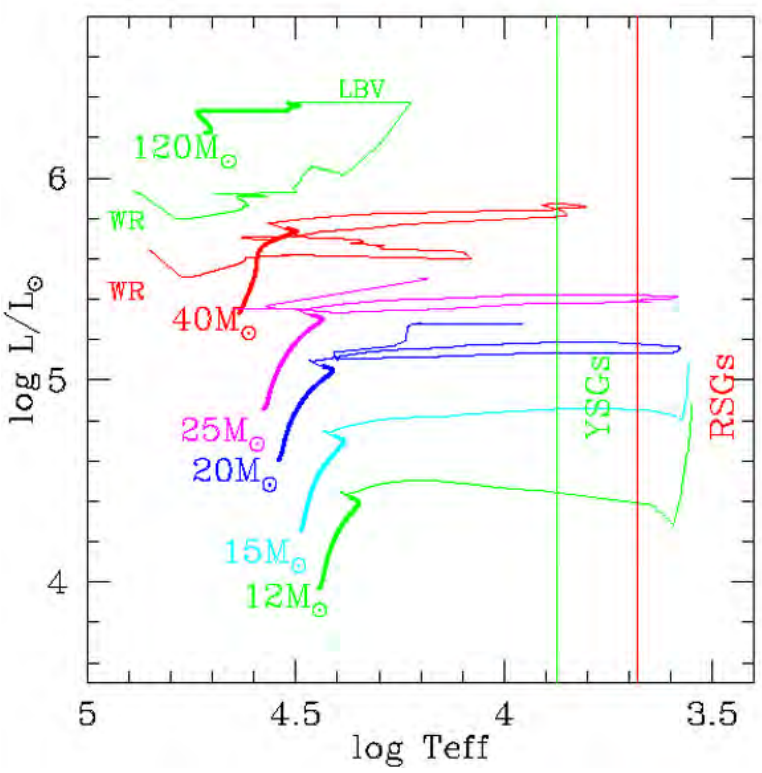

Figure 2.6: HR-diagram showing examples of evolutionary tracks of solar metallicity (Z = 0.014) high mass stars with varying M_{ZAMS}, which are shown at the beginning of each track. The thick part of the lines indicates the main sequence. The general regions of RSGs and YSGs has been labeled. From Massey (2013).

Figure 2.6 shows how the evolutionary tracks of high mass stars can look with varying M_{ZAMS} in a HR-diagram.

2.2.4 Supernovae

Ultimately the star dies. But how depends on the initial mass. Intermediate mass stars with initial masses of about $4-8\ M_\odot$ continues their nuclear fusion in the core until they reach carbon or oxygen (sometimes silicon), where they shed their outer layers through strong stellar winds. These layers form planetary nebulae and the remnant becomes a white dwarf.

Heavier stars will in turn end their lives as supernovae. As their nuclear burning reaches the final stage of an iron core, the burning stops and the outward pressure disappears, leading to a collapse of the remaining outer layers which takes less than a second. The contraction of the iron core raises the temperature. At some point iron

starts to suffer from photodisintegration:

$$^{56}\mathrm{Fe} \rightarrow 13\,^{4}\mathrm{He} + 4\mathrm{n} \tag{2.8}$$

which absorbs energy, removing even more of the outward pressure. In turn, the photons become more and more energetic, until they are able to break up helium into protons and neutrons which absorbs even more energy. The continuing collapse leads to even higher density until free protons are able to capture free electrons and turn into neutrons.

The removal of energy (and decreasing number of particles) results in a higher drop in pressure. At some point the neutron gas becomes degenerate, which creates a pressure sufficient enough to stop the collapse. The core expands slightly, like when a rubber ball have been squeezed, and creates a shock wave going out through the outer material of the star, along with a high neutrino pressure created from weak interactions of protons locked in the iron nuclei. The slight expansion releases the neutrinos which, due to extreme density, can provide a pressure that combined with the blast wave has enough energy to send the remaining mass out in a supernova, leaving behind a compact object in the form of a neutron star or a black hole.

The supernova types are divided into two main groups: those without and those with hydrogen Balmer lines in the optical spectrum when the light emission peaks. These two groups are named Type I (hydrogen absence) and Type II (hydrogen present). This depends on whether or not the progenitor star (the star which later on explodes as the supernova) have shed it's outer envelopes of hydrogen. They are furthermore given a letter depending on more specific characteristics in each main group.

TYPE I – The supernova **Type Ia** is a very special type of supernova since this is the only type where the explosion is set off by a thermal runaway reaction. Type Ia SNe happens in stellar binary systems where a carbon-oxygen rich white dwarf reaches the Chandrasekhar limit[2] through mass accretion from it's stellar companion. This mass accretion raises the temperature enough to ignite carbon fusion before it collapses and explodes. The **Type Ib** is typically associated with Wolf-Rayet stars, specifically WC types, which still have atmospheres containing helium. The specific feature of the Ib SN is a neutral helium line at 587.6 nm in the spectrum. This type of SN is caused by the core of the star collapsing, hence being a *core collapse supernova* (CCSN). **Type Ic** is almost identical to Ib but show

[2]Which in this case is about 1.4 $M_\odot$ (Longair, 2011).

weak or no presence of helium in the spectrum, making it likely to have evolved further to a WO star before collapsing.

TYPE II – All of the Type II supernovae are core collapse supernovae (CCSN). Their subcategory are partly determined by the emissions lines but also by the shape of the light curve. A **Type IIP** has a significant *plateau* in its light curve after peak emission, where as a **Type IIL**'s is decreasing linearly. The **Type IIn** SN is characterized by narrow emission lines compared to the otherwise broad ones of Type II SNe, and **Type IIb**'s spectre looks like a standard Type II's at early times but then later on resembles that of a Type Ib/Ic.

REMNANTS – All the material that is left after the explosion, i.e. the gas and dust, constitute the supernova remnant (SNR). The material is heated by the shock wave produced by the supernova which also send the material on an outward trajectory. The shock slows down as it sweeps up more and more of the ambient medium, and in turn creates a reverse shock which reheats the material inside of the initial shock wave position.

Table 2.1 from Smith (2014) shows the different SN types with their most likely associated progenitor star. The initial mass of the star, referred to as the *zero age main sequence mass* (M_{ZAMS}) and the mass-loss rate ($\dot{M}$) are also indicated along with the terminal velocity of the stellar winds (V_∞). Notice the variation in V_∞ which span from a $10\,\mathrm{km\,s^{-1}}$ for RSGs up to $1000\,\mathrm{km\,s^{-1}}$ for LBVs and WRs.

Some stars, with progenitor masses exceeding $130\,\mathrm{M_\odot}$, ends their lives as so-called *pair-instability* SNe (PISNe). In these types of SNe the photons get so energetic that they are able to drive the pair production of electrons and positrons:

$$2\gamma \rightarrow \mathrm{e}^- + \mathrm{e}^+. \tag{2.9}$$

As the energy of the gamma rays increase, more and more are removed through the pair production. This process removes so much of the thermal pressure and leads to a partial collapse. This will in turn greatly accelerate the burning resulting in a thermonuclear runaway explosion that obliterates the core without leaving a black hole remnant behind.

Figure 2.7: Left: SN 1006 Supernova Remnant composite image in x-ray, optical and radio. Credit: NASA/ESA/Zolt Levay (STScI). Right: SN 1054 remnant (Crab nebula) taken at Nordic Optical Telescope (NOT). Credit: Drachmann/Hobert/Holm/Jul.

Table 2.1: Mapping of SN Types to their Likely Progenitor Star Properties

SN	Progenitor Star[a]	M_{ZAMS} ($M_\odot$)	$\dot{M}$[b] ($M_\odot$ yr^{-1})	V_∞ (km s^{-1})
II-P	RSG	8 - 20	$10^{-6} - 10^{-5}$	10 - 20
II-L	RSG/YSG	20 – 30 (?)	$10^{-5} - 10^{-4}$	20 - 40
II-pec	BSG (b)	15 – 25	$10^{-6} - 10^{-4}$	100 - 300
IIb	YSG (b)	10 – 25	$10^{-5} - 10^{-4}$	20 - 100
Ib	He star (b)	15 – 25 (?)	$10^{-7} - 10^{-4}$	100-1000
Ic	He star (b)/WR	25 – ?	$10^{-7} - 10^{-4}$	1000
Ic-BL	He star (b)/WR	25 – ?	$10^{-6} - 10^{-5}$	1000
IIn (SL)	LBV	30 – ?	(1 – 10)	50 - 600
IIn	LBV/B[e] (b)	25 – ?	(0.01 - 1)	50 - 600
IIn	RSG/YHG	25 – 40	$10^{-4} - 10^{-3}$	30 - 100
IIn-P	super-AGB	8 – 10	0.01 - 1	10 - 600
Ibn	WR/LBV	40 – ?	$10^{-3} - 0.1$	1000
Ia/IIn	WD (b)	5 - 8 (?)	0.01 - 1	50 - 100

Notes. An overview of the progenitor stars for the various SN types with their *Zero Age Main Sequence* Mass (M_{ZAMS}), mass-loss rate ($\dot{M}$) and the wind terminal velocity (V_∞). From Smith (2014).

[a] Most likely progenitor star type. "(b)" indicates that a binary channel is probably key. Note that stars which shed envelopes in *binary Roche-Lobe overflow* (RLOF, see Sect. 2.3.3) are likely to have a slow (10 km s^{-1}) equatorial outflow, in addition to the wind speed of the star.

[b] Mass-loss rates for pre-SN eruptions are listed in parentheses, corresponding roughly to the total mass ejected in the few years immediately preceding core-collapse. The mass-loss rates may be lower but still substantial at larger radii traced by the expanding SN shock at late times.

2.3 Stellar Winds and Outbursts

The lives of high mass stars, and in turn what happens in the end, are very much influenced by the amount of material that it succeeds in losing during the various phases. Because of the very high luminosity, i.e. very high radiation pressure pointing outwards, massive stars are generally on the verge of instability. A star is stable when the gravitational force is equal to the radiation pressure, but sometimes the radiation pressure exceeds the gravitational force, like during outbursts or luminous winds. This results in material being thrown away from the star's surface. The upper limit for the radiation pressure, i.e. the highest luminosity the star can attain without surpassing the hydrostatic equilibrium, is called the *Eddington Luminosity*, given as:

$$L_{\text{Edd}} = \frac{4\pi cGM}{\kappa}, \tag{2.10}$$

which means that higher values of the opaxity, κ, i.e. the material being more interactive with the radiation field, the less luminosity is needed to exceed the limit and cancel the hydrostatic equilibrium.

There are in general three different "ways" of mass-loss. The first being a steady continuous wind over a longer period of time (see the following section) and the second being massive and violent eruptive events that occur on shorter times scales (Sect. 2.3.2). The last one, called *Roche-Lobe Overflow* (RLOF) happens in binary systems through mass accretion on to a stellar companion (Sect. 2.3.3).

2.3.1 Steady Outflows

For high mass stars the most of their lives are spent as hot stars, such as OB and WR stars. The mass loss in this phase is dominated by the so-called *line-driven wind*. These winds arise due to the high radiation pressure pointing outwards and away from the star, since light transfers momentum to the gas through absorption and scattering by UV metal lines. The mass loss through line-driving hence depends on the luminosity (in the UV), the metallicity as well as the temperature of the star. The mass loss rate can be expressed as:

$$\dot{M} = 4\pi r^2 \rho(r) v_\infty, \tag{2.11}$$

where $\rho(r)$ is the average mass density at radius r where the wind has reached its terminal velocity, v_∞. The latter is usually determined by looking at *P Cygni* absorption

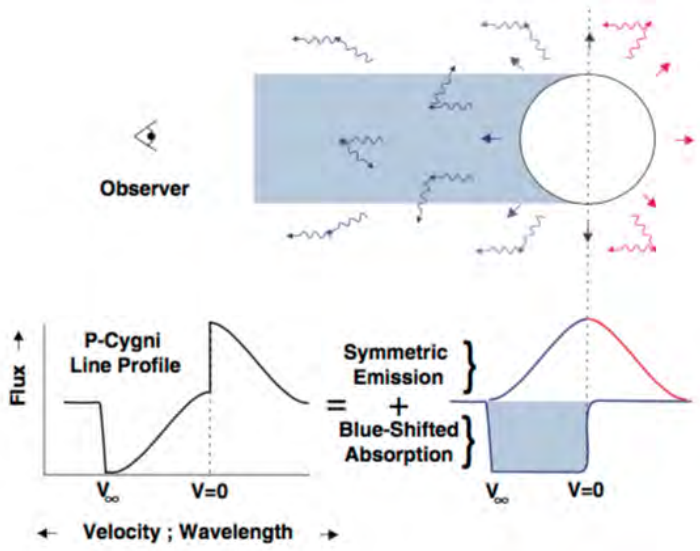

Figure 2.8: Schematic illustration of the formation of a P Cygni line profile due to stellar wind outflow. From Owocki (2000).

lines, which are very characteristic, in the UV.

Figure 2.8 shows a schematic of how the P Cygni line is formed. The material from wind approaching the observer, inside the absorption column (see Fig. 2.8) has its line blueshifted (due to the Doppler effect). The observed flux is reduced because of scattering of radiation, which results in an absorption line on the blue side of the line profile. Outside the absorption column, the wind material can be either blue- or redshifted from scattering, which results in an increase in the flux, hence higher emission. Combining these two effects result in an absorption line shortwards of $v = 0$ and an emission line for $v > 0$. The P Cygni line is a direct observational evidence of mass-loss. An example of an observed P Cygni line is plotted in Fig. 2.9, which show a typical P Cygni type profile found in the spectrum of SN1997eg, suggesting that the SN has encountered a dense circumstellar medium (CSM).

2.3.2 Eruptive Mass Loss

Sometimes stars, such as the LBV class, can experience extreme mass-loss during a period of years to a few decades, in what we call "giant eruptions". During these eruptions the star's luminosity is suddenly and drastically increased, which could lead to a so-called *super-Eddington* (SE) wind that drives the high mass-loss, in which the *Ed-*

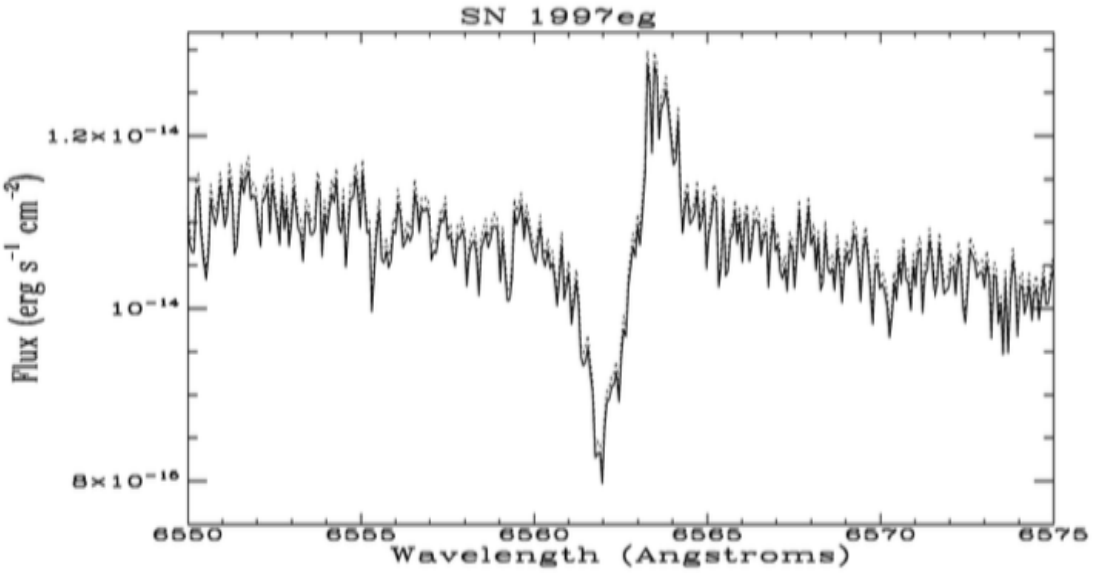

Figure 2.9: Typical P Cygni line profile observed in the spectrum of SN1997eg. The line indicates the existence of dense circumstellar material which the SN ejecta is expanding into. From Salamanca et al. (2002).

dington Ratio[3], Γ, exceeds unity substantially, as in the case of the "Great Eruption" of the star η Car with values of $\Gamma \simeq 5$ for about a decade (Smith, 2014).

Another theory is that the eruptions might be hydrodynamic explosions, meaning the mass-loss is powered by a shock. This was partly motivated by the very high-speed ejecta of η Car with velocities of about 5000 km s^{-1} which might be unlikely to achieve without a strong blast wave. Also the thin walls, or ring structure, of the nebula indicates a small range of expansion velocities. This is most easily explained by a compression in a shock (Smith, 2014). What is causing these eruptions are still up for debate.

Some of these outbursts or explosions are so huge and luminous that they look similar to, and are sometimes mistaken to be, a SN. Stars exhibiting these events are called SN impostors, sometimes referred to as a Type V SN. Eruptions, like that of η Car, emits light of order comparable to what is emitted from a SN, but after the light has faded the progenitor star still remains. Some of these events happen just prior to the real SN in LVB stars, which is suggested to be the case of SN 2009ip by Mauerhan et al. (2013). SN2009ip has been classified as an LVB with several outburst leading up to a final outburst which transitioned into a SN. More examples of SN impostors include the great eruption of η Car, P Cygni and SN 2006jc.

[3]The Eddington Ratio is defined as the ratio between the luminosity and the Eddington Limit form Eq. 2.10: $\Gamma = \kappa L / 4\pi cGM = L/L_{\text{Edd}}$.

2.3.3 Binary Systems

There are now strong evidence that most high mass stars (about 3/4) exists in binary systems in close enough orbit to interact and exchange mass (Smith, 2014). Binary systems must therefore dominate the mass-loss and transfer effects of high mass stars. When the massive star enters the post-MS phases its temperature slightly drops and its radius will increase severely. If the star expands enough for the photosphere to extend beyond the star's *Roche Lobe*, its mass will transfer onto the companion. The Roche Lobe is the volume within which the material is gravitationally bound to the star. This kind of mass-loss/accretion is called *Roche Lobe Overflow* (RLOF). Two examples of RLOF is shown in Fig. 2.10 for a low mass (left) and a high mass binary (right).

RLOF can happen multiple times during the lifetime of the binary system, exchanging mass back and forth. When the mass is transferred to the companion, the material will slowly evolve into a disc, because the particles lose their angular momentum due to friction, creating an accretion disc. The material in the disc will in turn accumulate onto the star, which can lead to numerous possibilities of further evolution. In general you can divide close binaries into three classes:

1. Detached binary: both stellar radii are smaller than the stars' Roche Lobes.
2. Semidetached binary: one of the stars' radius exceeds its Roche Lobe and material may accrete onto the stellar companion.
3. Contact binary: both stellar radii extends beyond the Roche Lobes, resulting in a common envelope.

It is in the semidetached case we see stellar interaction. Relatively low rates of mass transfer in close semidetached binary systems may give rise to outbursts from increased luminosity.

A comparison of all the different mass-loss rates have been made in Fig. 2.11, where the various rates are shown for different luminosities. It is quite clear that the mass-loss increases for higher values of luminosity. Notice how much higher the mass-loss is for the LBV giant eruptions in the upper right corner (though found assuming the total ejecta being lost over a period of 10 yr). These winds and outbursts have gas densities as well as temperatures which are good conditions for dust formation.

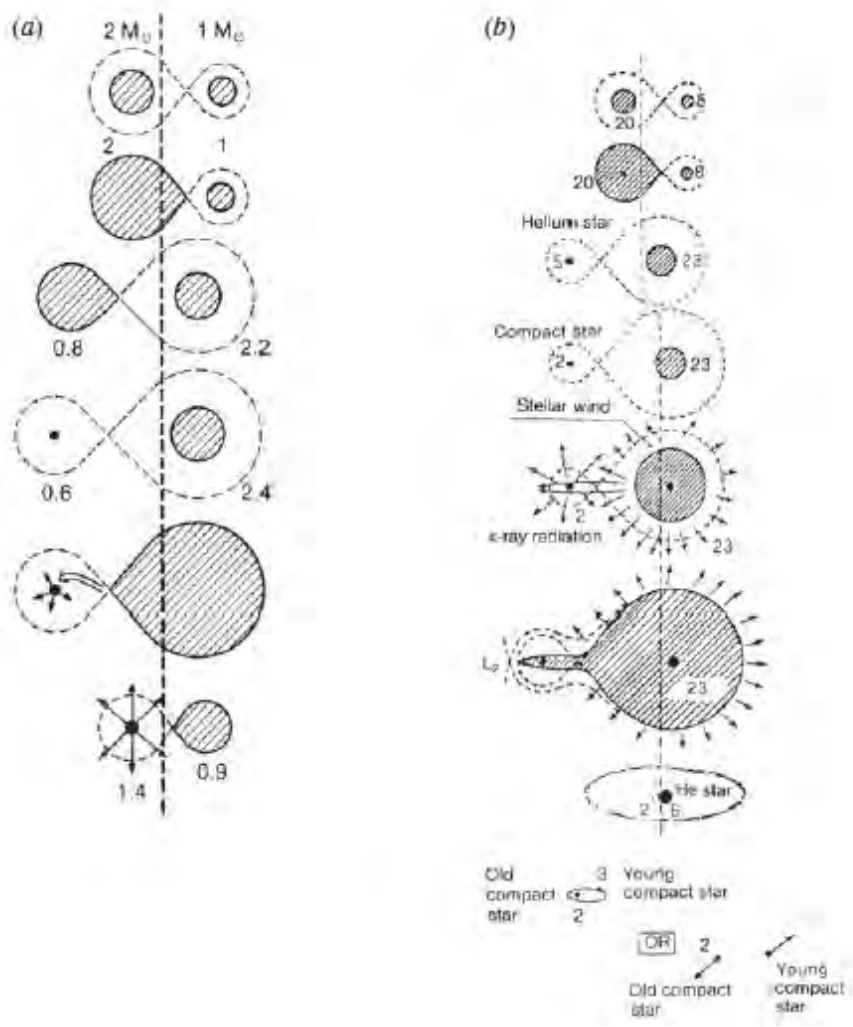

Figure 2.10: Schematic showing the stellar evolution of stars in binary systems. The numbers on each side of the dashed line indicates the mass of the stellar object at this point. *(a)* Low mass binary: i) Both stars on the main sequence; (ii) mass transfer from the more massive of the stars to the lighter once the former becomes a red giant; (iii) formation of a light subgiant and a more massive main sequence companion; (iv) formation of a white dwarf and a main sequence stars; (v) mass transfer onto the white dwarf when the second star becomes a giant; (vi) the white dwarf exceeds the Chandrasekhar mass and explodes as a Type Ia supernova.
(b) High mass binary: (i) Main sequence phase; (ii) the more massive star fills the Roche lobe as it becomes a red giant and mass transfer begins; (iii) end of the first mass transfer phase; the first Wolf-Rayet phase begins; (iv) the helium star has exploded leaving 2 $M_\odot$ remnant which may be a neutron star or a black hole; (v) the massive star becomes a giant star and mass is transferred onto the compact star which becomes a strong X-ray source; (vi) large scale mass-loss onto the secondary star begins; (vii) the second Wolf-Rayet phase in which the more massive star has lost its envelope leaving a roughly 6 $M_\odot$ helium star ; (viii) the 6 $M_\odot$ star explodes as a supernova. From Longair (2011).

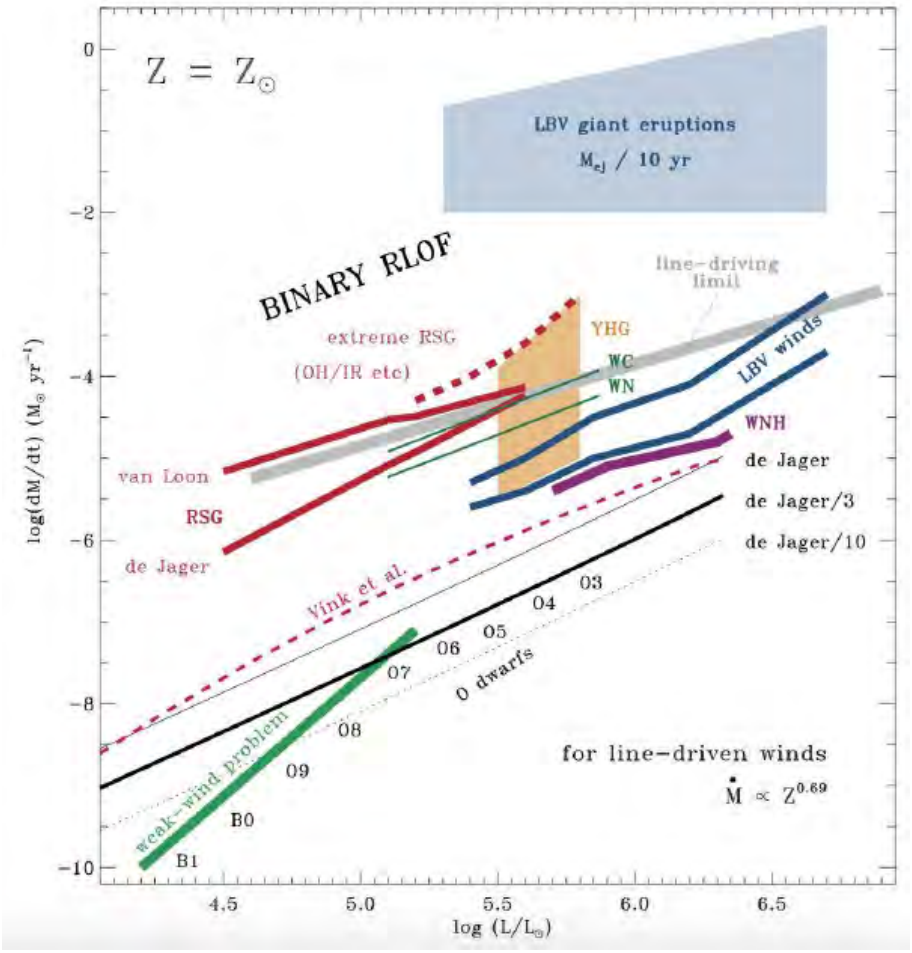

Figure 2.11: Different mass-loss rates for various stellar types. Pay most attention to the difference in the LBV winds and the very high rates from the LBV giant eruptions. See Smith (2014) for further details.

2.4 Dust

Whether we like it or not, dust plays an important role in astronomy and astrophysics. Almost everywhere we look in space we see dust, or at least evidence of it, since it obscures and scatters the light from the objects we actually want to look at, it being stars, quasars, supernovae and so on. Dust are responsible for absorbing about one third of the starlight in a normal spiral galaxy and re-emitting it in the IR and it makes up about 0.1% of the total baryonic mass in the Milky Way.

When talking about dust we are talking about larger and more complex molecules than usually. These molecules are of comparable size to particles in f.ex. smoke, typically up to about a few microns (μm). The composition and the formation site of the dust still remain uncertain, but I will give some general features and considerations in

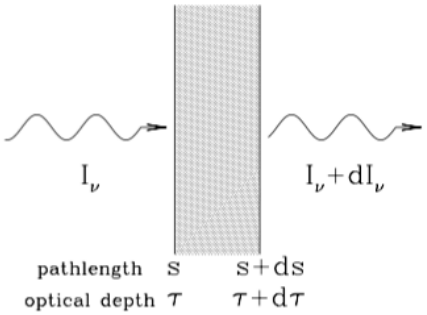

Figure 2.12: Illustration of the geometry of radiative transfer. See text for explanation. From Draine (2011).

the following sections. Dust is believed to be responsible for the formation of planetary systems when the grains start to coagulate into larger grains, creating planetesimals and planets, but dust is also thought of as the key ingredient of life.

2.4.1 Absorption

First, lets have a look at how light propagates through space. Radiative transfer theory describes how light travels through a medium which absorbs and emits. Radiation with specific intensity I_ν (intensity that is frequency/wavelength dependent) encounters a medium and exits on the other side. Depending on how the medium interacts with the radiation, the specific intensity has now changed with dI_ν (see illustration in Fig. 2.12). The equation of radiative transfer tells us that:

$$dI_\nu = -I_\nu \kappa_\nu ds + j_\nu ds. \tag{2.12}$$

The first term, $-I_\nu \kappa_\nu ds$, is the absorption and stimulated emission done by the medium a long the beam path ds. κ_ν is the absorption coefficient which is frequency (or wavelength) dependent. The second term is the change in I_ν due to spontaneous emission by the material and j_ν is the emissivity which is also frequency dependent.

Instead of using the pathlength ds we can express Eq. 2.12 in terms of the *optical depth* τ_ν. The optical depth is defined as:

$$d\tau_\nu \equiv \kappa_\nu ds, \tag{2.13}$$

and is a quantity that tells us something about how transparent or *opaque* a medium

is to radiation. Using this rewrites Eq. 2.12 to:

$$dI_\nu = -I_\nu d\tau_\nu + S_\nu d\tau_\nu \tag{2.14}$$

where

$$S_\nu \equiv \frac{j_\nu}{\kappa_\nu} \tag{2.15}$$

is the *source function*. If the medium is uniform and the radiation field is in local thermodynamic equilibrium (LTE), the medium absorbs the same amount of radiation as it emits and hence:

$$dI_\nu = 0 = -I_\nu d\tau_\nu + S_\nu d\tau_\nu, \tag{2.16}$$

which means that $I_\nu = S_\nu$. A radiation field in LTE will have the same intensity as a black-body and therefore $I_\nu = B_\nu(T) = S_\nu$, where $B_\nu(T)$ is the Planck law with temperature T.

Dust grains are heated by light from the star it surrounds, with the intensity mainly dominating the UV and optical part of the electromagnetic spectrum. When a grain absorbs an ultraviolet or optical photon, an electron is excited to a higher energy state or, if powerful enough, completely removed from the grain as a *photoelectron* (free electron). Typically, the grain or molecule will deexcite *nonradiatively* through vibrations in the molecular structure, redistributing the energy internally which results in heating of the grain.

2.4.2 Emission

Kirchoff's law tells us that bodies which are good absorbers must be equally good radiators. Once the grain has been heated it needs to cool by getting rid of the extra energy provided by the incident photon. This can be done through the following mechanisms:

1. Emitting a thermal photon
2. Collisional deexcitation with cold atoms or molecules
3. Ejection of atoms or molecules from the grain surface

Dust grains in equilibrium have temperatures in the range 30-50 K, which mean their radiation dominates at far-infrared (FIR) wavelengths of 50-100 μm. However, dust grains are not very efficient radiators at long wavelengths and radiates as a *modified*

black-body rather than a perfect one. This means that the dust will have a higher temperature than a perfect black-body in the same radiation field.

In the FIR ($\lambda > 60\,\mu$m) a continuous emission (continuum) is created by warm normal-sized grains which are in thermal equilibrium with the radiation field. These normal dust grains typically has a size $> 0.01\,\mu$m and a temperature about $20-40$ K. Smaller grains (tiny) with sizes of about $5-50$ Å and temperatures of a few hundred to a few thousand kelvin are responsible for a continuum in the area $3-30\,\mu$m due to non-equilibrium heating.

The black-body spectrum is given by the Planck function, or Planck's radiation law, telling us what the spectral radiance should be given a temperature and wavelength or frequency. The law is expressed as:

$$B(\nu, T) = \frac{2h\nu^3}{c^2} \frac{1}{e^{h\nu/k_B T} - 1} \tag{2.17}$$

or using wavelength

$$B(\lambda, T) = \frac{2hc^2}{\lambda^5} \frac{1}{e^{hc/\lambda k_B T} - 1}, \tag{2.18}$$

where h is the Planck constant, k_B is the Boltzmann constant and c is the speed of light. An approximation of this was discovered several years before Max Planck by Wilhelm Wien, who found that the emission from a black-body source peaks at a given wavelength as (Wien's displacement law):

$$\lambda_{max} = \frac{b}{T}, \tag{2.19}$$

where $b = 2900\,\mu$m·K is Wien's displacement constant. Using this we see that a black-body with temperature in the range 30-50 K should have its peak emission about $\lambda_{max} = 2900\mu$m·K / T $\simeq$ 60 to 100 μm, which is in the IR regime. However, Wien's law (or sometimes referred to as Wien's approximation) works well at lower wavelengths but not at longer, so the result should be taken lightly.

2.4.3 Formation

Red giants and planetary nebula envelopes seem to be the primary formation site for dust grains, as what we have seen observationally. These areas have optimal conditions for dust formation which are reasonably high densities ($\log(N)\langle H\rangle > 10^8\,\mathrm{cm}^{-3}$) and temperatures close to heavy element condensation temperatures of < 2000 K. Once the

grains have formed they can grow through coagulation or surface accretion of atoms and molecules, and they can brake into smaller pieces through sputtering and collisions (grain-grain).

AGB stars seem to be the primary formation site for dust particles. Depending on their O/C abundance they are divided into two classes:

Oxygen rich (O>C): A lot of oxygen is found in the atmospheres of the stars. Most of the carbon gets locked up with the oxygen creating CO and silicates acts as the primary condensates. This is seen as strong 10 μm silicate features in the spectra of the dusty outflow.

Carbon rich (O<C): The atmospheres are very carbon rich due to nucleosynthesis and dredge-up. Carbonaceous solids as graphite and amorphous carbon are here the principal condensates. There is no 10 μm silicate feature in the spectra but sometimes one can be seen at 11.3 μm which arises from SiC.

AGB stars are, however, a rather long term solution to our dust problem. It takes many years for a low mass star to reach the AGB stage, and since more observations of dusty high-redshift galaxies are coming up these days, we are in need for some fast, short term injection of dust. Solutions to this could be provided through dust formation in novae and supernovae. These have also been observed as sites of dust formation. It is however unclear whether or not the dust grains are able to survive the shock waves of the supernova and to what extent.

2.4.4 Models

Dust models are usually based on one of two types of elements, which are the two main dust types that will form in the stellar environment, being carbon and silicates (besides iron, corundum (Al_2O_3), magnetite (Fe_2O_4) and SiO_2 grains). However, the two main species will be carbon dust and silicate dust. These two dust types will typically not form in the exact same location due to the high binding energy of carbon monoxide (CO). As CO is the most tightly bound molecule, then in equilibrium situations all available carbon-atoms and all available oxygen-atoms will form CO. CO divides dust nucleation and growth into two different chemical paths:

C/O > 1: Carbon chemistry (C_2, CN, CH, C_2H_2, C_3, HCN).
Possible dust types: graphite (C), amorphous carbon (C), diamond (C), silicon carbide (SiC).

C/O < 1: Oxygen chemistry (OH, SiO, TiO, H_2O, TiO_2, VO, ZrO, ScO, YO, LaO).
Possible dust types: enstatite ($MgSiO_3$), olivine ($MgFeSiO_3$), ferrosilite ($FeSiO_3$), pyroxene ($MgFeSiO_4$), forsterite (Mg_2SiO_4), fayalite (Fe_2SiO_4).

Carbon has the unique property that the atoms can form three different types of bonds through sp^1, sp^2 (graphite) and sp^3 (diamond) hybridization. Amorphous carbon is a broad term covering materials which have a combination of the different bond types. Amorphous materials can show a whole range of different optical properties related to the exact microphysical properties of the measured sample. Amorphous carbon is an illustrative example of this, as the measured extinction can differ by a factor of 10 (Andersen et al., 2003), depending on the detailed microphysical properties of the amorphous dust.

Silicates are the most stable condensates formed from the abundant elements O, Si, Mg and Fe. Out of these four elements silicate grains form as silicatetrahedras (SiO_4) combined with Mg^{2+} or Fe^{2+} cations. In the crystalline lattice structures it is possible for the tetrahedras to share their oxygen atoms with other tetrahedras and thereby form many different types of silicates. The optical properties of these silicates all have resonances around $10-20\,\mu$m, due to the Si–O stretching and the O–Si–O bending mode arising from the silicatetrahedras. Alignment of the tetrahedras may cause sharp peaked resonances, whereas amorphous silicates will show a broad feature which can be seen as a blend of such sharp resonances.

A crystalline solid has a highly ordered lattice structure, with constant bond lengths and angles between atoms. In a solid, rotational motions are not possible and the vibrational-rotational transitions seen in gas-phase molecular spectra are replaced by a broad, continuous band at the vibrational frequencies. Due to the symmetry of the structure, only a few of the possible lattice vibrational modes are optically active. Therefore, crystalline solids have only a few sharp features in the IR.

To interpret the observed extinction related to a given type of dust material, it is necessary to determine the extinction efficiency (Q_{ext}). The extinction is given as the sum of absorption and the scattering ($Q_{ext} = Q_{abs} + Q_{sca}$) and is a function of the dimensionless size parameter $x = 2\pi a/\lambda$ and a composition parameter, the complex refractive index of the material, $m = n - ik$. The problem is that of solving Maxwell's equations with appropriate boundary conditions at the grain surface. The method of solution is there often refereed to as Lorenz-Mie theory. For more detail see the textbook by Bohren and Huffman (1983).

3 Data

The data used for the analysis throughout this thesis comes from two specific telescopes. Most importantly is the *Herschel Space Observatory* (on the right in Fig. 3.1) from which I required most of my data. Additionally, I retrieved a single wavelength frame from the *Spitzer Space Telescope* (on the left in Fig. 3.1). First, I will give a short introduction to the data, the telescopes and their instruments in the upcoming section (Sect. 3.1). Secondly, I will talk about the selection criteria for making my sample (Sect. 3.2) and finally I will give a quick tour through my targets (Sect. 3.3).

3.1 *Herschel* and *Spitzer*

The *Herschel* Space Observatory contains two photometric instruments from which I obtained most of my images. The first is the *Photodetecting Array Camera and Spectrometer* (PACS) which observes in three different wavelength intervals: blue, green and red. The blue observes at 70 μm (60 to 85 μm), the green at 100 μm (85 to 125 μm) and the red at 160 μm (125 to 210 μm).

The second instrument is the *Spectral and Photometric Imaging Receiver* (SPIRE) which observes at longer wavelengths divided into three intervals: short, medium and long, centred around 250, 350 and 500 μm, respectively. All the observations I found

Figure 3.1: Images of the *Spitzer* Space Telescope (left) and the *Herschel* Space Observatory (right). Courtesy of NASA/JPL-Caltech and ESA.

were all taken using the parallel mode, SPIREPACS, where both instruments were used. This, however, means that only two out of the three PACS windows were used, i.e. the blue and the red (70 and 160 μm). All the three possible SPIRE images were taken, though.

Additionally, a last image was used from the *Spitzer* telescope's *Multiband Imaging Photometer for Spitzer* (MIPS) instrument, which produces imaging and photometry in three bands centered around 24, 70 and 160 μm. But since the frames at 70 and 160 μm is already covered by *Herschel*, I only recovered the 24 μm frame.

My images were found using the *Herschel Interactive Processing Environment* (HIPE), from which you can directly access the *Herschel Science Archive*. The objects were found by a coordinate search and retrieved to HIPE, where I was able to locate my targets. Most of the times there were multiple hits on the coordinate search, because the search is done for the coordinates and a given radius. Not all of the observations contained the whole object which could lie just outside of the frame of partially outside, just on the border. Therefore, all the frames were inspected to see of the object were totally visible. All the images were in units of Jy/pixel.

All the images from *Herschel* had already been processed prior to the analysis following standard pipelines within HIPE. Depending on what analysis you want to do, different data products are available, e.g. for point sources and for extended sources.

Table 3.1: Instrument Data

Instrument	Wavelength (μm)	Resolution ($''$/pixel)	Flux Uncertainty (%)
MIPS	24	2.45	2
PACS	70	3.2	20
PACS	160	3.2	20
SPIRE	250	6	15
SPIRE	350	10	15
SPIRE	500	14	15

Since my targets are rather "big", or *not* point sources, I have used the products for extended photometry. Table 3.1 show some of the numbers of the instruments including the resolution and the flux uncertainty.

The MIPS-24 μm frame was found using the *Spitzer Heritage Archive*[1] where I found my objects also from a coordinate search. These images were in units of MJy/sr and therefore needed to be converted to units of Jy/pixel which could be done in HIPE. As so, they were imported to HIPE and converted to Jy/pixel using a build in unit conversion function[2]. The data products collected from *Spitzer* were also processed prior to the analysis following standard pipelines.

The articles (Gvaramadze et al., 2010; Wachter et al., 2010) from which I found my sample of objects, detected all the dusty nebulae from the MIPS-24 μm frame. They report the magnitudes of the stars using data from *Spitzer* at shorter wavelength frames centered at 3.6, 4.5, 5.8 and 8.0 μm from the *Infrared Array Camera* (IRAC) instrument, as well as various catalogues. Though, for the vast majority of the objects the dusty nebulae were only visible at 24 μm, they only report the magnitudes of the central sources.

3.2 Target Selection/Selection Criteria

The original list of targets consisted of 156 different dust puff candidates. The list was made from the discoveries from Wachter et al. (2010) and Gvaramadze et al. (2010), who found 62 and 115, respectively, with some overlaps. All these stars of various

[1] From: *http://sha.ipac.caltech.edu/applications/Spitzer/SHA/*

[2] The photometric maps from *Spitzer* does not know its own units when imported to HIPE. Using the function: *IMAGE.setUnit(Unit.parse("MJy/sr"))* defines the image's units. I convert the units to Jy/pixel by using: *IMAGE.convertImageUnit(image = IMAGE, newUnit = "Jy/pixel")*.

classes show signs of a surrounding dust shell at 24 μm. Some clearer than others and sometimes more than one.

To help narrow down the list of candidates to investigate I made a short list of selection criteria to follow:

Strict:

I Observations with both PACS and SPIRE.

II Visible and clearly defined nebulae in at least PACS70 μm frame.

And additionally:

III Signs of outer nebula.

IV Signs of surrounding cavity.

Item I was fairly easy. Using the *Herschel Science Archive* I was able to look up all 156 targets. Some were not observed at all and others were just outside the field of view or just on the edge. Only the ones that were fully visible (meaning the nebula was not partially cut by the edge) in both the PACS and the SPIRE frames were not discarded. *Item II* is a bit more subjective in the sense that the detection of a nebula is done by eye. It can sometimes be difficult to set the scale parameter in the most optimal way for the nebula to be as clear and the ISM to be as faint as possible.

The last two items were not as strict as the first ones. Again, these criteria were judged from visual inspection and were also rather difficult due to the scaling. However, the only way to clearly identify a second shell is by the presence of a cavity or it might just as well be the ISM. Nevertheless, all these criteria efficiently shortened the list of targets to 10 candidates for the inner shell analysis, whereas five of these also were qualified for the analysis of the outer shell. It is very likely that even more targets from the original list qualifies for further analysis but given the amount of time put into examining the frames for each object, a list of 10 makes up a large enough workload. A more detailed examination of the remaining objects would be recommended. The total list of targets are shown in Appendix A along with my initial findings and comments.

3.3 Targets

Table 3.2 shows my sample with the target name (as they are named in Wachter et al. (2010) and Gvaramadze et al. (2010)), their coordinates and whether or not they have a clear or signs of cavity and a definable/visible outer shell. Additionally, I have noted any possible spectral classes as found in the original papers and other comments. In Fig. 3.2 all the targets are shown in the MIPS-24 μm frame. Most of the targets show a more or less circular nebula with slightly fainter emission than compared to the most central objects, e.g. MN46 and W27a in Fig. 3.2d and 3.2i, respectively. Others show higher emission in the shell, which obscures the central object, like the case of MN18 and MN111 (Fig. 3.2b and 3.2f). Also note that some of the targets show hints of a ring-like structure at the boundary of the shells, e.g. the case of W8a and W43 (Fig. 3.2h and 3.2j). This could be an indication of shorter and more violent episodes of mass-loss from outburst rather than a continuous and steady outflow.

A comparison of two images from *Herschel* and *Spitzer* has been made in Fig. 3.3. The figure shows the star W27a in the MIPS-24 μm (left) and the PACS-70 μm (right) frame. When looking at the *Herschel* image one can see that the emission is more uniform throughout the shell than when looking at the *Spitzer* image. There is no trace of the central object, nor all the surrounding objects. Notice the that the ring structure is

Table 3.2: Target List

			Gvaramadze			
Target	RA (J2000)	DE (J2000)	Cavity?	Definable Outer Shell?	Class	Comments
MN14	14:31:11.00	−61:02:02.1	yes	yes		
MN18	15:16:41.00	−58:22:26.0	yes	yes		Blue Supergiant
MN19	15:19:59.90	−57:24:15.2	yes			
MN46	16:43:16.37	−46:00:42.4	some			cLBV
MN64	17:43:59.85	−30:28:38.5	some		M2	
MN111	19:43:53.19	24:15:31.3	some	yes		
			Wachter			
W:5	15:07:56.37	−58:18:23.8	some		M0 III/K0 I	
W:8a	15:33:03.10	−56:12:20.0	yes	yes	K1 II/G7 I	
W:27a	17:37:47.54	−31:37:33.4	yes	yes		
W:43	18:33:39.54	−08:07:08.4			G7 I	

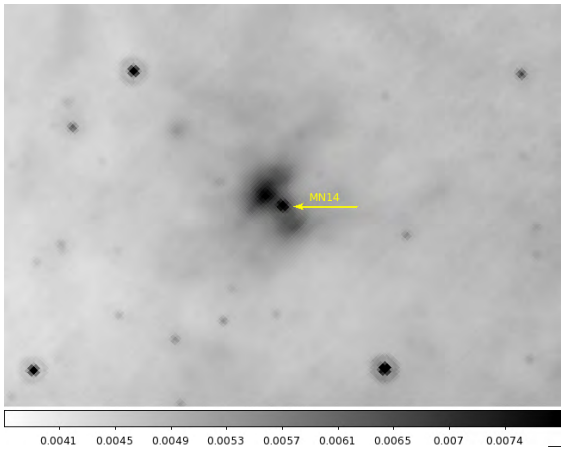

(a) MN14

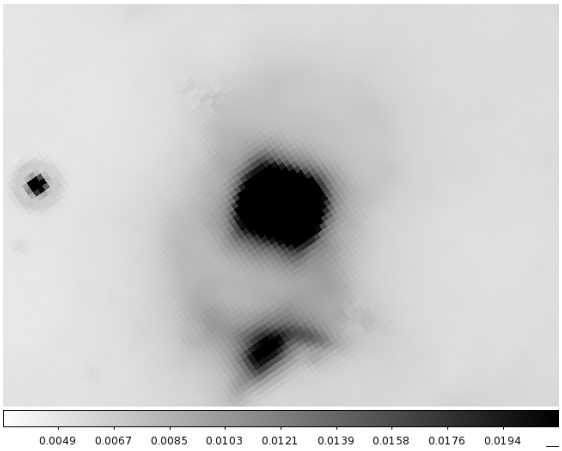

(b) MN18

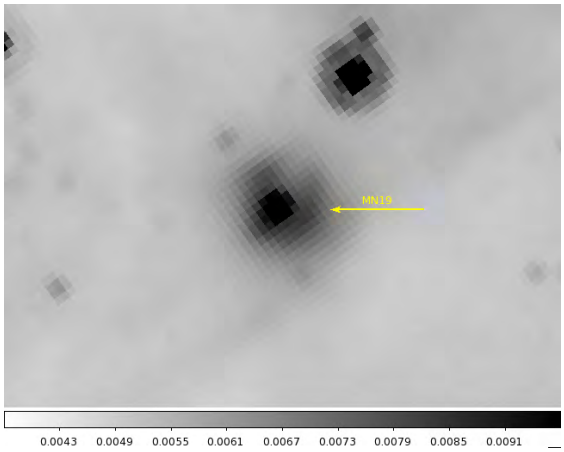

(c) MN19

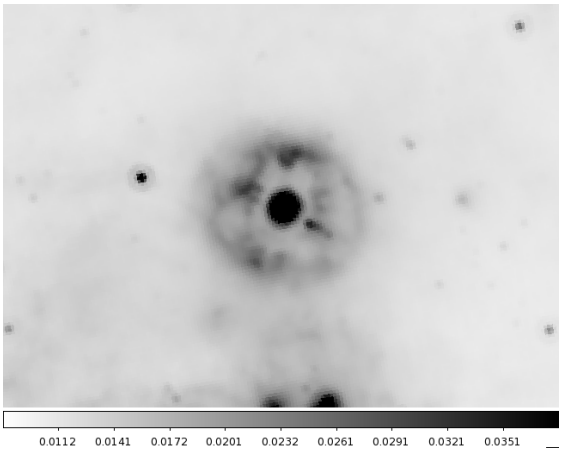

(d) MN46

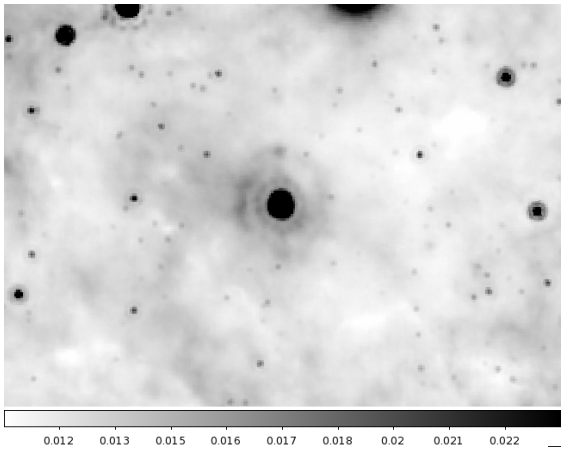

(e) MN64

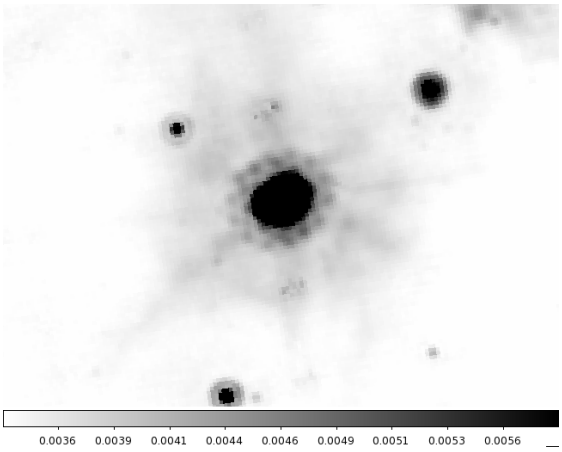

(f) MN111

Figure 3.2: Images from *Spitzer* MIPS-24 μm of the target nebulae. North is up and east to the left. Some of the targets' central region has been marked by an arrow to distinguish it from other nearby objects, likely binary stars. The flux scale on the bottom is in Jy.

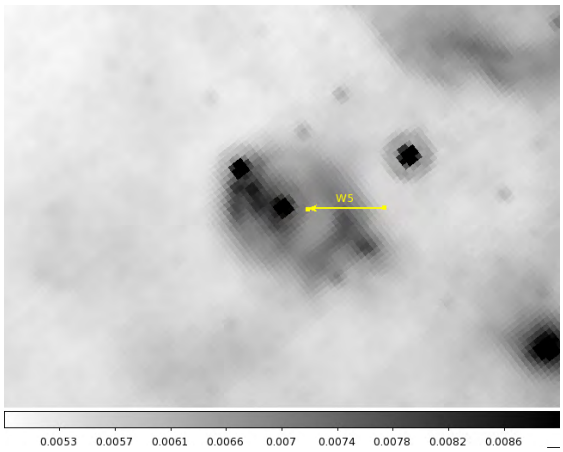

(g) W5

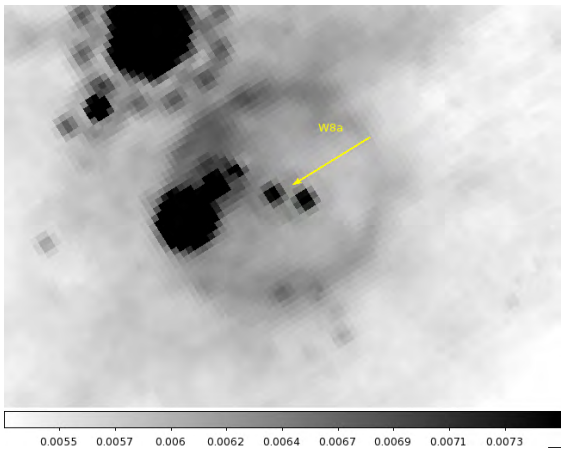

(h) W8a

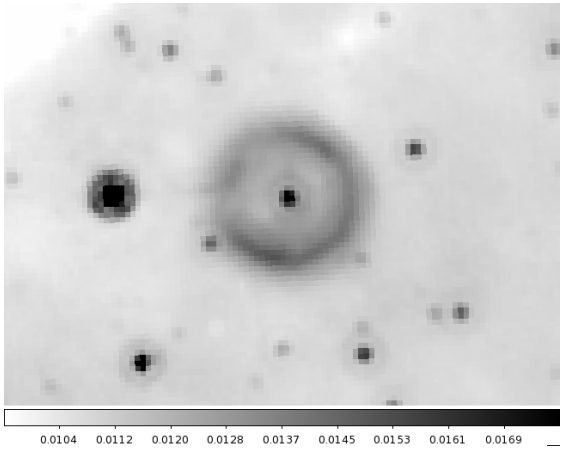

(i) W27a

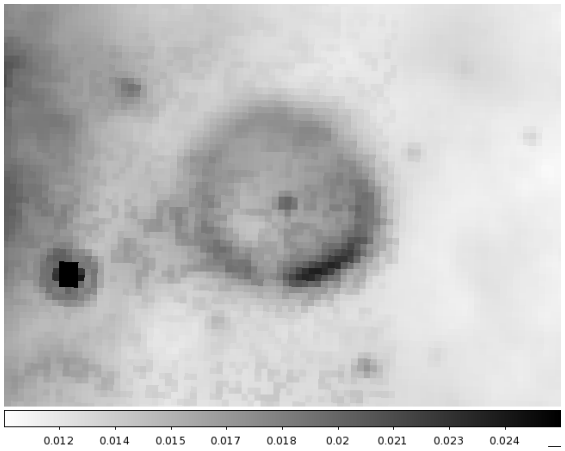

(j) W43

Figure 3.2: – *Continued.*

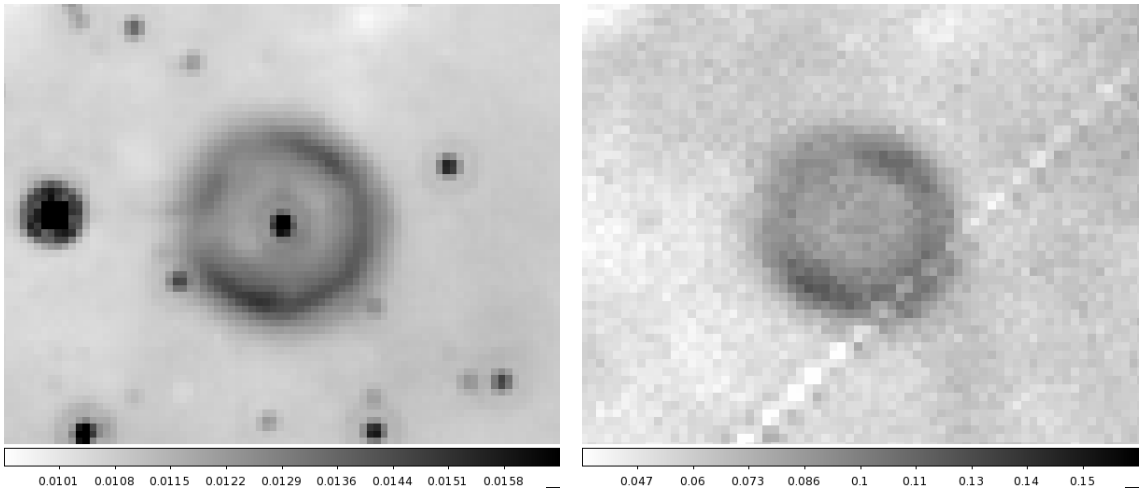

Figure 3.3: Inner shell of W27a. Left: MIPS-24 μm. Right: PACS-70 μm. North is up and east is to the left. The white line passing through the PACS image is from a nearby overexposed star (referred to as an artefact).

visible at both wavelengths.

In Fig. 3.4 the five targets with outer shells are shown. MN14 and MN111 (Fig. 3.4a and 3.4b) are shown in the MIPS-24 μm frame whereas the others are shown in the PACS70 μm frame, where the outer nebulae where most visible. Looking at the two first targets one can see (subtle) signs of a cavity (bright white areas), where for the others this is shown as the dark areas, between the outer nebulae and the surrounding medium. MN14, MN18 and MN111 have more easy definable shells, since these are of more circular or elliptical nature. The two remaining targets have more complex and irregular structures which makes it harder to distinguish the shell from the ISM. Looking at MN18 (Fig. 3.4c) the elliptical structure of the outer shell actually resembles that of the Homunculus Nebula which lies around the stellar system Eta Carinae (see Fig. 2.5), where the primary star is classified as a LBV.

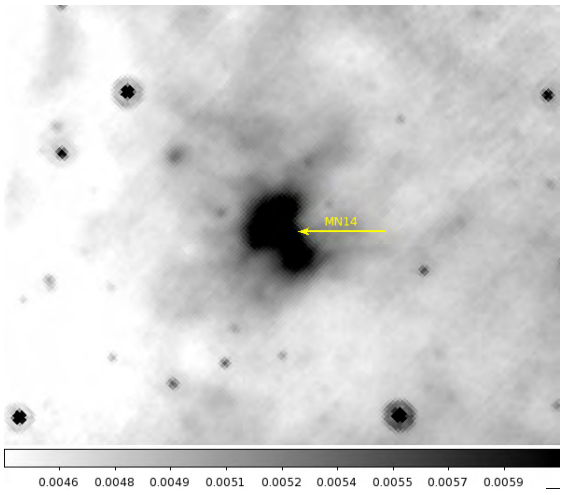

(a) MN14 in MIPS-24 μm.

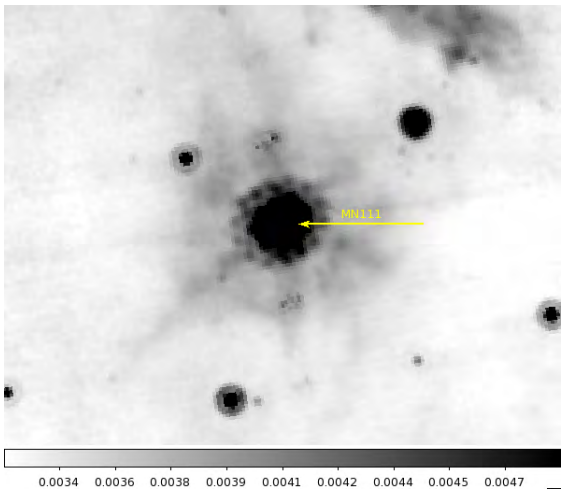

(b) MN111 in MIPS-24 μm.

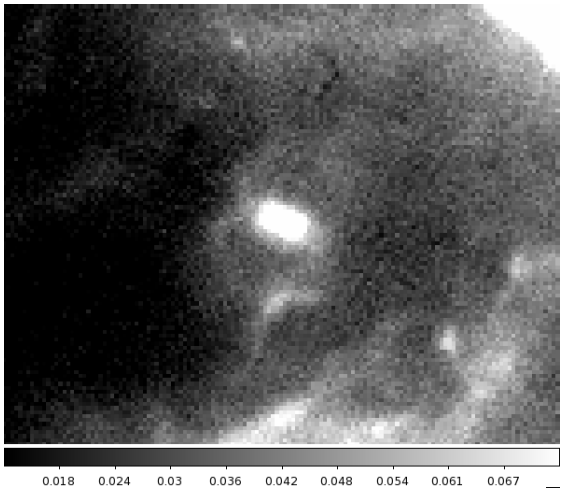

(c) MN18 in PACS-70 μm

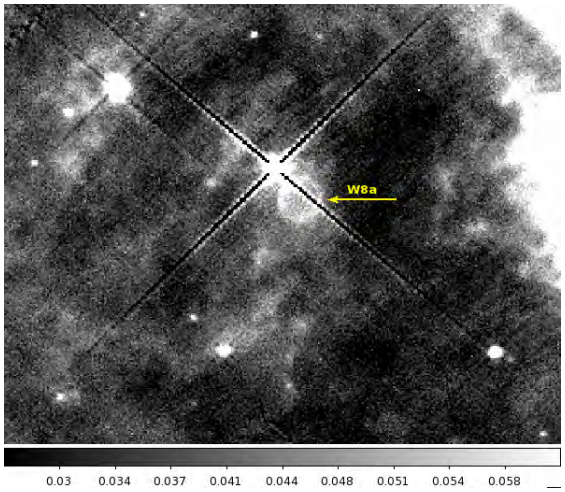

(d) W8a in PACS-70 μm

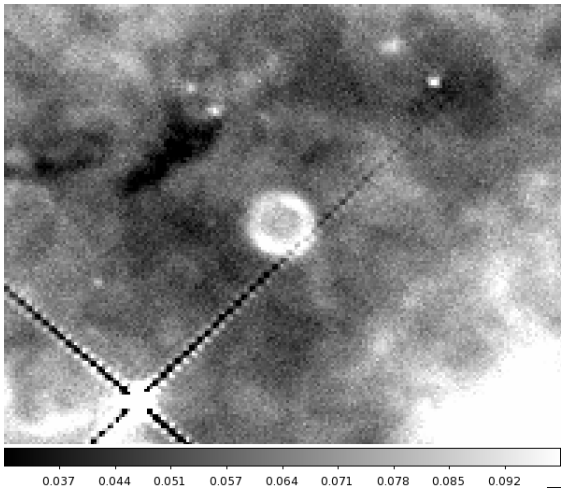

(e) W27a in PACS-70 μm

Figure 3.4: Outer shells of targets.

4 Analysis

During this project I have used various tools and methods to analyse my data. The steps and theoretical models are described throughout this section. In the upcoming section I will tell about one of my main methods, *Aperture Photometry*, which gives me the flux density of the sources at each wavelength. Slightly different approaches have been used for the case of the inner shells (Sect. 4.1.1) and the case of the outer shells (Sect. 4.1.2). In Sect. 4.2 I will explain how I obtain the dust masses by fitting the *Spectral Energy Distribution*.

4.1 Aperture Photometry

To obtain the flux densities I have used the method of aperture photometry. After identifying the source or target you wish to investigate, you enclose the source with an aperture (a circle or ellipse) such that all the flux coming from the target is within this. The aperture should be as small as possible for the sky contribution to be minimal, but large enough so it does not eliminate any of the target flux. Though, we are still looking through some amount of "sky" along the line-of-sight. By defining an annulus (ring) around the target one can determine the average flux contribution from the sky and subtract this from the initial source flux. The aperture and annulus of W27a are shown

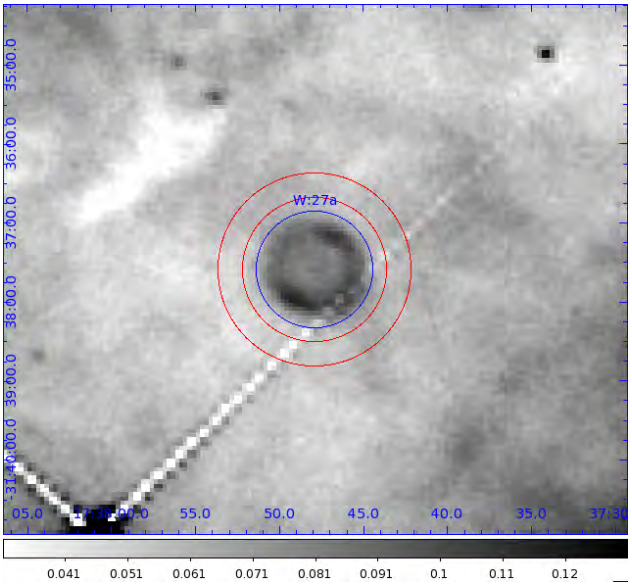

Figure 4.1: W27a with its aperture (blue) and annulus (red). The aperture only encloses the source dust shell. The annulus is chosen to be as close as possible to the source to measure the relevant background, but still far enough away to not include any flux from the source. The artefact across the image is from a nearby overexposed star.

in Fig. 4.1. For point sources one should include a correction term since the light is distributed over the pixels according to its *point spread function* (PSF), which occurs because of the telescope optics and the astronomical *seeing*. The aperture thus exclude a certain amount of the source flux. For extended sources this correction is negligibly small and can be ignored.

There are numerous tools for doing aperture photometry: Aperture Photometry Tool (APT), build-in functions in the Herschel Interactive Processing Environment (HIPE) and SAOImage DS9, just to name a few. Since HIPE is already used to find and retrieve the target images from PACS and SPIRE this would be the obvious choice, but it provides the flux densities with incorrect errors[1]. APT, as the name might suggest, is a great tool for doing this, but it does not do well with large images[2]. I therefore chose to use DS9 where I can manually calculate the errors based on the standard deviations of the pixel values. It should be noted that besides the errors, HIPE and DS9 give fairly persistent results.

[1] Of course, it is possible to change the settings so that the errors will be calculated correctly, but HIPE is highly based on build-in and automatic functions which makes it less accessible than DS9, which is way more manageable.

[2] All the images should then be scaled and the objects should be "extracted" in smaller images, but this would require an extensive amount of time because of the many different frames.

DS9 gives an output of variance or standard deviation per pixel as well as a mean and median value per pixel and number of pixels contained within a user defined region. In general the mean pixel value has been used in the calculation, but in some cases there are interfering artefacts and it might be more preferable to use the mode or median instead, since these are not affected as much.

4.1.1 Inner Shell

From the photometric maps I obtain the mean flux density for the source and the background as well as their extent in pixels. With this I get the sky-subtracted flux density for the source using:

$$F_s = N_s(\overline{s}_s - \overline{s}_{bg}) \tag{4.1}$$

where N_s is the number of pixels within the aperture (the target's pixels), $\overline{s}_s$ is the mean flux value within the aperture and $\overline{s}_{bg}$ is the mean flux value from the annulus, hence the background. The flux density is measured in Jy as defined in Eq. 2.3.

The hard part of this is to determine how large the aperture needs to be, i.e. the extent of the source. For this, one can try to determine the extent directly from the maps by eye, but one can also try to look at the radial plots or *aperture slices* for the target, which can be done in APT. An example is shown in Fig. 4.2. These plots are a good tool for determining the extent of the source. However, there are still no written rules for how to best determine the radius. It is still a matter of choice but one can more easily see on the graphs where the contribution is purely from the background. This should help minimize the amount of the target flux that is excluded.

In Fig. 4.3 one can see the dust shell around the star MN18 at six different wavelengths. Note how the shell is significantly more visible at the shortest wavelengths. This can also be shown using Wien's displacement law (Eq. 2.19) which tells us that a black-body emitter with a temperature of about 30-50 K should have its emission peak around 60-100 μm (although I must remind that dust grains are not emitting as a perfect black-body). At the longer wavelengths the temperature of the dust starts to approach that of the surrounding medium, which makes it harder to see if the flux contribution is from the shell or the background. Because of the vague detection in the SPIRE bands I have chosen to use the same aperture and annulus for all the frames, to be as consistent as possible. Otherwise it might be more correct to determine the sizes

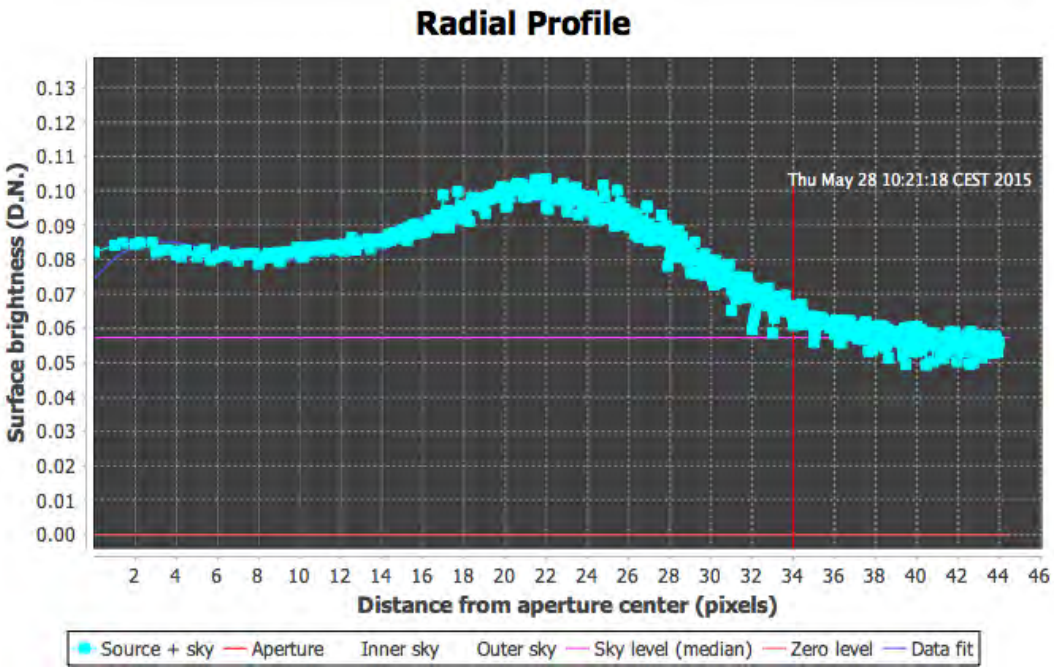

Figure 4.2: Output from APT for W27a: the radial profile. The graph shows the surface brightness as a function of the distance to the aperture center. The red vertical line marks the size of the aperture. The horizontal purple line indicates the sky level which, in this case, has not been subtracted.

of the aperture and annulus at all wavelengths.

4.1.2 Outer Shell

Some of the stars also show signs of a larger shell extending further away from the central source. These shells are even more faint and harder to define than the inner ones, since these have lower temperature and therefore blend in with the more comparable ISM. In order to find the flux radiating from the outer shell, one needs to remove the flux contribution from the inner parts as well as other interfering objects. The method is fairly similar to the one above. However, since they do not have a simple geometrical structure the outer shells are much more difficult to define. Figure 4.4 shows an example of an outer shell around target MN18 and W8a.

The dust in the outer shell is colder than the dust in the inner shell, hence it radiates less and more similar to the surrounding interstellar medium. Some of the targets show signs of a *cavity* ("empty space") around the shells with less ISM. This cavity most likely arose when the star was initially formed. The high and sudden radiation pressure would blow away the surrounding ISM and the remaining gas from the dark cloud of

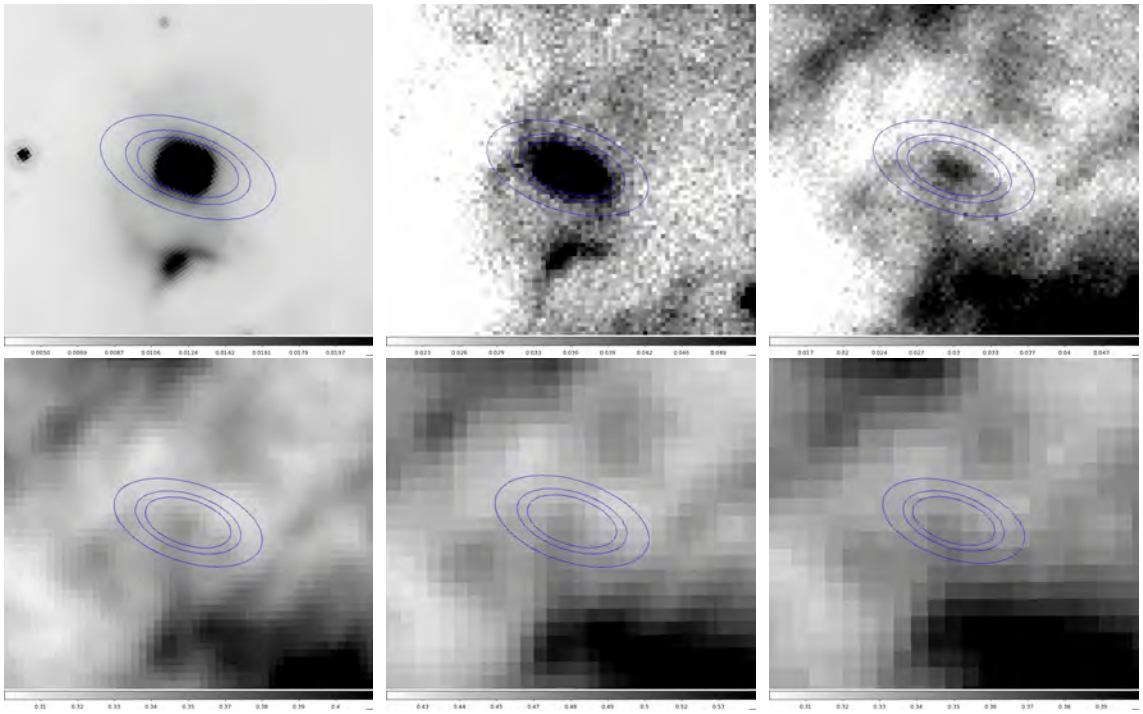

Figure 4.3: Each of the frames show the aperture for MN18 in six different wavelength bands. North is up and east is left. Top Left to Right: MIPS24, PACS70 and PACS160. Bottom Left to Right: SPIRE-250, -350 and -500. The aperture and annulus are shown in all the frames around the targets inner dust nebula. Note that the pixelation in the frames at longer wavelengths is due to the poorer resolution compared to those at shorter wavelengths (see Table 3.1.

which the star was made (Vamvatira-Nakou et al., 2013).

To find the flux from the outer shell I have subtracted the flux from the inner shell, the contribution from the background and possible interfering artefacts such as other objects or overexposed stars. Almost the same formula has been used as for the inner shell (Eq. 4.1). However, here I do not use the mean flux from within each area. I remove the total inner shell and artefact's flux contribution from the outer shell and divide it with the outer shell's area without the "contaminated" areas to find a mean flux value. It is then multiplied with the total area to find the total flux. The formula then looks as follows:

$$F = N_o \left[\frac{F_o - F_i - F_a}{N_o - N_i - N_a} - \frac{F_{bg}}{N_{bg}} \right], \tag{4.2}$$

where F_o is the total flux from the outer shell (the yellow region Fig. 4.4), F_i is total flux from the inner shell (blue region), F_a is the flux from any interfering artefacts (purple regions) and F_{bg} is the flux of from the background (red region). All with their respec-

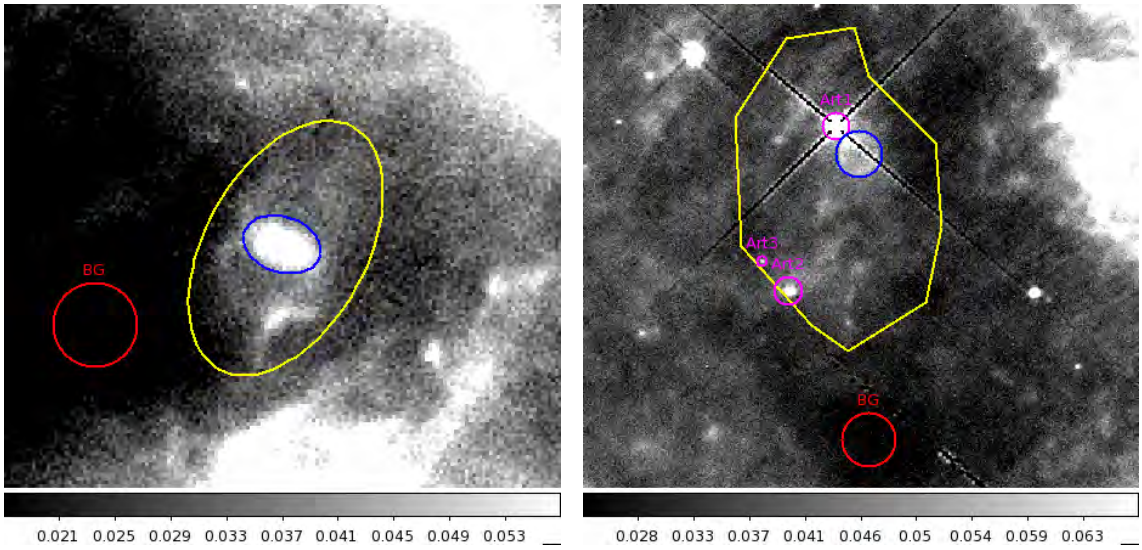

Figure 4.4: The outer shells of MN18 (left) and W8a (right) in the PACS70μm frame. North is up and east is left. Marked is the inner shell (blue) and the outer shell (yellow). Around the outer shells one can see a hint of the cavity (dark area) which has been used to distinguish the shell from surrounding medium. The red circles has been used to determine the background contribution. In the right frame some artefacts has been marked with purple.

tive sizes in terms of pixels (N_o, N_i, N_a and N_{bg}).

4.2 Spectral Energy Distribution

High mass stars mainly radiates in the visible or UV part of the electromagnetic spectrum. At longer wavelengths (lower frequencies and temperature) the intensity goes towards zero and does not contribute much to the spectrum. The dust surrounding the star, however, radiates in the infrared part because it has a much lower temperature and is thermal. If we therefore observe a given target at IR wavelengths we will only see the emission from the dust components around the star and by using aperture photometry we can get the flux densities for the dust.

When we have the flux densities from different wavelength frames we can plot them for these, hence making what is commonly known in astronomy as a *Spectral Energy Distribution* (SED). This is defined as:

$$F_\nu = \frac{M_\mathrm{d}}{D^2} B_\nu(T_\mathrm{d}), \tag{4.3}$$

where F_ν is the flux density, M_d is the dust mass, D is the distance to the star and B_ν

is the black-body function. Since we are dealing with dust which absorbs and re-emits the light in the infrared part of the spectrum and which is not a perfect black-body emitter, we must introduce an absorption coefficient, κ (Sect. 4.2.2). Doing this we get what is called a *Modified Black-Body function*.

4.2.1 Modified Black-Body Function

When a system is in thermodynamic equilibrium, i.e. has a – to some point – constant temperature overall, the system emits a special type of electromagnetic radiation called black-body (or thermal/temperature) radiation. It is a continuous spectrum over frequencies (or wavelengths) and depends solely on the systems temperature.

Stars are not in thermal equilibrium with their surroundings, but are still as a first approximation emitting as black-bodies. The radiation from the star's inner parts are travelling throughout the star, getting absorbed and re-emitted without any loss of energy, which means that the star is opaque. Of course there can be absorption and emission lines depending on the type of star, but in general the spectrum is dominated by the black-body radiation.

Recall Eq. 2.17 (Planck's law) that says the intensity of a black-body as a function of frequency, ν, and temperature, T, can be expressed as:

$$B(\nu, T) = \frac{2h\nu^3}{c^2} \frac{1}{e^{h\nu/k_B T} - 1}, \tag{4.4}$$

where h is the Planck constant, k_B is the Boltzmann constant and c is the speed of light in vacuum. If we take the absorption from the dust into account (since it is not a perfect black-body) we can alter the SED (Eq. 4.3) and get the modified black-body function:

$$F_\nu = \frac{M_\mathrm{d}}{D^2} B_\nu(T_\mathrm{d})\,\kappa, \tag{4.5}$$

where κ essentially is the absorption as a function of ν (monochromatic absorption coefficient), or the dust model.

4.2.2 Dust Models

The choice of dust model can have a significant impact on the resulting dust mass and temperature, to a lesser degree. They can be more or less complex depending on the assumptions about the dust composition and size distribution. Basically, the opacity κ

from Eq. 4.5 is the dust model that one chooses to use:

$$\kappa = \kappa_\nu \left(\frac{\nu}{\nu_0} \right)^\beta . \tag{4.6}$$

Here, ν_0 is the reference frequency and κ_ν is the corresponding absorption coefficient at this frequency. The parameter β says something about the dust composition and the grain size and geometry. By fitting Eq. 4.5 to the fluxes we can find the dust masses of the puffs around the stars as well as the dust temperature.

For both shells I have used two different dust models to fit the SEDs. The model parameters are shown in Table 4.1. The models are based on laboratory measurements of

Table 4.1: Dust Model Parameters

Model	κ_ν (m^2kg^{-1})	ν_0 (μm)	β	Reference
Carbons	45.0	20	1.45	Zubko et al. (1996) & Preibisch et al. (1993)
Silicates	5.0	70	1.95	Dorschner et al. (1995)

silicates Dorschner et al. (1995) and carbon (Zubko et al., 1996; Preibisch et al., 1993). A sample of different dust models are shown in Fig. 4.5, where κ is plotted as a function of the wavelength. In general, the models are linear (in logarithmic space) when we look at the IR regime. At shorter wavelengths κ is more difficult to model since it behaves very different from model (dust type) to model. Fitting the data from Fig. 4.5 using Eq. 4.6 we find our dust model parameters.

4.2.3 Single and Double Component SED

In most of the cases fitting a single dust component is not totally accurate as if done by fitting with the modified black-body function from Eq. 4.5, because of the "flatting" at the top of the SED. The equation assumes one dust component with one temperature, one mass and one composition. The dust puffs are most likely of quite complex structure and composition, with dust of different sizes and temperatures. Since we do not know the exact composition and size distribution[3], one can just assume a single mineral type (single dust composition), which has been conventional. Rewriting Eq.

[3]Though it should be mentioned that for $\lambda \gg a$ (a = grain radius) the grain size are less relevant (Rayleigh-Jeans approximation), but it still affect the value of β.

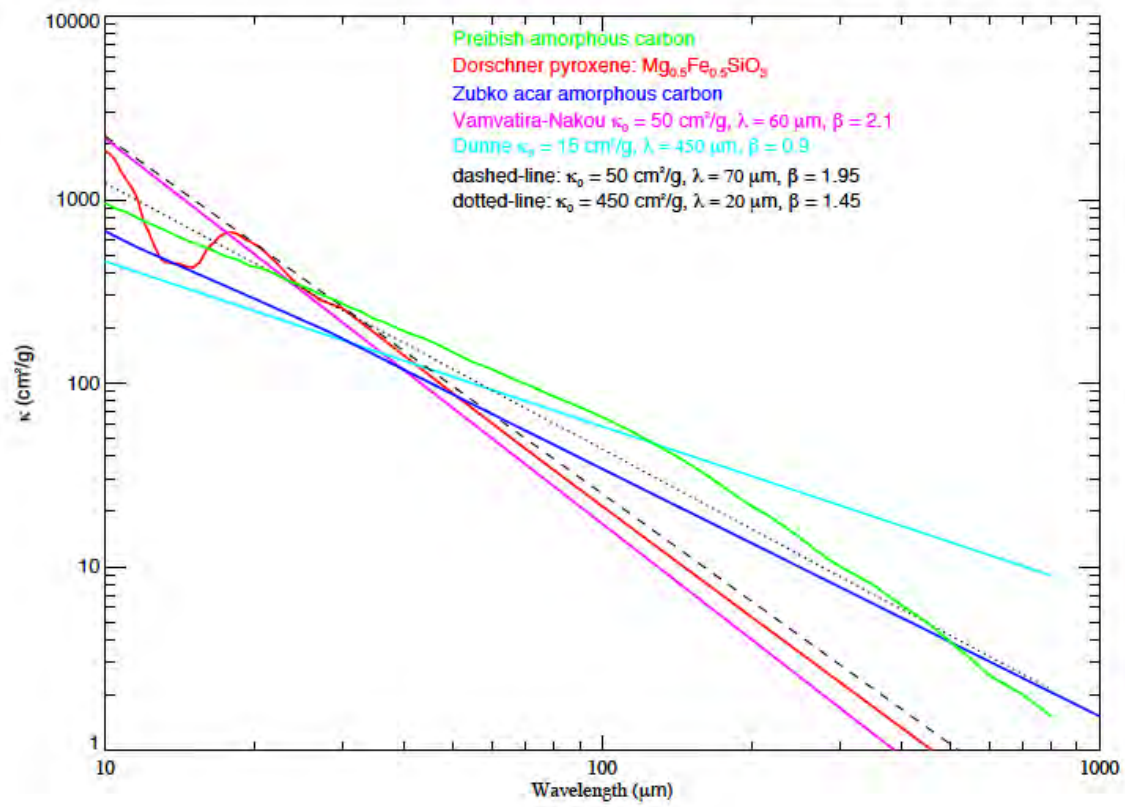

Figure 4.5: κ as a function of wavelength for various dust models. The dashed-line is the silicate fit of Dorschner et al. (1995) (red) and the dotted-line is the carbon fit of Zubko et al. (1996) and Preibisch et al. (1993) (blue & green, respectively). The slope determines the β parameter. Additionally, the models used by Vamvatira-Nakou et al. (2013) and Dunne et al. (2003) are also shown.

4.5 to account for two dust components (i.e two temperatures and dust masses) gives us:

$$F_\nu = \frac{\kappa}{D^2} \left[M_1 B_\nu(T_1) + M_2 B_\nu(T_2) \right], \tag{4.7}$$

where the subscripts refers to dust component 1 (warm) and 2 (cold). Each component has its own mass and temperature (in form of the black-body from Eq. 4.3) but both components are assumed to have the same mineralogy, i.e. same absorption features in form of κ.

In the case of the outer shells a single dust component should be sufficient since there is no apparent flattening of the SEDs. Also, the second shell should have had longer time to reach thermodynamic equilibrium and the dust grains should be more or less of the same structure, size and composition.

5 Results

In the following section I present the results from the analysis of the dust from both the inner and outer shell. This includes the determination of the extent of the shells, the flux densities and the resulting SEDs as well as the dust masses and temperatures obtained from fitting these.

5.1 Inner Shell

Using the aperture slice feature from APT, I found the extent of all the shells and the appropriate radii for the annuli. The location and aperture slice for each object is shown in Fig. 5.1. The red line marks the aperture and the green and yellow marks the inner and outer radius of the annulus, in which the sky contribution has been determined.

Some of the objects have small bumps when you move away from the center. This might be due to an interfering bright object in the foreground or the background as in Fig. 5.1g, which has multiple objects within the outer sky radius. In other cases it could be due to a ring structure of the shell as in Fig. 5.1i. This would suggest a shorter outburst rather than a continuous wind driven mass-loss.

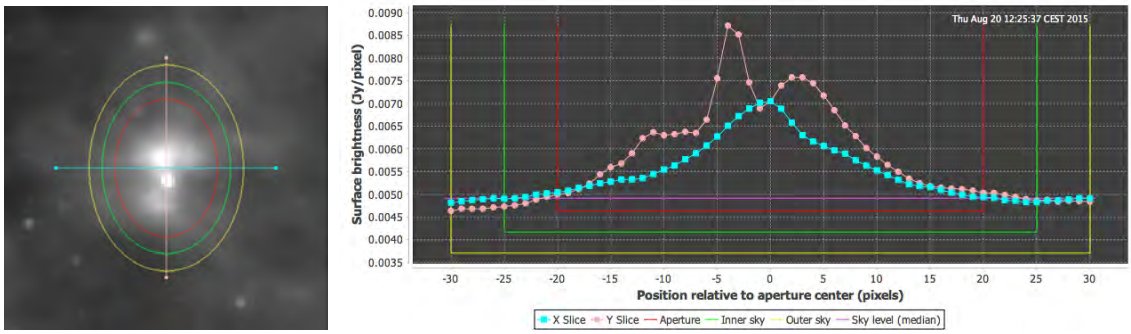

(a) MN14

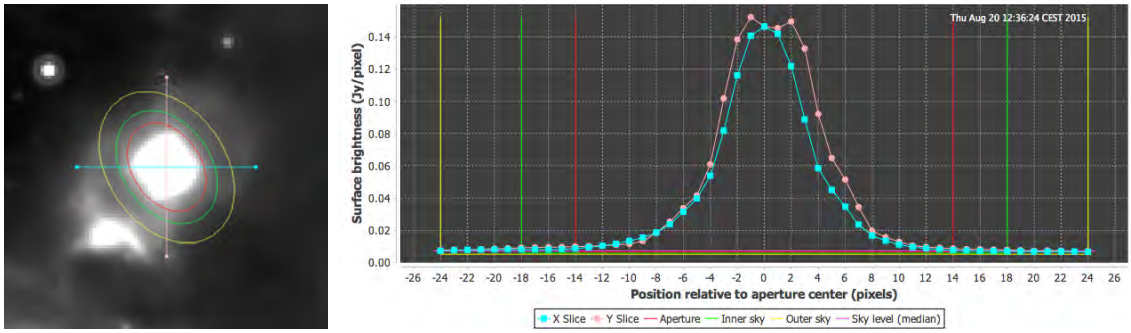

(b) MN18

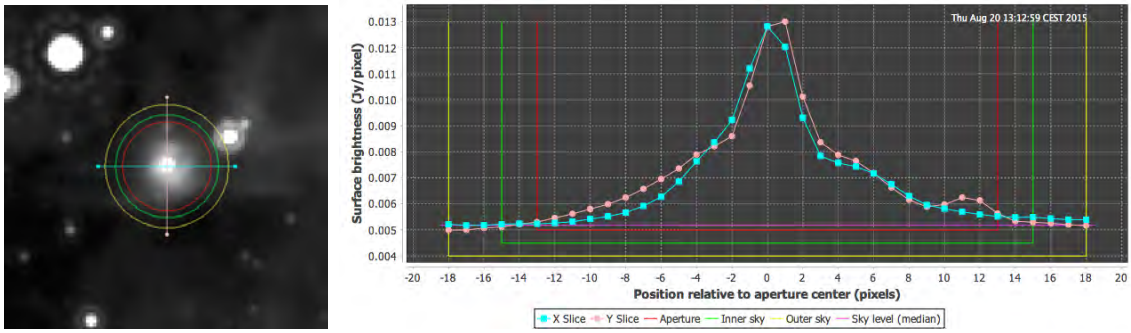

(c) MN19

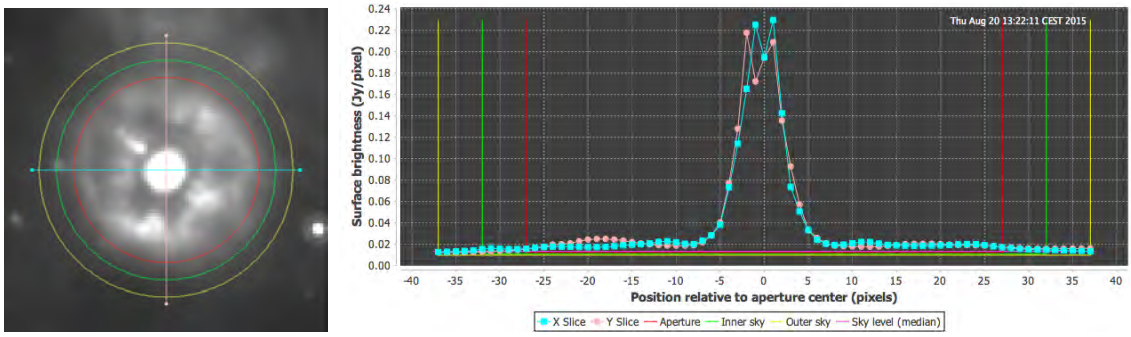

(d) MN46

Figure 5.1: The left figures show the location of the aperture and annulus of each target's inner shell in the MIPS-24 μm frame. The graphs to the right show the aperture slice with flux counts vertically and horizontally from the center of the target. The radii in the bottom are given in pixels.

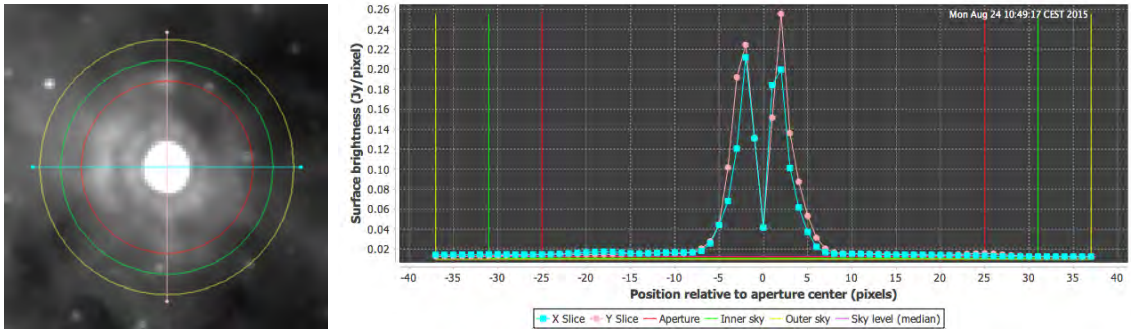

(e) MN64

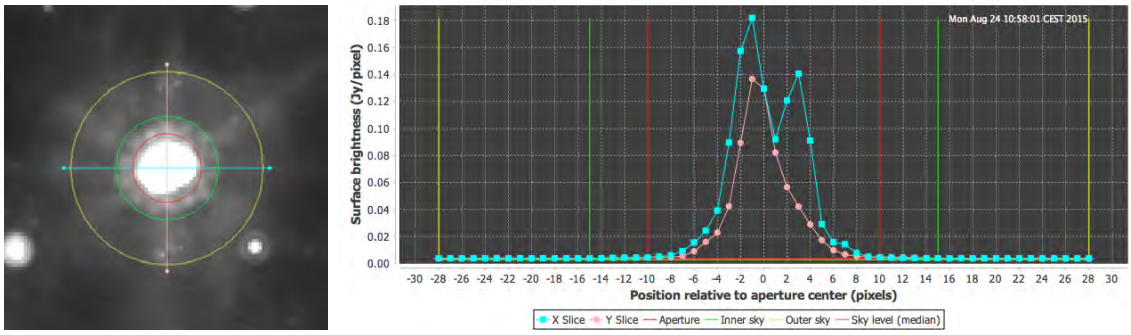

(f) MN111

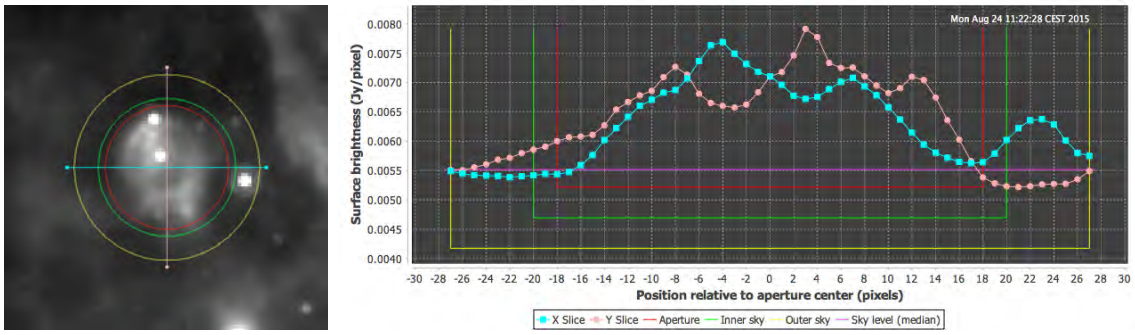

(g) W5

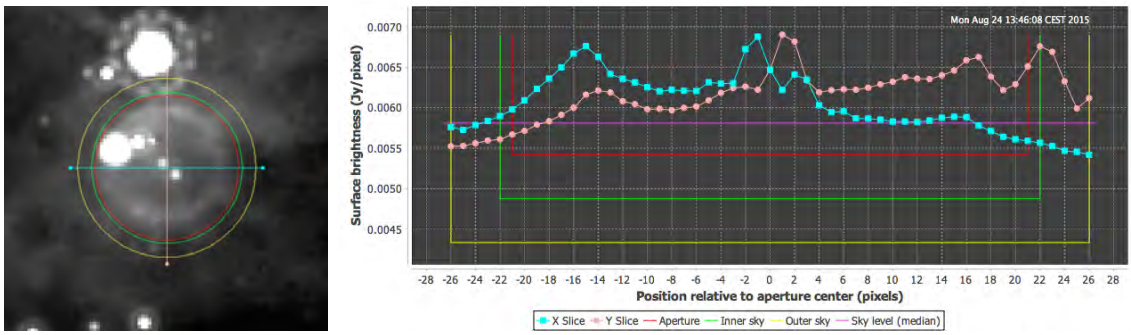

(h) W8a

Figure 5.1: – *Continued*

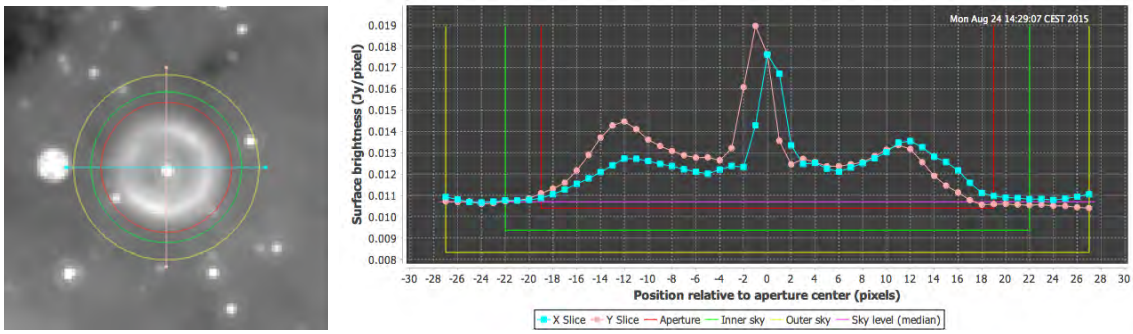

(i) W27a

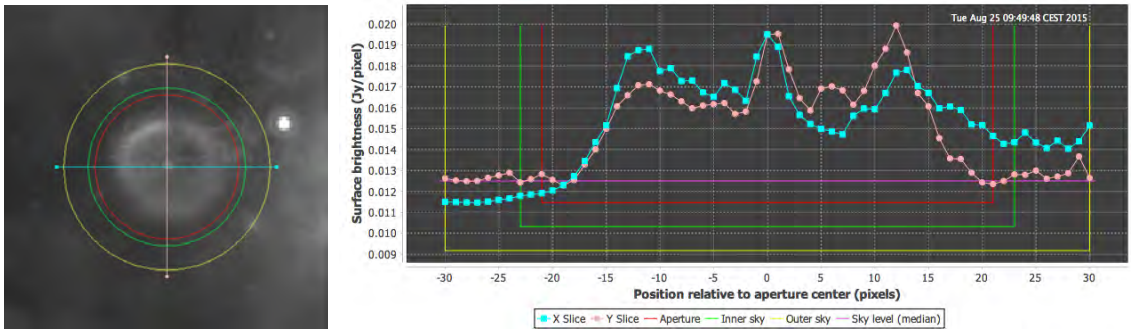

(j) W43

Figure 5.1: – *Continued*

From aperture photometry I obtained the flux densities in the various wavelength bands from *Herschel* and *Spitzer*. The target list and their respective flux densities are shown in Table 5.1. The large uncertainties on the SPIRE measurements are due to the weak detection in these frames. Using these results and the converted magnitudes from Wachter et al. (2010) and Gvaramadze et al. (2010) I initially fitted a two component black-body function: one for the dust (a total dust component including both the warm and cold component) and an even hotter one for the stellar contribution, a "central source" component, so to speak. This was done to see if the points from Table 5.1, especially the MIPS-24 μm point, belonged to the dust component or if it contained too much radiation from the central source. The function is the same as Eq. 4.7, but the temperature is much hotter ($\geq$ 1000 K) and the mass is some orders of magnitude smaller:

$$F_\nu = \frac{\kappa_\nu}{D^2}\left[M_1 B_\nu(T_1) + M_2 B_\nu(T_2)\right], \tag{5.1}$$

where M_1 and T_1 refers to the warm dust component and M_2 and T_2 to the hot central

Table 5.1: Inner Shell Flux Densities

	MIPS	PACS		SPIRE		
Target	24μm	70μm	160μm	250μm	350μm	500μm
	(Jy)	(Jy)	(Jy)	(Jy)	(Jy)	(Jy)
MN14	0.71±0.11	8.5±1.7	8.7±1.8	2.5±0.7	0.6±0.4	<0.3
MN18	10.5±1.8	9±2	1.7±0.4	0.22±0.11	< 0.12	< 0.05
MN19	0.51±0.08	6.8±1.4	4.4±1.0	< 0.9	< 0.6	0.3
MN46	21±3	60±12	59±12	24±5	9±5	2.1±1.0
MN64	13±2	5±2	...	...	...	...
MN111	5.6±1.0	78±18	61±13	25±4	9.3±1.7	2.54±0.14
W5	6.6±1.0	3.4±0.7	...	...	...	...
W8a	0.84±0.14	7.2±1.8	3.3±1.8	< 5	< 4	< 2
W27a	1.9±0.3	18±4	11±2	1.6±1.4	< 1.7	< 0.5
W43	3.5±0.5	40±8	27±8	9±5	< 7	< 1.8

Notes. The targets' inner shell flux densities in each of the *Herschel* PACS and SPIRE frames as well as the *Spitzer* MIPS-24 frame. All the flux densities are given in Jy with an uncertainty of one σ.

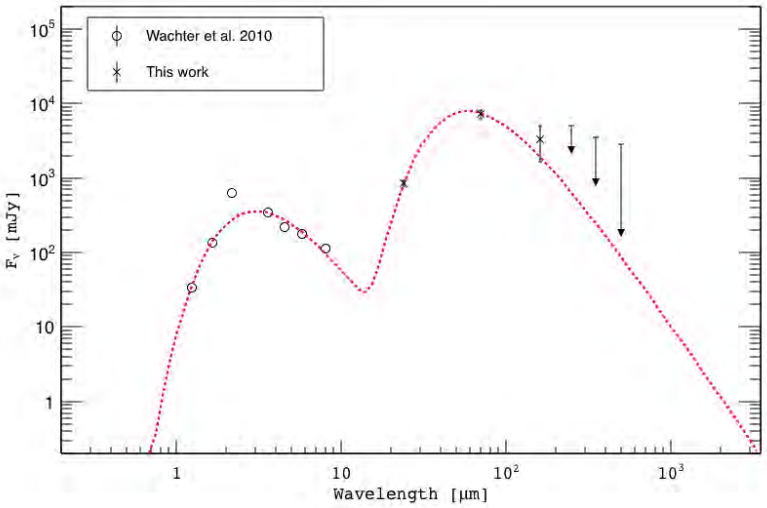

Figure 5.2: The SED of W8a with two temperature components. The circle points indicates the results taken from Wachter et al. (2010), where the rest is from this work. The red dashed line shows the modified black-body function with two components: a hot and a warm. The MIPS24μm point clearly belongs to the warm component. Upper limits are indicated as arrows.

source component. An example of this is shown in Fig. 5.2. The same dust model has been used for both components which might not be very accurate, but this was also done purely for show.

Figure 5.2 shows the SED of the target W8a made from the magnitudes (converted into Jy) from Wachter et al. (2010) at the shortest wavelengths and the results I found at longer wavelengths. It is easy to see that the points from 24μm and up belongs to the dust component. Since the mass contribution from the "central source" component is very small compared to that of the dust component ($\sim 10^7$ times smaller), I chose to only use the points I found (from Table 5.1) and fit these to find the dust mass in the shell. The results are shown in Fig. 5.3, where all the target SEDs have been plotted along with their respective fits.

All the targets have been fitted with two different dust models as mentioned in Sect. 4.2.2. The model parameters are found in Table 4.1. Some of the targets have only been fitted with a single dust component such as MN18, which does not show any signs of "flattening" on the top of the SED. And since we only have two points on the SED of MN64 and W5, there is no point in fitting a double component, though it can not be ruled out that it does have an extra component. However, since these targets are the only ones with their PACS-70 μm point lying lower than their MIPS-24 μm, this indicates that what we are in fact fitting is the cold dust component which contains most of the dust mass. The same is almost the case for MN18, where the MIPS-24 μm and PACS-70 μm are about the same value.

Furthermore, the SEDs has been *bootstrapped* around 12 μm, meaning the flux at this point was limited to $F_{12\,\mu\mathrm{m}} = 0.00 \pm 0.01$ Jy. This was done to prevent the fit from making a "*camel*" rather than the flattening at the top of the SED. This was not done in the cases of MN18 ($F_{12\,\mu\mathrm{m}} = 0.0 \pm 0.1$ Jy), MN64 and W5 because of the single component fit and their relatively warmer dust component. The impact of the bootstrap will be further discussed in Sect. 6.1.

Since we do not know the exact distance to the objects the fits are giving us the dust mass as a function of this (which is in order of $M_\mathrm{d}(D) \simeq 10^{-12}\,\mathrm{kg\,m^2}$). These number can be difficult to relate to anything so I choose to present the dust masses as if the stars all have the same distance of 5 kpc. The Milky Way is approximately 30 kpc in diameter and the Sun is about 8 kpc from the center, which gives us an upper limit of the possible distance (not taking the obscured view by the galactic center into account) of 22 kpc. In the direction away from the galactic center we have a max distance of 7 kpc. Since the mass scales as $\propto$ D^2, I choose to use 5 kpc as a "golden middle way" to exclude getting too high or too low a dust mass (though we can not know for sure that the stars are as far away as ~20 kpc or as close as ~ 500 pc).

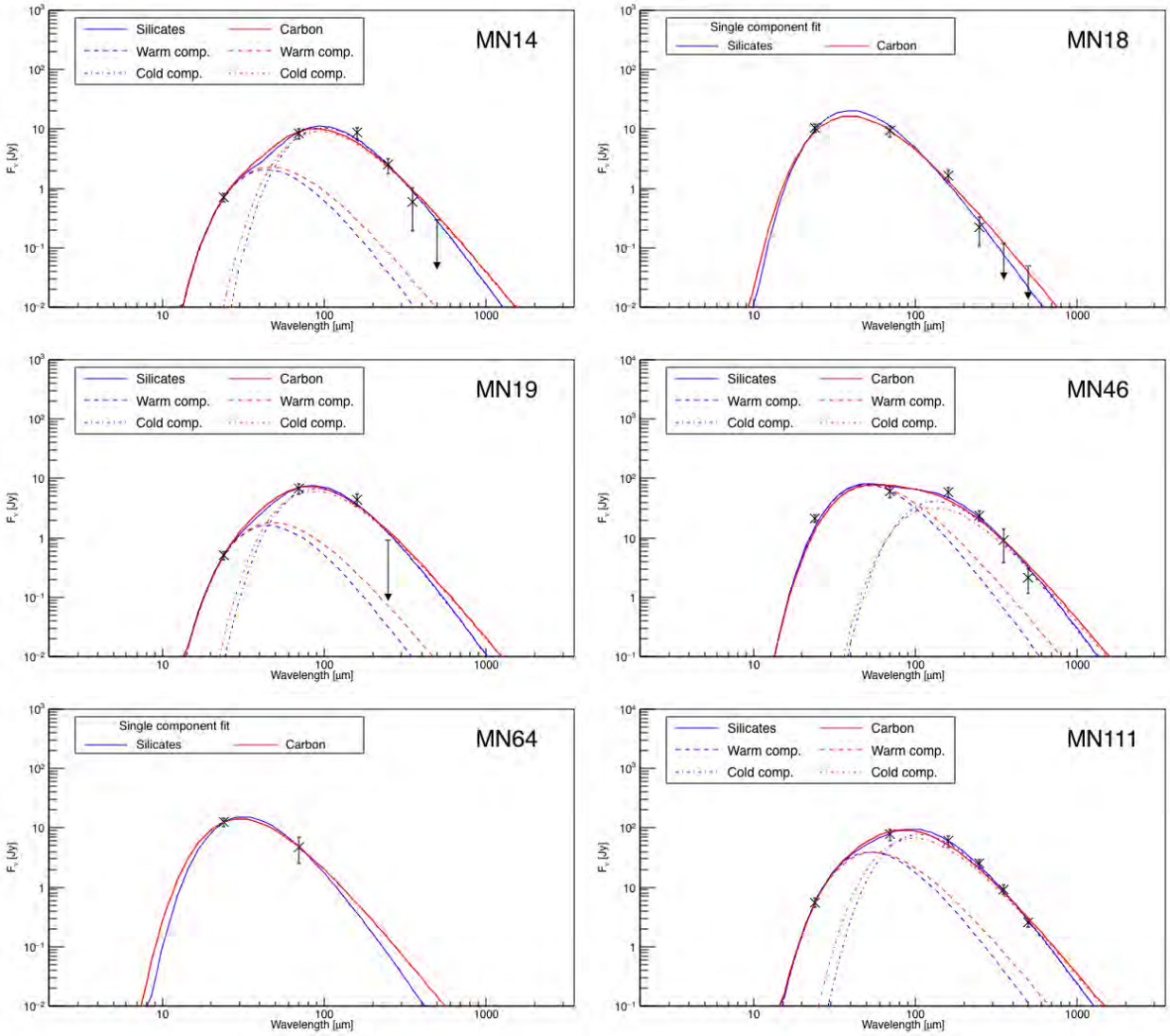

Figure 5.3: SEDs fittet with a modified black-body function. Each SED is fitted with black-body functions based on two different dust models. The blue lines corresponds to the fit using the silicate-model, whereas the red are for the carbon-model. The contribution from the two components are plotted as the dashed line (warm component) and the dash-dotted line (cold component). Upper limits are indicated with arrows. MN18, MN64 and W5 are fitted using only a single dust component. The target name is noted in the upper right corner on each plot. Note that MN46 and MN111 has slightly different flux scales than the others.

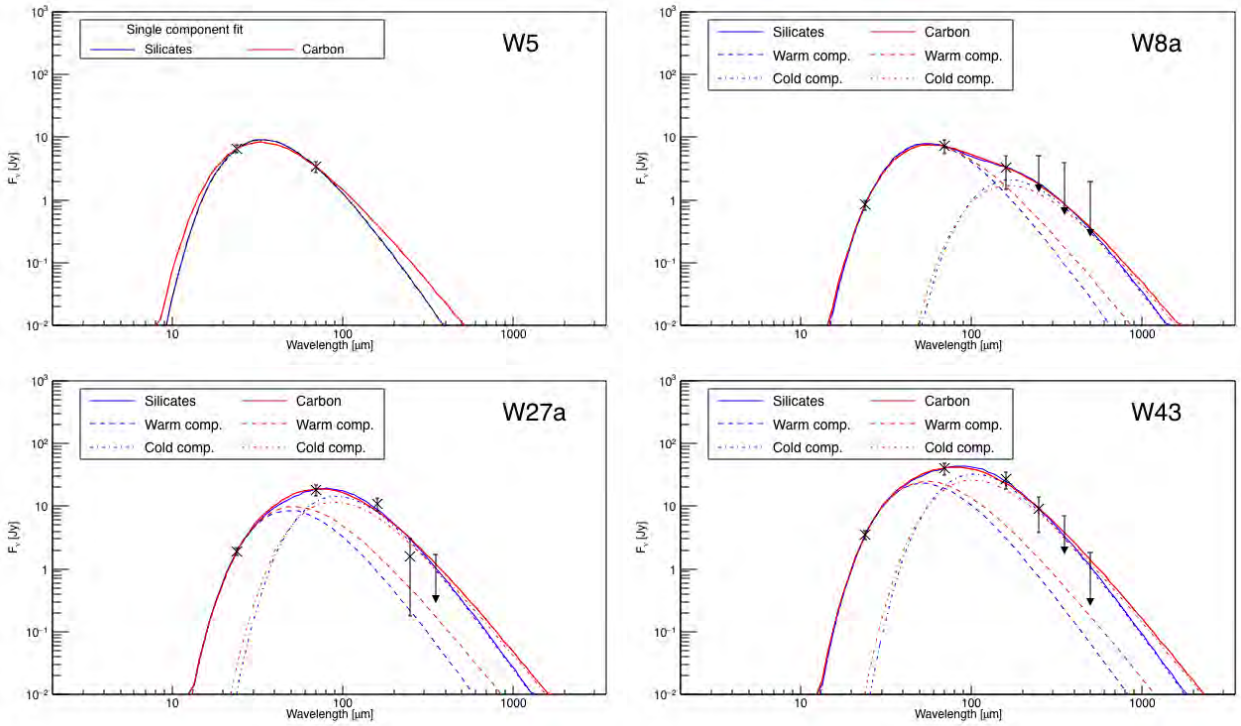

Figure 5.3: – *Continued*

The results from the fits are shown in Table 5.2 and the total dust mass has been calculated for a distance of 5 kpc, such that:

$$M_{5\mathrm{kpc}} = M_{\mathrm{d}} \times \left(\frac{D}{5\,\mathrm{kpc}}\right)^2, \tag{5.2}$$

where M_{d} is the mass coefficient we get from the fit. In the case of a two component fit M_{d} is the sum of both dust mass coefficients. For each of the targets you get quite different results depending on which dust model you use. Comparing the two models we see that the silicate-based model yields $3-5$ times as much dust as the carbon-based one. These masses span from a few parts of a thousand to a few solar masses (W5 with $\mathrm{M}_{5\mathrm{kpc}}$ =0.0010 $\mathrm{M}_{\odot}$ and MN46 with $\mathrm{M}_{5\mathrm{kpc}}$ =2.9 $\mathrm{M}_{\odot}$).

The temperatures seem to be fairly consistent. The warm component lies in the range of $50-90$ K and the cold one in the range $20-40$ K. A few targets have some rather large uncertainties, i.e. the cold component of W8a and the warm component of MN19. The temperatures obtained from the carbon-based model are slightly higher, but still within the uncertainties.

Table 5.2: Inner Shell Dust Masses and Temperatures

Model:		Silicates			Carbon		
Target	Size ($''$)	M_{5kpc} ($M_\odot$)	T_w (K)	T_c (K)	M_{5kpc} ($M_\odot$)	T_w (K)	T_c (K)
MN14	36.75×49	0.16	67 ± 18	30 ± 2	0.04	70 ± 17	35 ± 3
MN18[a]	34.94×24.5	0.004	73 ± 3	–	0.0014	83 ± 3	–
MN19	31.85	0.06	65 ± 34	33 ± 5	0.018	68 ± 38	38 ± 8
MN46	66.15	2.9	59.1 ± 1.5	22 ± 2	0.6	62.4 ± 1.7	25 ± 3
MN64[a]	61.25	0.0012	90 ± 11	–	4×10^{-4}	108 ± 16	–
MN111	21.9	1.7	56 ± 7	28 ± 3	0.3	60 ± 7	34 ± 4
W5[a]	41.1	0.0010	84 ± 5	–	3×10^{-4}	99 ± 7	–
W8a	51.45	0.5	53 ± 3	17 ± 17	0.09	58 ± 3	20 ± 26
W27a	46.55	0.16	61 ± 13	32 ± 5	0.04	63 ± 13	37 ± 9
W43	51.0	0.6	56 ± 11	28 ± 7	0.17	60 ± 10	32 ± 9

Notes. [(a)] Single dust component fit.

5.2 Outer Shell

As well as for the inner shell I have found the flux densities for the outer shells. However, only for four targets (out of the ten I have used) with the most visible and definable outer shells (W27a did in fact also show sign of an outer shell, but because of problems with the background determination, i.e. great variations from location to location, I chose to exclude this from further analysis). Since the outer shell is not visible at shorter wavelengths, i.e. the MIPS-24 μm, only the *Herschel* frames has been processed. In Table 5.3 the four targets are listed with their flux densities for the outer shell in all the *Herschel* frames. The fits for these results are shown in Fig. 5.4 and the results from the fits are shown in Table 5.4. The temperatures for the dust are listed as

Table 5.3: Outer Shell Flux Densities

	PACS		SPIRE		
Target	70μm (Jy)	160μm (Jy)	250μm (Jy)	350μm (Jy)	500μm (Jy)
MN14	45±16	233±51	145±110	< 141	< 65
MN18	61±20	46±18	< 61	< 38	< 22
MN111	< 38	70±28	57±52	< 67	< 36
W8a	< 219	381±250	196±82	< 264	< 139

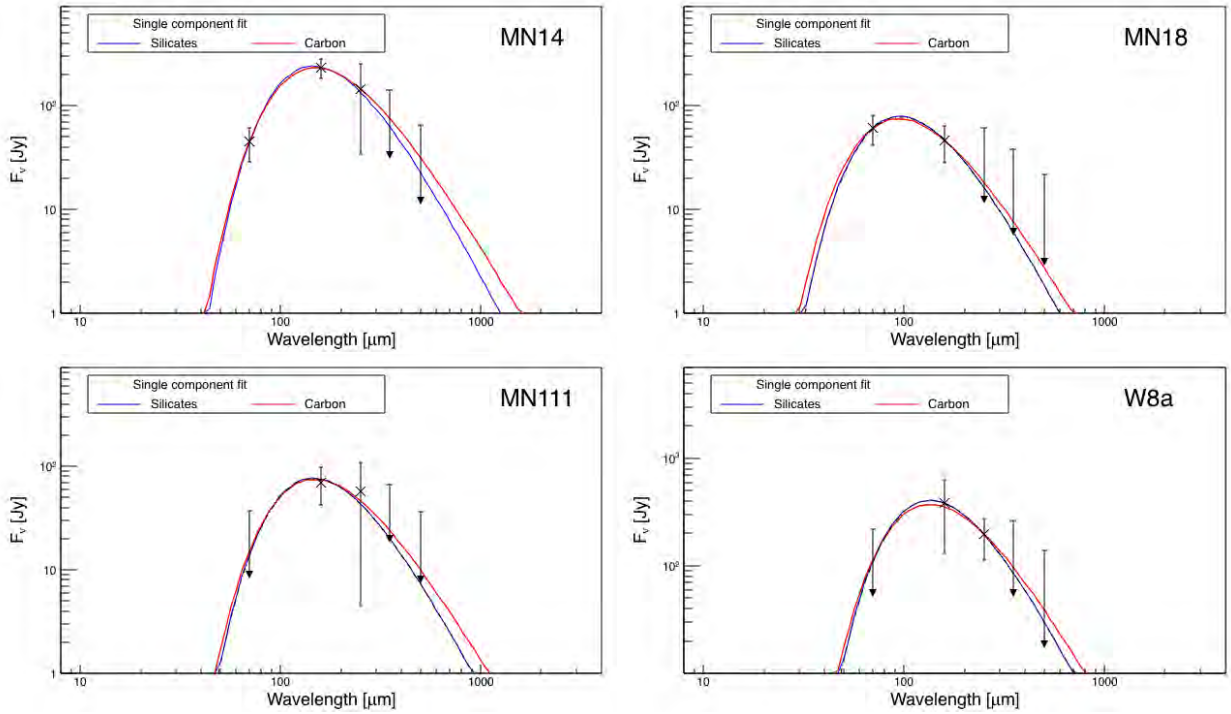

Figure 5.4: The SEDs for the outer shells fitted with both the silicate- (blue line) and the carbon-based (red line) dust model. The fit consists only of one dust component. The target name is shown in the upper right corner. Arrows indicate upper limits. Please note that W8a has a slightly different flux scale.

Table 5.4: Outer Shell Dust Masses and Temperatures

Model:	Silicates		Carbon	
Target	$M_{5\,kpc}$ ($M_\odot$)	T (K)	$M_{5\,kpc}$ ($M_\odot$)	T (K)
MN14	25	20.1 ± 1.4	8	21.9 ± 1.6
MN18	1	31 ± 4	0.3	35 ± 6
MN111	8	20 ± 5	2	22 ± 5
W8a	29	22 ± 3	8	24 ± 4

Notes. The mass are listed for both dust models with an assumed distance of 5 kpc.

well as the masses.

Since the dust in the outer shells are further away from the star, it is not exposed to the same amount of radiation coming from the star, hence it has a lower temperature as expected. Because of this lower temperature the dust most likely has a different composition compared to the dust from the inner shell, e.g. larger grains and more

complex molecules, likely because they have had more time to collide and to condensate. I have, nevertheless, still used the same two models as for the case of the inner shell, though it might not be absolutely correct. Also, I have only used a single component fit (Eq. 4.5) since there are no obvious signs of an extra component due to flattening of the SED and the dust should have had more time to reach an equilibrium temperature.

Here we also see quite different results when comparing the two models. An overall difference of a factor ~ 3 in favour of the silicate-based model. Half the sample yields very high masses from the silicate model of 25 and 29 $M_\odot$ (MN14 and W8a, respectively), which suggest that we might be overshooting the distance of 5 kpc. It could also be due to poor background subtraction, since it was sometimes difficult to distinguish the outer shell's emission from the general background emission. The targets MN18 and MN111 gives more reasonable results of 1 to 8 $M_\odot$, respectively. The output from the carbon-based model is more sensible for all the targets with masses in the range $0.3 - 8\ M_\odot$.

As for the inner shell, the temperatures are also fairly consistent for the outer shell with values about $\sim 20 - 30$ K, the exception being W8a that has higher temperatures for the outer shell than for the inner shell, which is in contradiction to what we expect. However, the temperatures for W8a's inner shell has quite large uncertainties, so it is difficult to say if the dust from the inner shell in fact is colder than that of the outer shell.

6 Discussion

6.1 High Mass Stars as Dust Factories

6.1.1 The Inner Shell

The greatest uncertainty on my results is inevitably the unknown distances to my objects. Since we expect all the targets to be located within the Milky Way, they can have distances in the range of a few hundred parsecs up to tens of kpc. And since the mass scales as $\propto D^2$ this could affect the results quite significantly. The further away, the more dust. If for example the star MN14 lies closer than 1 kpc its dust shell would contain $< 0.002\,M_\odot$ (using the carbon model), but it would contain $\sim 0.6\,M_\odot$ if it instead has a distance of 20 kpc (a factor 300 higher). Comparing to the silicate model it only has to be at a distance of 12.5 kpc to have a dust shell of $1\,M_\odot$.

In general the fits are just, or barely, constrained by the number of data points (4 parameters vs. 6 data points, in most of the cases). In the case of MN64 and W5, which only have 2 points, these can of course be fitted with anything. They have therefore only been fitted with a single dust component. When looking at the SEDs it can be seen that both their MIPS-24 μm points lie above their PACS-70 μm which could indicate that this in fact is the cold dust component, though slightly hotter than compared

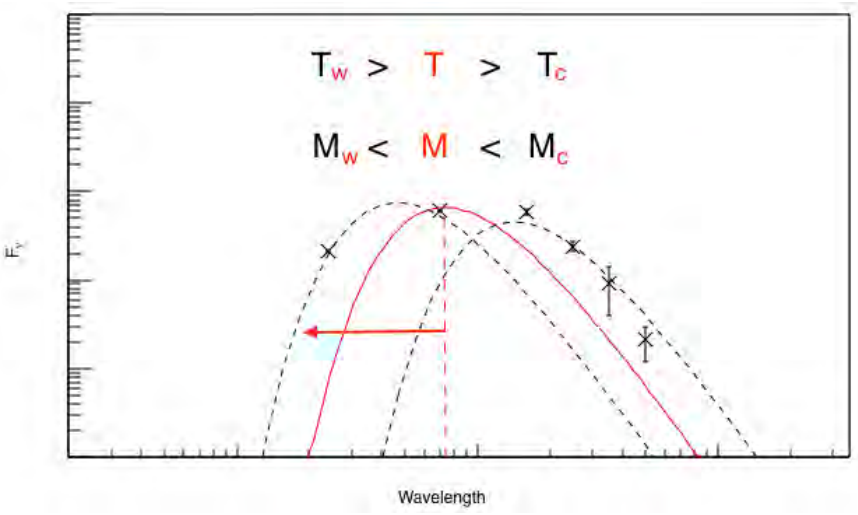

Figure 6.1: Illustration of how fitting a single dust component to the SED gives a bias on the dust temperature and the dust mass. The black dashed lines symbolizes the warm (left) and the cold (right) components from the double component fit and the red line symbolizes the single component fit. Moving the peak (red dashed line) towards lower wavelengths gives a higher temperature and a lower dust mass than comparing to the cold component of the double component fit.

to the other targets'. Since the majority of the dust mass is found in the cold component, these can be seen as upper limits to the dust mass. The last case where a single component has been used is MN18. This target also have comparable values of fluxes at 24 and 70 μm which could also indicate a hotter cold component.

However, there might be a bias on the single temperature component fit. If there are in fact two dust components the temperature will be overestimated (biased towards higher temperatures) since the fit will be "placed" between the two components. This has been illustrated i Fig. 6.1. If this is the case then the dust mass itself will be underestimated (biased towards lower values) as indicated on the figure.

Another thing that could affect the results, at least for the inner shells, is the bootstrapping I used for the SED fits (Sect. 5.1). As mentioned earlier, the bootstrapping was done to prevent the warm component from being fitted with a too high temperature, creating the so-called "camel" fit. An example of this is shown in Fig. 6.2. The effect of the bootstrap means that the warm component gets a lower temperature and hence also a higher mass coefficient than otherwise. However, the mass contribution from the warm component are about 3 orders of magnitude lower than that of the cold component. One could have fitted the SEDs with an additional component, but

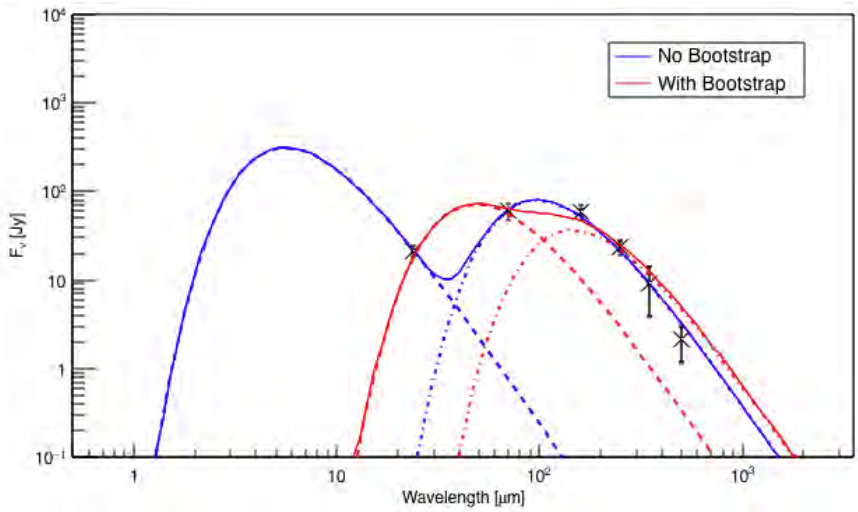

Figure 6.2: An example of how the bootstrap affects the fit. The blue lines are the resulting fit with no bootstrapping and the red are the resulting fit with bootstrap $F_{12} = 0.0 \pm 0.01$. Without the bootstrap the warm component gets a significantly higher temperature and a significantly lower mass coefficient, creating the "*camel*" fit.

this would only introduce even more parameters to an already poorly constrained fit. Omitting the bootstrap would also cause the aforementioned temperature bias on the cold component, which would result in a significantly lower dust mass.

Comparing the dust masses from Table 5.2 to what others have found, we see that the results are somewhat comparable. For example the dust mass of $0.125\,M_\odot$ derived for the *Homunculus Nebula* of η Carinae (Smith et al., 2003) are of about the same order (still assuming our targets to have distances of 5 kpc, however). The circumstellar Homunculus Nebula was ejected in the mid 19th century during the *Great Eruption* which lasted about 20 yr. This implies a total mass-loss rate of about $\dot{M} \geq 0.5\,M_\odot\,\mathrm{yr}^{-1}$, but could be higher due to a "conservative" dust-to-gas ratio of ~100 (perhaps by a factor 2).

Guha Niyogi et al. (2014) studied the dusty environment of the LBV R71 in the Large Magellanic Cloud (LMC) and found that the circumstellar dust shell contains about $0.01\,M_\odot$ made up mostly of amorphous silicates but also carbonaceous material. They derive a time-averaged mass-loss rate of $\dot{M} = 2.5 \times 10^{-6}\,M\,\mathrm{yr}^{-1}$ over ~ 4000 yr, and by assuming the same mass-loss rate for additionally 5 confirmed LBVs in the LMC they get a combined mass-loss rate for the six objects of $\dot{M} = 1.3 \times 10^{-5}\,M\,\mathrm{yr}^{-1}$, which is comparable to the mass-loss rate of all the AGBs and RSG in the LMC.

The study of a cLBV by Agliozzo et al. (2014) using *Herschel* data, shows an ejecta of $0.02\,M_\odot$ warm dust with temperatures in the range $60 - 85$ K. The dust grains are dis-

tributed throughout three concentric shells made of mixed silicate and graphite grains. They furthermore estimate a mass-loss rate of $\sim 6.5 \times 10^{-5}\,\mathrm{M\,yr^{-1}}$ which is comparable to that from Guha Niyogi et al. (2014).

6.1.2 The Outer Shell

The resulting dust emission depends a great deal on the background determination, which in some cases varies a lot. The star W27a did show signs of an outer shell but I chose to eliminate this for further analysis because of difficulties with the background. The remaining 4 targets had more consistent background emission and did not vary as much from location to location. There are still high uncertainties implicated with the derived dust masses because of the difficulties in determining the extent of the outer shell.

Vamvatira-Nakou et al. (2013) had a similar case to that of my targets with outer shells. They investigated a double shell around WRAY 15-751, which is an LVB that lies about 6 kpc away. They found that the dust temperature lies in the range of $66-95\,\mathrm{K}$ for the inner shell and about 40 K for the outer shell and about $\sim 0.05\,\mathrm{M_\odot}$ of dust in each shell. Ultimately they derive that a total mass of about $4\pm2\,\mathrm{M_\odot}$ was ejected which corresponds well to a $\sim 40\,\mathrm{M_\odot}$ RSG progenitor star.

If the dust shells are products of episodic outbursts or violent eruptions, one would expect about the same amount of dust in each shell, as is the case of Vamvatira-Nakou et al. (2013). Perhaps slightly higher values for the outer shell since it was created from an initially more massive progenitor, and could have swept up more circumstellar material from previous outbursts/winds or the ISM. This work finds a difference in dust masses from inner to outer shell to be of several factors, which would suggest that the background subtraction might have been insufficient or that the flux included by the aperture might be a partial contribution from the ISM.

6.2 Other Productions Sites of Dust

6.2.1 Supernovae: Dust Production or Destruction?

Turning to supernovae as dust production sites there seem to be significant differences in the results regarding the dust masses produced in SNe and SNRs. SNe seem to be a quite efficient site of dust production with dust masses in the order of tenths to a few

solar masses. However, because of the pending reverse shock created from the frontal shock's encounter with the ambient medium, it is unclear how much of the dust that will in turn survive and make its way into the ISM.

One of the younger SNRs is the well-known and -studied SN1987A. Indebetouw et al. (2014) finds a dust mass of $> 0.2\,M_\odot$ in the remnant's inner ejecta with cold dust temperature of $T = 26 \pm 3$ K, whereas Matsuura et al. (2011) finds a somewhat higher dust mass between $0.4 - 0.7\,M_\odot$ with temperatures of $17 - 23$ K. These results indicate that SNe in fact could be responsible for the majority of the dust mass detected in young galaxies at high redshifts, provided that the dust is not substantially destroyed by the encounter with the reverse shock. Indebetouw et al. (2014) states as a final remark that if $0.23\,M_\odot$ dust is created in a Type II SN and about $0.1\,M_\odot$ of that dust survives/passes through the reverse shock and into the ISM, then Type II SNe could dominate the dust production in galaxies at all redshifts. This would imply a survival rate of $40 - 50\%$, which compared to other results seem to be quite large and optimistic.

Nozawa et al. (2007) find, from theoretical studies, that the total mass fraction of dust that is destroyed in SNRs is between 0.2 and 1, which increases with the density of the ambient gas as well as the explosion energy of the SN. Another theoretical study by Bianchi and Schneider (2007) finds a destructive pattern of the reverse shock with dust survival rates between $2 - 20\%$ of the initial dust mass over a period of $4 - 8 \times 10^4$ yr. However, they still conclude that core-collapse (Type II) SNe could be major dust contributors, with $0.1 - 0.6\,M_\odot$ dust mass formed in the ejecta of $12 - 40\,M_\odot$ stellar progenitors. Both papers suggest that it is primarily the small grains which are destroyed by the reverse shock and the large grains (which contains most of the mass) that survives without significant decrease in size.

Observations of the old SN Sgr A (Lau et al., 2015) suggest that the reverse shock has reached the center of the SN. With this in mind they find the dust mass in the remnant which must be the surviving dust of the reverse shock. They find a dust mass of $\sim 0.02\,M_\odot$, and by comparing this to the results from younger SNRs they find a survival rate for the dust that encounters the reverse shock. If a total dust mass of $\sim 0.3\,M_\odot$ was created initially (which is suggested for progenitor stars masses of $13 - 20\,M_\odot$), this would mean a survival rate of 7%. If a lower initial dust mass of $0.1\,M_\odot$ is assumed to be created in SNe, which is comparable to that of Cas A and and the Crap Nebula (Gall et al., 2011), this would infer a survival rate of 20%. If the dust survival rate of the reverse shock is $\sim 10 - 20\%$ it's difficult to explain the observed amount of dust. If the initially produced dust mass is of order $0.5\,M_\odot$, which is suggested by observations of SN1987A (Matsuura et al., 2011; Indebetouw et al., 2014), SNe could in fact be responsible for

producing most of the dust in the early universe.

A rather pessimistic result comes from observations by Lakićević et al. (2015) who actually finds that the SNRs in the LMC removes more dust than they create, with a destruction rate of $0.037^{+0.075}_{-0.025}\,M_\odot\,yr^{-1}$ and a total dust removal of $3.7\,M_\odot$ dust per SNR. This result implies that we in fact should not observe any dust at all, which is a quite interesting result. If correct this would mean that our understanding of dust is much more inadequate than initially anticipated, and a new production site or mechanism is required to explain our observations.

6.2.2 The Slow but Steady AGB Stars

For a long time the AGB stars were the most favored production sites for dust. But since newly observations of dust at high redshift galaxies have come forth, these have been more or less eliminated as significant contributors in the early universe, because of the timescale discrepancy. With initial masses in the range $0.8-8\,M_\odot$ the AGB stars lose up to $\sim 80\%$ of their masses and form circumstellar envelopes of gas and dust (Gall et al., 2011). This happens over a quite long period and since it takes about $\sim 10^9$ yr for a star to reach the AGB phase, these are considered as a more long term investment of dust.

The AGB stars has typically mass-loss rates in the order of $10^{-7}-10^{-5}\,M_\odot\,yr^{-1}$ (Gall et al. (2011), and references therein). The famous Helix nebula has been studied in detail by many, and Van de Steene et al. (2015) finds total dust mass of $3.5\times10^{-3}\,M_\odot$. In the cases of S Scuti and RT Capricorni (Mečina et al., 2014) a dust mass of $(7\pm2)\times10^{-5}\,M_\odot$ and $(1.0\pm0.2)\times10^{-5}\,M_\odot$, respectively, as well as dust mass-loss rates in the order of $\sim 10^{-8}\,M_\odot\,yr^{-1}$.

7 Conclusion

7.1 Can we eliminate massive stars as contributors of dust to the ISM dust budget?

Until recently we have only been looking at old evolved stars as the primary formation site of dust. Over the past decade there has been a growing interest in SNe and SNRs as dust factories but because of the destructive nature of the SN explosion, astronomers has tended to disregard high mass stars as an option. But can we eliminate high mass stars as contributors to the ISM dust budget?

The new developments in IR telescopes has opened for more detailed studies of dust around and in SNe and SNRs, but also around high mass stars. Using recent observational data from *Herschel's* PACS and SPIRE instruments (and *Spitzer's* MIPS) I have found the dust contribution as a function of distance for a sample of 10 stars, selected from a larger population of ~ 150 stars identified with *Spitzer*, located in the Milky Way. Using aperture photometry I determined the sample's SEDs and by fitting these with a double component modified black-body function I have found the mass coefficients and the temperatures of the warm and cold dust in the envelopes. The results suggest that a single dust puff around a massive star could contain between $0.001 - 2.9\,M_{\odot}$ of

dust assuming a distance of 5 kpc, and with a minimum of 0.1 $M_\odot$ per SN to explain for the amount of dust we see in early high redshift galaxies, it looks as high mass stars could be able to produce a substantial fraction of this.

Mass-loss is in general very important when it comes to high mass stars. The stars start to lose mass very early in their lives on the main sequence and continues to do so throughout the following phases, determining the way of evolution. And with higher rates of $\dot{M}$ than compared to old low and intermediate mass stars, they shed off quite a bit of gas and dust, sometimes during short periods of time. Especially the LBV class with their large eruptions and explosions where the escaping material can attain high enough velocities to escape the pending SN blast wave.

LBV and WR winds (see Table 2.1) can attain velocities of about 1000 km s^{-1}, and if the dust needs to get about a parsec away for it to survive the explosion it will take < 1000 yr. However, in violent outbursts like the case of η Car, the escaping material can reach velocities as high as 5000 km s^{-1}, which will mean the dust only needs < 200 yr to reach the 1 pc mark (this of course provides that the material can maintain its high velocities). If a massive star undergoes about 3-5 major outbreaks, corresponding to 3-5 dust shells, during its post-main sequence phase with about 0.05 $M_\odot$ dust per shell (which is about 50% of what we need from a SN to explain the dust present at high redshift), we will end up with about $0.15 - 0.25\,M_\odot$ dust per star. Assuming an average survival rate of 20% (average because the dust in the inner most shells probably will be more affected) after the SN and reverse shock, it will result in $0.03 - 0.05\,M_\odot$ dust per massive star, which is about half the outcome we need from a SN.

It seems that high mass stars could in fact be important contributors to the overall dust budget, producing a noticeable amount of dust. More concrete results will help answering the question, when the distances to the objects has been determined, but as of now it seems that high mass stars should not be neglected as formation sites of dust if we want to understand the origin of the dust present in the ISM of galaxies.

7.2 Future Work

One of the present shortcomings for being able to determine the amount of dust mass present in the individual dusty rings around each of the high mass stars observed with *Spitzer* and *Herschel*, are that the exact distance to most of these stars are currently unknown. However, this situation is hopefully about to change with the upcoming release of the *GAIA* satellite catalogue during the summer 2016. We expect the catalogue to contain distances for a handful of the dusty high mass stellar sample observed by

Spitzer. The *GAIA* satellite is measuring the positions, distances, space motions and many physical characteristics for one billion stars in the Milky Way, complete to 20th magnitude. The measurement precision, reaching a few millionths of a second of arc, is unprecedented.

The infrared data from the *Herschel* satellite provides the distribution of cold dust around these stars and the position data from the *GAIA* satellite will provide the distance to the stars, making it possible for the first time (once the *GAIA* data is released) to actually estimate the contribution of cosmic dust from high mass stars to the interstellar medium of the Milky Way. Also, follow-up observations with the *ALMA* radio telescope array in Chile would be desirable, to probe the detailed mass loss history and molecule formation, as this hopefully will make it possible to determine the dust formation mechanisms. The aim should be to get enough data to be able to derive dust masses for a more representative sample across the stellar mass function, and to probe the formation sites with a view to understanding the formation mechanism and the dust properties (e.g. FIR emission lines can be used to determine key molecule precursors to dust synthesis, FIR dust emission and UV/optical extinction curves can constrain the composition and grain properties of the dust).

Figure 7.1: Colour-composite image of the Carina Nebula, revealing exquisite details in the stars and dust of the region. Credit: ESO and T. Preibisch

"And in the end, the love you take is equal to the
love you make"

– Sir Paul McCartney, *The End*.

Appendix A

Initial List of Targets

In the following the complete list of *Spitzer* detected dust shells (Gvaramadze et al., 2010; Wachter et al., 2010) are shown along with my preliminary findings. Note that some objects are missing in Table A.2. These stars were also observed by Gvaramadze et al. (2010) and are therefore included in Table A.1.

Table A.1: Targets from Gvaramadze et al. (2010)

Target	RA (J2000)	DE (J2000)	Herschel Data / Comments
MN1	11 44 18.10	-62 45 20.2	No
MN2	12 00 58.82	-63 12 59.9	No
MN3	12 10 13.37	-62 50 58.3	No
MN4	12 17 10.37	-62 06 27.1	No
MN5	12 29 41.70	-62 13 08.4	No
MN6	12 47 17.74	-63 00 34.3	No
MN7	13 10 04.87	-63 11 30.1	No
MN8	13 10 43.84	-63 17 45.8	No
MN9	13 14 57.05	-62 23 53.3	No
MN10	13 19 33.87	-62 38 44.8	No
MN11	13 27 08.11	-62 03 19.8	No
MN12	13 27 17.85	-63 19 28.1	No
MN13	13 42 33.08	-62 48 11.3	No
MN14	14 31 11.00	-61 02 02.1	No
MN15	15 01 35.02	-58 00 26.1	No
MN16	15 07 56.37	-58 18 23.8	SP
MN17	15 13 42.17	-58 53 18.5	No
MN18	15 16 41.00	-58 22 26.0	Clear emission in blue with outer shell (far enough?)
MN19	15 19 59.90	-57 24 15.2	No
MN20	15 31 41.30	-56 08 53.0	No
MN21	15 33 08.10	-56 12 20.0	SP (Clear nebula and possible outer shell)
MN22	15 34 12.01	-55 29 57.4	No
MN23	15 35 26.53	-56 04 12.3	Clear nebula +outer shell, might not produce shell
MN24	15 35 53.00	-55 57 04.6	No
MN25	15 38 56.77	-56 37 22.9	No
MN26	15 45 27.46	-53 56 02.6	No
MN27	15 45 59.14	-53 32 32.5	Nebula in blue, no clear cavity/o-shell
MN28	15 46 51.72	-53 44 58.8	No
MN29	15 48 36.40	-54 30 46.9	No
MN30	15 48 42.07	-55 07 42.2	No
MN31	15 49 05.43	-53 44 12.8	No
MN32	15 49 25.97	-55 13 41.6	No
MN33	15 52 54.77	-52 59 47.0	No
MN34	15 58 11.48	-52 55 50.4	No
MN35	15 58 13.78	-52 57 51.4	No
MN36	15 58 45.84	-54 11 48.9	No
MN37	15 59 18.88	-54 07 37.5	No
MN38	16 05 52.99	-52 50 37.8	No
MN39	16 10 26.55	-51 21 25.3	No
MN40	16 11 32.21	-51 29 06.4	No
MN41	16 26 34.28	-50 21 01.9	No
MN43	16 32 14.11	-47 50 40.1	SP
MN44	16 32 39.95	-49 42 13.8	Nebula in blue (and red) maybe outer shell.

Table A.1: – *Continued*

Target	RA (J2000)	DE (J2000)	Herschel Data / Comments
MN45	16 36 42.78	-46 56 20.7	No
MN46	16 43 16.37	-46 00 42.4	No
MN47	16 46 17.35	-45 08 47.9	SP
MN48	16 49 37.70	-45 35 59.2	Clear nebula in blue, no cavity/outershell
MN49	17 07 23.16	-40 07 41.0	No
MN50	17 07 23.34	-39 56 50.5	No significant detection (of any kind)
MN51	17 08 29.13	-39 25 07.7	No
MN52	17 09 22.37	-40 08 01.2	No
MN53	17 09 24.78	-40 08 45.6	SP
MN54	17 09 33.99	-40 09 10.1	No
MN55	17 11 01.00	-39 45 18.7	No
MN56	17 11 16.69	-39 31 31.3	No
MN57	17 20 08.04	-36 13 23.9	No
MN58	17 37 47.54	-31 37 33.4	SP
MN59	17 39 18.99	-31 24 24.3	No
MN60	17 42 07.62	-26 02 13.4	No
MN61	17 42 14.02	-29 55 36.1	No
MN63	17 43 09.50	-33 51 11.0	No
MN64	17 43 59.85	-30 28 38.5	No
MN65	17 45 40.77	-27 09 15.0	No
MN66	17 47 05.21	-27 25 33.5	No
MN67	17 48 39.21	-26 23 15.9	SP IF
MN68	18 02 22.34	-22 38 00.2	No
MN69	18 02 43.91	-22 37 47.0	No
MN70	18 03 56.68	-22 56 00.0	No
MN71	18 04 39.66	-21 41 34.0	No
MN72	18 04 44.44	-21 50 25.7	No
MN73	18 05 14.84	-23 47 09.3	No
MN74	18 06 12.92	-21 17 45.7	No
MN75	18 06 36.21	-19 53 47.3	No
MN76	18 07 05.17	-20 15 16.3	No
MN77	18 13 31.20	-18 56 43.0	No
MN78	18 17 15.54	-14 53 05.1	No
MN79	18 28 33.41	-11 46 44.2	No
MN80	18 33 39.55	-08 07 08.5	No
MN81	18 33 43.47	-08 23 35.3	SP
MN82	18 37 33.49	-06 46 28.8	SP
MN83	18 39 23.01	-05 53 19.9	SP
MN84	18 41 59.73	-05 15 39.4	SP
MN85	18 42 06.31	-03 48 22.5	SP
MN86	18 42 08.27	-03 51 02.9	SP
MN87	18 42 22.47	-05 04 30.1	SP
MN88	18 42 27.40	-03 56 34.1	SP

Table A.1: – *Continued*

Target	RA (J2000)	DE (J2000)	Herschel Data / Comments
MN89	18 44 54.85	-03 35 38.6	SP
MN90	18 45 55.94	-03 08 29.7	SP
MN91	18 49 27.39	-01 04 20.3	No detection
MN92	18 50 01.97	-00 56 14.3	SP
MN93	18 50 39.80	00 04 45.4	SP
MN94	18 50 47.24	01 04 59.1	SP
MN95	18 51 00.29	-00 32 31.0	SP
MN96	18 51 02.95	-00 58 24.2	SP
MN97	18 53 05.82	00 11 35.8	SP
MN98	19 01 16.69	03 55 10.8	SP
MN99	19 03 29.45	04 07 20.2	SP
MN100	19 04 21.07	06 00 01.2	SP
MN101	19 06 24.54	08 22 01.6	SP
MN102	19 06 33.65	09 07 21.1	SP
MN103	19 07 57.95	07 55 21.5	SP
MN104	19 08 46.19	08 43 29.0	SP
MN105	19 10 04.27	10 43 29.2	SP
MN106	19 13 32.75	08 27 03.1	SP
MN107	19 24 03.34	13 39 49.4	SP
MN108	19 26 58.96	18 46 44.0	Visible nebula in blue, no apparent outer shell.
MN109	19 28 14.58	17 16 23.1	No clear nebula, unlikely outer shell.
MN110	19 30 33.49	18 35 56.7	SP
MN111	19 43 53.19	24 15 31.3	SP
MN112	19 44 37.60	24 19 05.9	No clear nebula, some cavity/outer shell
MN113	19 44 42.96	23 11 33.9	No clear nebula, maybe surrounding gas. Not ideal target.
MN114	20 17 08.12	41 07 27.0	Nothing in the archive
MN115	20 35 16.03	42 20 16.4	Nothing visible

Notes. The last column contains my initial comments and sightings of the objects. SP means the object's coordinates has been observed with the SpirePacs instrument. IF (In Frame) means the target is located inside the frame.

Table A.2: Targets from Wachter et al. (2010)

Target	RA (J2000)	DE (J2000)	Herschel Data / Comments
2	13 01 21.88	-62 44 13.1	SP IF
4	14 21 10.02	-61 38 19.9	SP IF
6a	15 09 28.99	-58 47 43.0	SP IF (Noted)
6b	15 09 29.51	-58 47 55.1	Same (noted)
7	15 25 59.86	-57 04 40.3	SP IF
8b	15 33 06.63	-56 12 21.9	Same
11b	15 48 42.10	-55 07 54.2	SP IF
12	15 55 37.88	-53 43 40.2	SP IF
14	16 29 03.77	-47 46 26.4	SP IF
21	17 05 10.43	-40 53 07.1	SP IF
23b	17 08 29.30	-39 25 15.8	SP IF (noted)
25	17 35 29.42	-32 46 56.2	SP IF
26a	17 37 03.71	-31 47 46.7	SP IF (noted)
26b	17 37 03.94	-31 47 34.9	Noted.
27b	17 37 47.30	-31 37 37.0	Yes sir!
28b	17 39 19.13	-31 24 14.2	No nebula in blue. No clear cavity or outer nebula.
29	17 41 35.43	-30 06 38.9	No
31	17 43 39.08	-24 31 52.5	SP IF (Same as MN67)
33	17 48 14.03	-28 00 53.1	No
34	17 49 35.39	-26 49 30.2	No
35	18 00 57.62	-24 33 46.7	No
40	18 23 34.20	-15 25 07.6	No
41	18 28 41.56	-10 27 05.6	No
42	18 32 17.39	-09 16 13.9	No
44	18 33 55.28	-06 58 38.6	No
45	18 39 32.24	-05 44 20.4	No
50	18 42 46.92	-03 13 17.2	Clear inner shell, maybe outer
58	19 32 52.84	-17 42 30.3	No
59a	19 38 55.10	-21 27 55.0	No
59b	19 38 55.69	-21 27 48.3	No
62a	19 55 02.32	-29 17 17.8	No
62b	19 55 02.49	-29 17 19.8	No

Notes. Same as Table A.1. The missing targets are the ones that overlaps with those from Gvaramadze et al. (2010).

Appendix B

Article in prep: The significance of dust production in Late Type High-Mass Stars to the ISM dust budget

Astronomy & Astrophysics manuscript no. article
March 1, 2016

The significance of dust production in Late Type High-Mass Stars to the ISM dust budget

A. P. Drachmann[1] and A. C. Andersen[1]

Dark Cosmology Centre, Niels Bohr Institute, University of Copenhagen, Juliane Maries Vej 30, DK-2100 Copenhagen, Denmark

March 1, 2016

ABSTRACT

Cosmic dust, that dominate the solid phase of matter in the universe, not only shapes what we observe – observations of star formation, quasars, supernovae and hence dark energy –are all profoundly affected by dust, but the presence of dust also dictates the formation of low- and high-mass stars, the making of planets, and the formation of molecules in space. Yet, we do not know the formation site of most dust. Recent observations by infrared (IR) space telescopes have made it easier to investigate probable production sites of dust such as supernova remnants (SNR) which show promising results of dust production. However, recent observations and theoretical studies suggests that the reverse shock from the supernova (SN) might be destroying significant amounts of the dust.
Lately, a large population of high mass stars with circumstellar dust shells has been found in our Galaxy, which indicate that high mass stars could be contributing to the overall dust budget as well. From a sample of 10 *Spitzer*-detected high mass stars with circumstellar dust shells we use new photometric data from the *Herschel Space Observatory* to determine their spectral energy distribution (SED). By fitting each SED with a two-component black-body function I find the dust masses and temperature of the shells using silicate- and carbon-based models. With a dust minimum of 0.1 $M_\odot$ per SN to explain for the majority of dust produced in early galaxies, the results suggests that late-type high mass stars indeed could be able to produce noticeable amounts of dust. It seems that high mass stars could be an important contributor to the dust budget of the ISM, perhaps on the same level as SNRs.

Key words. circumstellar matter, stars: late-type, stars: mass-loss, stars: high-mass

1. Introduction

Cosmic dust plays a crucial role in the evolution of the Universe by assisting the formation of molecules (Hirashita & Ferrara 2002), which are needed to cool down star forming clouds for the very second generation of solar type stars to be able to form (Schneider et al. 2004). Furthermore dust is critical to the formation of planets [12] providing a clear link between understanding the where and when of dust formation and the epoch of planet formation on a cosmic scale. Finally, dust absorbs ultraviolet-optical light and subsequently re-emits it at infrared/millimeter wavelengths, strongly affecting our view and hence our understanding of cosmic star-formation (Steidel et al. 2005) and quasars (Urry & Padovani 1995), and our lack of understanding of dust remains the major uncertainty in observations of dark energy (Davis et al. 2007).

The dust present in the Milky Way today has for years been assumed to be mostly produced in the envelopes of evolved (age > 1 Gyr), low mass stars (Wilson 2000; [23]; [24]). Observations of the presence of large amounts of dust in very early galaxies (Bertoldi et al. 2003; Maiolino et al. 2004) with ages less than 1 Gyr indicate that even though low mass stars seem to be the dominant dust producers in the present universe, it might not always have been the case.

Theoretical studies (Bianchi & Schneider 2007; Nozawa et al. 2007) indicate that under certain circumstances high mass stars which explode as supernovae may provide a fast and possibly efficient dust formation environment in the early Universe. However direct observational evidence for supernovae as a major source of dust was missing for years as supernova in the local Universe, with the at the time most reliable observations showed only a few 10^{-3} $M_\odot$ produced (Rho et al. 2008; Meikle et al. 2007; Kotak et al. 2009; [30]), well below the cosmologically interesting limit of 0.1 $M_\odot$. Not until the observations of Cas A (Barlow et al. 2010), Crab (Gomez et al. 2010) and the surprising findings by Herschel of SN1987A (Matsuura et al. 2011; 2015) has there been strong observational evidence for supporting the theoretical predictions for efficient supernova dust production in very early galaxies (e.g. [31], [33]). However, a possible major flaw of the predictions for supernovae produced dust at high redshift is that the reverse shock in the supernova might likely destroy all the supernova dust before it reaches into the interstellar medium (Bianchi & Schneider 2007; Biscaro & Cherchneff 2014). A very recent paper by Lakićević et al. (2015) presents observational evidence for supernova in the Large Magellanic Cloud to destroy more dust than they produce, indicating that supernova are also unlikely to be net producers of long-lived dust in galaxies.

High mass stars, however, have another way of producing dust. Close to the ends of their lives, they run through a series of violent, episodic mass loss events (Gomez et al. 2010). These mass losses appear to be highly enriched in dust, as shown by the recent discovery of a population of mid-infrared shells around high mass stars in the Galaxy (Wachter et al. 2010; Gvaramadze et al. 2010), observations of the high-mass variable binary star η Car (Gomez et al. 2010), and observations of supernovae (Smith et al. 2012). The mechanism triggering the mass loss, and the nature and total mass of dust produced and driven off in these ejections are all still unclear (Cherchneff 2013). However, it appears that the outflow velocity of these ejections is sufficient to enable the dust to outrun the most destructive effects of the following supernova (Davidson 1971; Goodrich et al. 1989).

Observations by the MIPS instrument on board *Spitzer* (Multiband Imaging Photometer for Spitzer) discovered a large number (>156) of circular and elliptical shells at 24 μm around luminous central sources. Deep optical and near-infrared spectroscopic observations of the central stars indicate that most of these objects are massive stars (Wachter et al. (2010); Gvaramadze et al. (2010)). From a selection of these stars we have determined the mass components for the shells as a function of distance by fitting a two component modified black-body function to each of the spectral energy distributions (SED). This is done using data obtained from the *Spitzer* Space Telescope as well as the *Herschel* Space Observatory.

2. Observations

The sample of targets was chosen from two larger samples from Gvaramadze et al. (2010) and Wachter et al. (2010). We have selected 10 targets with the clearest, most easy defined nebulas with at least two detections at the lowest wavelengths (24 μm, 70 μm). The flux densities were obtained using images from *Herschel* observations. The targets were found by a coordinate search in the *Herschel Science Archive* and were all taken using the SPIREPACS mode, which observes with PACS (Photodetector Array Camera and Spectrometer) and SPIRE (Spectral and Photometric Imaging Receiver) instruments in parallel mode. This means that we only have observations in two of the three PACS bands. The data were already processed prior to the analysis using standard pipelines in the *Herschel Interactive Processing Environment* (HIPE).

Each target was observed and measured in images from PACS and SPIRE at 70, 160μm and 250, 350, 500μm, respectively. It is possible to also get an image from PACS at 100 μm but this is not taken in the parallel mode. Most of the targets were only clearly visible at 70μm and to some extent at 160μm. In general there were no clear detections in the SPIRE frames, therefore the results from these are in most cases used as upper limits for a detection. Additionally, a measurement from *Spitzer* in the 24μm band with the MIPS instrument were also done. In Fig. 1 an example of observation is shown of the W:27a in the PACS-70μm and the MIPS-24 μm frame. The circumstellar dust shell is clearly visible in both frames. In the MIPS-24 μm frame one can clearly see a ring structure at the outer bounds of the shell. This is also somewhat visible in the PACS-70 μm frame.

Some of the targets also showed signs of a second larger and more faint shell. These shells have a much more complex structure than the inner circular ones and are harder to distinguish from the background. Surrounding the shells one can see a hint of a cavity (some more clearly than others) which might have been created prior to the ejection of the nebula, as suggested by Vamvatira-Nakou et al. (2013) to be the case of WRAY 15-751.

3. Spectral Energy Distribution (SED)

3.1. Single and Double Component Modified Black-Body Functions

All the targets were found by using the given coordinates (see Table 1) and the dust shells/puffs were identified using DS9. The size and extent of the shells were determined using the Aperture Photometry Tool (APT) where a ring aperture and annulus (in some cases elliptical) were used to find the flux density within the aperture as well as the corresponding uncertainty. An output from APT is shown in Fig. 2. The total flux density from the dust

Table 1: Target List

Target	RA (J2000)	DE (J2000)	Outer Shell?
Gvaramadze			
MN14	14:31:11.00	−61:02:02.1	yes
MN18	15:16:41.00	−58:22:26.0	yes
MN19	15:19:59.90	−57:24:15.2	
MN46	16:43:16.37	−46:00:42.4	
MN64	17:43:59.85	−30:28:38.5	
MN111	19:43:53.19	24:15:31.3	yes
Wachter			
W:5[a]	15:07:56.37	−58:18:23.8	
W:8a[b]	15:33:03.10	−56:12:20.0	yes
W:27a[c]	17:37:47.54	−31:37:33.4	yes
W:43	18:33:39.54	−08:07:08.4	

Notes. List of targets used with their coordinates. It is also noted if there is the presence of a definable outer shell.
[(a)] Also found by Gvaramadze et al. (2010) as MN16. [(b)] Also found by Gvaramadze et al. (2010) as MN21. [(c)] Also found by Gvaramadze et al. (2010) as MN58.

puff were determined using:

$$F_s = N_s(\overline{s}_\mathrm{s} - \overline{s}_\mathrm{bg}) \tag{1}$$

where N_s is the number of pixels within the aperture (the red circle shown in Fig. 2), $\overline{s}_\mathrm{s}$ is the mean flux density value within the aperture and $\overline{s}_\mathrm{bg}$ is the mean flux density from the annulus (marked with green and yellow), hence the background. The flux density is measured in Jy. In some cases, in particular the SPIRE frames, there were no clear detection of the nebula and therefore the same aperture were used throughout all the frames.

Given the flux densities we find the dust masses of the shells by fitting a modified black-body function to the SEDs. The modified black-body function is defined as:

$$F_\nu = \frac{M_\mathrm{d}}{D^2}\kappa B_\nu(T_\mathrm{d}) \tag{2}$$

where F_ν is the flux density at a given frequency ν, M_d is the mass of the dust shell and D is the distance to the object. Since we do not know the distance to most of our targets we have fitted the mass as a function of this. κ is the "dust model" that tells us something about the dust composition and geometry. It is defined as:

$$\kappa = \kappa_{\nu_0}\left(\frac{\nu}{\nu_0}\right)^\beta \tag{3}$$

where κ_ν is the absorption coefficient at the corresponding frequency, ν_0, and β says something about the dust grain's geometry and stuff. The B_ν is the black-body (Planck) function which is a function of the dust temperature T_d:

$$B_\nu(T_\mathrm{d}) = \frac{2h\nu^3}{c^2}\frac{1}{(e^{h\nu/kT_\mathrm{d}} - 1)}. \tag{4}$$

Here, h is the Planck's constant, k is the Boltzmann's constant and c is the speed of light. Initially, we checked whether or not

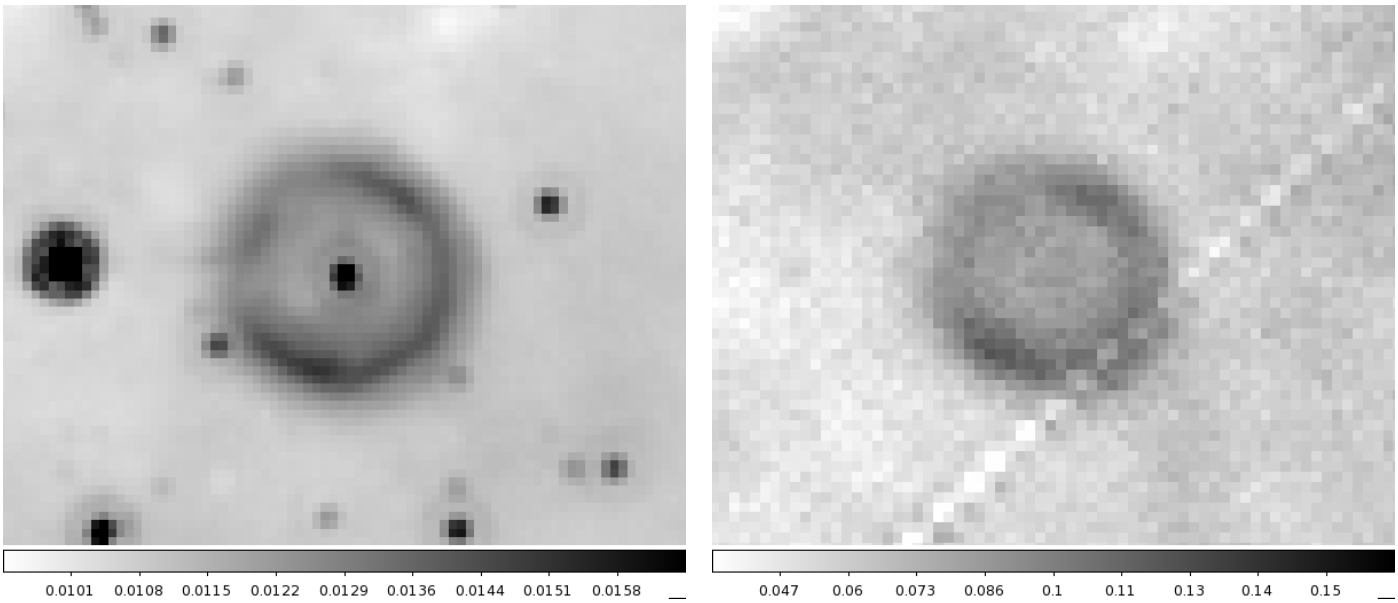

Fig. 1: W:27a shown in the *Spitzer* MIPS μm (left) and *Herschel* PACS-70μm (right) frame. North is up and east is left. The dust shell around the star is clearly visible as well as the ring structure. The ring's inner and outer radius corresponds to 0.53″and 1.01″, respectively. The scale on the bottom is in units of Jy/pixel.

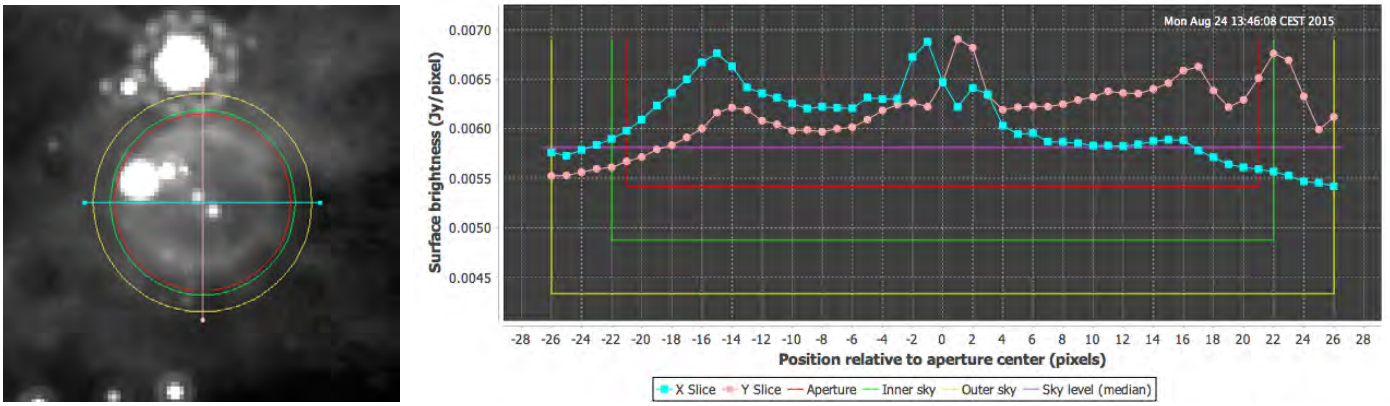

Fig. 2: The location and aperture slice of W8a from APT which is used to determine the extent of the shells. The left figure shows the placement of the aperture and annulus as well as the lines used for the flux counts for the aperture slice (right figure). The red circle/line indicates the aperture and the extent of the shell. The green and yellow indicates the inner and outer radius of the annulus. The radius is given in pixels (1 pixel = 2.45″).

the MIPS24μm points were part of a hotter dust component dominating at lower wavelengths using the fluxes from Gvaramadze et al. (2010) and Wachter et al. (2010). This did not seem to be the case and we omitted the extra points.

In most of our cases a single dust component was not sufficient and we therefore fitted the SEDs with a two-component modified black-body function. This was done by assuming two different dust components, each with its own mass and black-body spectrum (i.e. temperature), though with the same absorption features and chemical composition (i.e. κ). This rewrites eq. 2 to be:

$$F_\nu = \frac{\kappa}{D^2}\,[M_1\,B_\nu(T_1) + M_2\,B_\nu(T_2)] \tag{5}$$

so that $M_1\,B_\nu(T_1)$ is the contribution from the first (warm) dust component and $M_2\,B_\nu(T_2)$ is the contribution from the second (cold) component.

Furthermore, the SEDs has been *bootstrapped* around 12 μm, meaning the flux at this point was limited to $F_{12\,\mu\mathrm{m}} = 0.00 \pm 0.01$ Jy. This was done to prevent the fit from making a "*camel*" rather than the flattening at the top of the SED. This was not done in the cases of MN18 ($F_{12\,\mu\mathrm{m}} = 0.0 \pm 0.1$ Jy), MN64 and W5 because of the single component fit and their relatively warmer dust component.

3.2. Dust Models

Bussoletti et al. (1987a) have determined the extinction efficiencies for different samples of sub-micron amorphous carbon particles and spectroscopically analysed them in the wavelength range 1000AA - 300 μm. In their paper they present an updated version of the data already published from 2000AA to 40 μm(Borghesi et al. 1983, 1985) and new data obtained in the UV/vis (1000 - 3000 AA) and in the FIR (35 AA - 300 μm). The sub-micron amorphous carbon grains were obtained by means of two methods: (1) striking an arc between two amorphous carbon electrodes in a controlled Ar atmosphere at different pressures (samples AC1, AC2 and AC3; where the numbers refer to different accumulation distances from the arc discharge); (2) burning

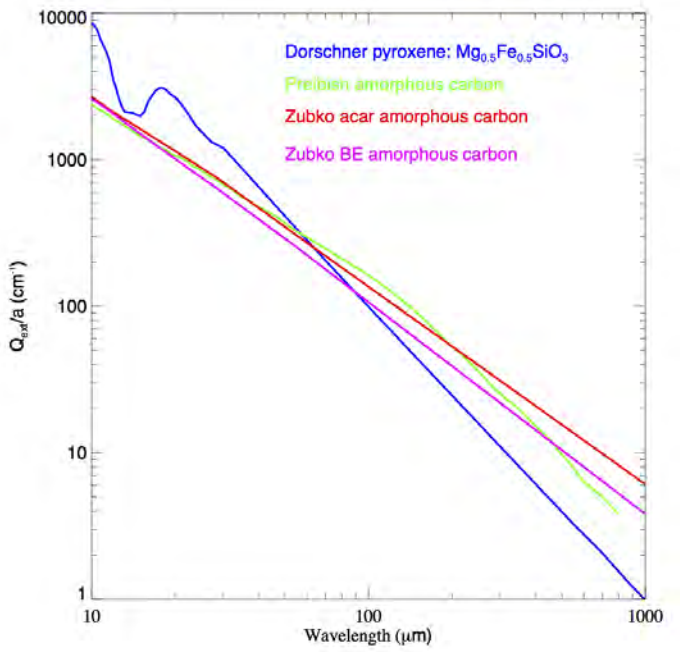

Fig. 3: Extinction of three different amorphous carbon samples (Preibish et al. 1996; Zubko et al. 1998) and silicates (Dorschner et al. 1995). Notice the relative large difference between the different amorphous laboratory samples at long wavelengths.

hydrocarbons (benzene and xylene) in air at room pressure (samples BE and XY). The smoke was collected on quartz substrates. For the UV/vis spectroscopy the quartz substrates on which the particles had been collected were used directly while the dust was scrapped from the substrate and embedded in KBr pellets for the IR spectroscopy. Bussoletti et al. (1987b) suggest that the extinction efficiencies, Qext/a, for the AC samples should be corrected by a factor of 5 due to an experimental underestimation of the pellet density. This correction gives an agreement with the data by Koike et al. (1980).

Colangeli et al. (1995) measured the extinction efficiency in the range 40 nm to 2 mm. They produced three different samples; two by arc discharge between amorphous carbon electrodes in Ar and H2 atmospheres at 10 mbar (sample ACAR and ACH2 respectively) and one by burning benzene in air (sample BE). The samples were deposited onto different substrates for the UV/vis measurements, while in the IR the samples where prepared both on a substrate and by being embedded in KBr/CsI pellets and for the FIR measurements the samples were embedded in polyethylene pellets. These different but overlapping methods gave the possibility of evaluating the difference as a result of embedding the samples in a matrix or by having them on a substrate. Colangeli et al. (1995) found that embedding the samples in a matrix introduces a systematic error (the matrix effect) while the spectra obtained for grains deposited onto a substrate did not suffer from any matrix effect detectable within the accuracy available in the experiment. Therefore the FIR data were corrected for the extinction offset introduced by the matrix.

The laboratorie measurements of Bussoletti et al. (1987a) and Colangeli et al. (1995) have been used to obtain the optical constants n and k of amorphous carbon grains by several authors.

Maron (1990) used the extinction efficiencies of Bussoletti et al. (1987a) (sample AC2) to derive the optical constants (n and k) by estimating the complex permittivity by a combination of the measured absorption efficiencies, dispersion formulae and Kramers-Kronig relation. The reason for performing these calculations is that the optical constants are needed for modelling emission properties of grains containing various allotropic carbons or having different sizes. Maron (1990) is of the opinion that the differences between the primary extinction efficiencies obtained by Bussoletti et al. (1987a) and Koike et al. (1980) are real and caused rather by the use of different electrodes (amorphous carbon and graphite, respectively) than by an underestimation of the pellet column density as suggested by Bussoletti et al. (1987b). Therefore he did not introduce the correction suggested by Bussoletti et al. (1987b).

Rouleau & Martin (1991) used the AC2 and BE data from Bussoletti et al. (1987a) to produce synthetic optical constants (n and k) which satisfy the Kramers-Kronig relations and highlight the effects of assuming various shape distributions and fractal clusters. One of the complications in determining these optical properties of amorphous carbon material was that in the infrared the extinction measurements were done on a sample of submicron-sized particles, while in the visible and ultraviolet the optical constants were obtained by measurements of reflectivity and transmission or by electron energy loss spectroscopy on bulk samples. These diverse measurements were used to produce synthetic optical constants which satisfied the Kramers-Kronig relations.

Preibisch et al. (1993) used the BE sample from Bussoletti et al. (1987a) between 0.1 - 300 μm and the data of Blanco et al. (1991) between 4 - 700 μm, using the same technique as used by Rouleau & Martin (1991) for deriving optical constants taking shape and clustering effects into account. Preibisch et al. (1993) extend the available optical constants on the basis of the measurements of Blanco et al. (1991). With these they determine the opacities of core-mantle-particles with varying mantle thickness and pollution.

Zubko et al. (1996) used the extinction efficiencies obtained by Colangeli et al. (1995) to derive the optical constants (n and k) also by use of the Kramers-Kronig approach. These data were used to evaluate the possible shapes of the amorphous carbon grains in space and the possible clustering of the particles.

4. The Amount of dust

4.1. Inner Shell

Table 2 shows all the flux densities of both the inner and outer shells for each target in the various wavelength frames. Figure 4 shows all the SEDs with their corresponding fits for the inner shells. Some of the targets show more or less sign of a double dust component, i.e. MN14, MN46 and W8a, whereas others only have a single component fit (MN18). For example, since we only have two points on the SED of MN64 and W5 it makes no point in trying to fit a double component. However, it can not be ruled out that it does in fact have one at this point.

In order to prevent fit from fitting with too high temperatures for the warm component, we chose to bootstrap the SEDs around 12 μm, such that $F_{12} = 0.0 \pm 0.01$. Without the bootstrap the temperature of the warm component would be of the order $\sim$ 2000 K, making a "camel" fit instead of a flat-top SED. This, however, was not done for MN14 and MN46, because of the lack of data points. In the case of MN18 $F_{12} = 0.0 \pm 0.1$.

In Table 3 the resulting dust masses from both fits are listed for each target for the inner shell. Since we do not know the distances we list the resulting dust masses for comparison as if

Table 2: Flux densities for inner and outer shells

	MIPS	PACS		SPIRE		
Inner Shell	24μm	70μm	160μm	250μm	350μm	500μm
Target	(Jy)	(Jy)	(Jy)	(Jy)	(Jy)	(Jy)
MN14	0.71±0.11	8.5±1.7	8.7±1.8	2.5±0.7	0.6±0.4	<0.3
MN18	10.5±1.8	9±2	1.7±0.4	0.22±0.11	< 0.12	< 0.05
MN19	0.51±0.08	6.8±1.4	4.4±1.0	< 0.9	< 0.6	0.3
MN46	21±3	60±12	59±12	24±5	9±5	2.1±1.0
MN64	13±2	5±2	...	...	...	...
MN111	5.6±1.0	78±18	61±13	25±4	9.3±1.7	2.54±0.14
W5	6.6±1.0	3.4±0.7	...	...	...	...
W8a	0.84±0.14	7.2±1.8	3.3±1.8	< 5	< 4	< 2
W27a	1.9±0.3	18±4	11±2	1.6±1.4	< 1.7	< 0.5
W43	3.5±0.5	40±8	27±8	9±5	< 7	< 1.8

	PACS		SPIRE		
Outer Shell	70μm	160μm	250μm	350μm	500μm
Target	(Jy)	(Jy)	(Jy)	(Jy)	(Jy)
MN14	45±16	233±51	145±110	< 141	< 65
MN18	61±20	46±18	< 61	< 38	< 22
MN111	< 38	70±28	57±52	< 67	< 36
W8a	< 219	381±250	196±82	< 264	< 139

Notes. The list of targets with their flux densities for the inner shells and for the targets with outer shells. The top part with the inner shells has flux densities in each of the *Herschel* PACS and SPIRE frames as well as the *Spitzer* MIPS-24 frame where as the bottom part with the outer shells only has the ones from *Herschel*.

the targets all have a distance of 5 kpc, such as:

$$M_{5\mathrm{kpc}} = M_{\mathrm{d}} \times \left(\frac{D}{5\,\mathrm{kpc}}\right)^2, \tag{6}$$

where M_d is the mass coefficient obtained from the fit (the sum of the two coefficients in case of a double component fit, even though the warm component contribute significantly less than the cold). The temperature of the two dust components and the size of the inner shell are also noted.

We see that using a silicate-based dust model we get a dust mass corresponding to $3-5$ times greater than when using a carbon-based model, spanning from a few thousandths of a solar mass (i.e. W5 with $M_{5kpc} = 0.0010\,M_\odot$) to a few solar masses (i.e. MN46 with $M_{5kpc} = 2.9\,M_\odot$). The temperatures seem to be fairly consistent with a warm component of about 50-90 K and a cold in the range 20-40 K, though some have rather large uncertainties (warm component of MN19 and the cold component of W8a). The temperatures seem to be slightly higher when using the carbon-model, but within the uncertainties compared to those from the silicate-model.

4.2. Outer Shell

The flux densities for the outer shells are shown in Table 2. The SEDs and their resulting fits for both models are shown in Fig. 5 for each of the four targets. All the SEDs have only been fitted with a single component black-body, since there were no clear signs of an extra component. The models used for these shells are the same as for the inner shells. However, the dust should have had more time to reach, or at least get closer to, a state of equilibrium with a more similar temperature for the two dust components. The resulting dust mass and temperature from both the fits are shown in table 4

Here we also see a significantly higher dust mass when using the silicate-based model and a slightly higher temperature when using the carbon-based. The temperature are also lower compared to the cold dust component of the inner shell as should be expected. Although there is an exception with W8a, but this target has rather large uncertainties on the temperatures of the inner shell. The dust masses obtained from the silicate-based model are quite high for most of the targets. This could indicate that we are overshooting the distance when setting it to 5 kpc. It could also be a result of poor background subtraction, since it was sometimes difficult to distinguish the outer shells' emission from the general background emission. However, the fit using the carbon-based model yields more reasonable results for the masses in the range 0.3-8 $M_\odot$. Overall there is a difference of a factor ~3 between the dust masses from the two models.

5. Significant or negligible?

5.1. The single star

In general the fits are just, or barely, constrained by the number of data points. But the greatest uncertainty on the deduced dust masses is still the unknown distances to the objects, since the dust mass scales as $\propto D^2$. In general the fits are just, or barely, constrained by the number of data points (4 parameters vs. 6 data points, in most of the cases). In the case of MN64 and W5, which only have 2 points, these can of course be fitted with anything. They have therefore only been fitted with a sin-

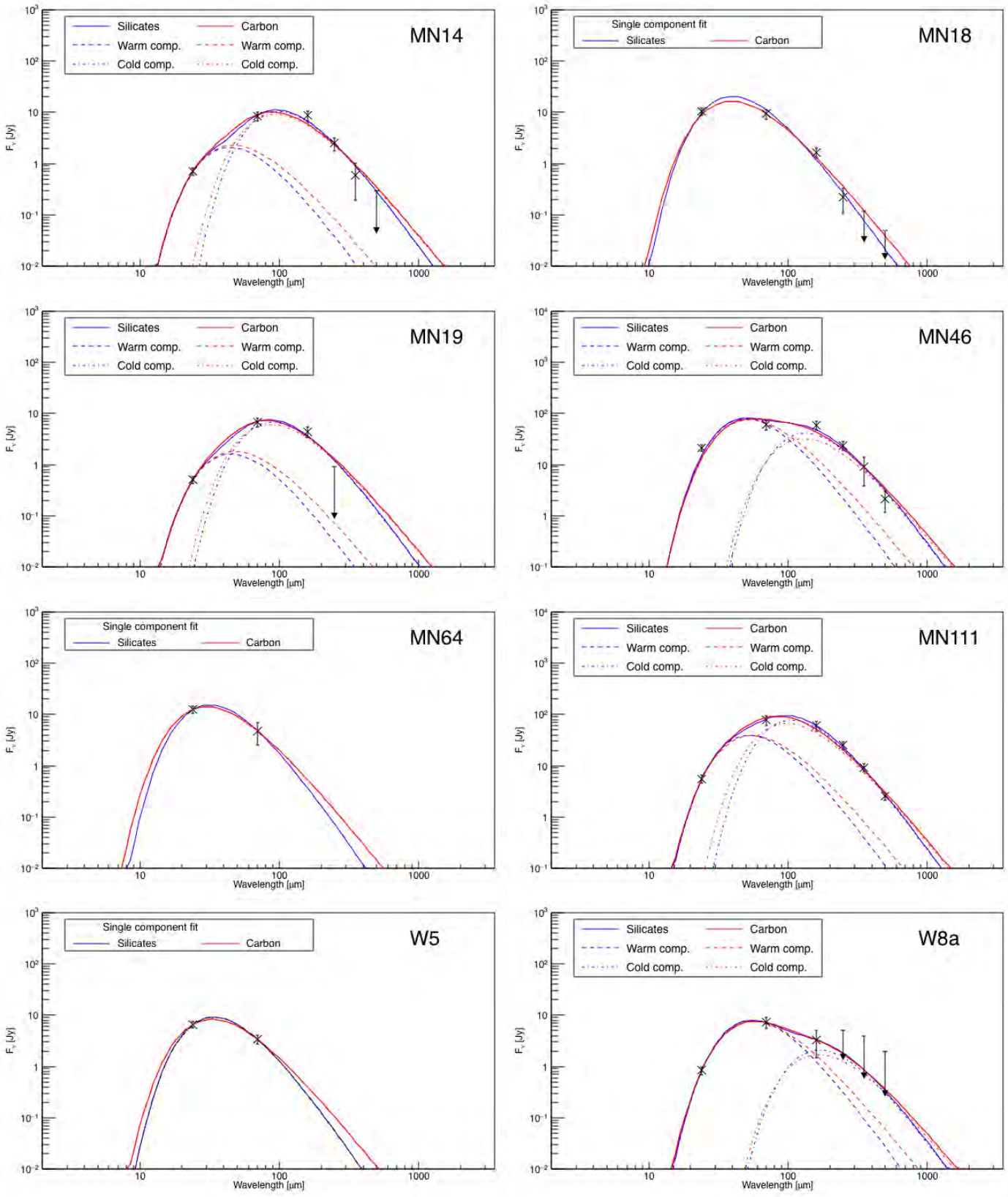

Fig. 4: SEDs fittet with a modified black-body function. Each SED is fitted with black-body functions based on two different dust models. The blue lines are corresponds to the fit using the silicate-model, whereas the red are for the carbon-model. The dashed and the dash-dotted lines show the contribution from the warm and cold dust component, respectively. Upper limits are indicated with arrows. MN18, MN64 and W5 are fitted using only a single dust component. The target name is noted in the upper right corner on each plot. Note that MN111 and MN46 has slightly different flux scales than the others.

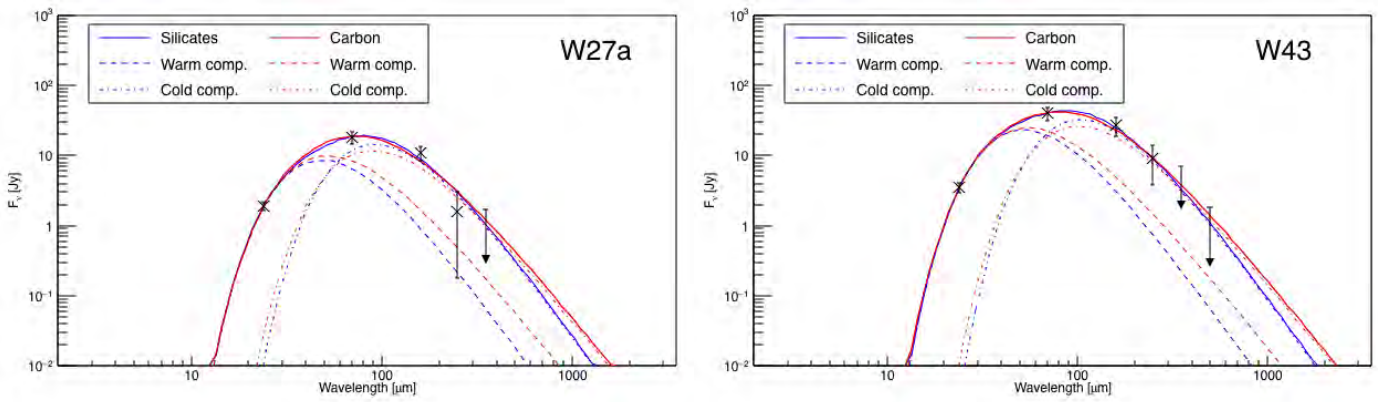

Fig. 4: *– Continued.*

Table 3: Inner shell dust masses and temperatures

Model:		Silicates[a]			Carbon[b]		
Target	Size	$M_{5\,kpc}$	T_w	T_c	$M_{5\,kpc}$	T_w	T_c
	($''$)	($M_\odot$)	(K)	(K)	($M_\odot$)	(K)	(K)
MN14	36.75×49	0.16	67 ± 18	30 ± 2	0.04	70 ± 17	35 ± 3
MN18[c]	34.94×24.5	0.004	73 ± 3	–	0.0014	83 ± 3	–
MN19	31.85	0.06	65 ± 34	33 ± 5	0.018	68 ± 38	38 ± 8
MN46	66.15	2.9	59.1 ± 1.5	22 ± 2	0.6	62.4 ± 1.7	25 ± 3
MN64[c]	61.25	0.0012	90 ± 11	–	4×10^{-4}	108 ± 16	–
MN111	21.9	1.7	56 ± 7	28 ± 3	0.3	60 ± 7	34 ± 4
W5[c]	41.1	0.0010	84 ± 5	–	3×10^{-4}	99 ± 7	–
W8a	51.45	0.5	53 ± 3	17 ± 17	0.09	58 ± 3	20 ± 26
W27a	46.55	0.16	61 ± 13	32 ± 5	0.04	63 ± 13	37 ± 9
W43	51.0	0.6	56 ± 11	28 ± 7	0.17	60 ± 10	32 ± 9

Notes. The fit results from both dust models. The dust masses has been calculated assuming a distance of 5 kpc. The 2nd column indicates the size of the shell.
[(a)] Model based on a Silicate-composition with parameters: $\nu_0 = 70\,\mu$m, $\kappa_{\nu_0} = 5.0\,m^2\,kg^{-1}$ and $\beta = 1.95$.
[(b)] Model based on a Carbon-composition with parameters: $\nu_0 = 20\,\mu$m, $\kappa_{\nu_0} = 45.0\,m^2\,kg^{-1}$ and $\beta = 1.45$.
[(c)] Single dust component fit.

Table 4: Outer shell dust masses and temperatures

Model[a] :	Silicates		Carbon	
Target	$M_{5\,kpc}$	T	$M_{5\,kpc}$	T
	($M_\odot$)	(K)	($M_\odot$)	(K)
MN14	25	20.1 ± 1.4	8	21.9 ± 1.6
MN18	1	31 ± 4	0.3	35 ± 6
MN111	8	20 ± 5	2	22 ± 5
W8a	29	22 ± 3	8	24 ± 4

Notes. [(a)] The models used are the same as for the inner shell. See text or table 3.

gle dust component. When looking at the SEDs it can be seen that both their MIPS-24 μm points lie above their PACS-70 μm which could indicate that this in fact is the cold dust component, though slightly hotter than compared to the other targets'. Since the majority of the dust mass is found in the cold component, these can be seen as upper limits to the dust mass. The last case where a single component has been used is MN18. This target also have comparable values of fluxes at 24 and 70 μm which could also indicate a hotter cold component.

As mentioned earlier, the bootstrapping was done to prevent the warm component from being fitted with a too high temperature, creating the so-called "camel" fit. The effect of the bootstrap means that the warm component gets a lower temperature and hence also a higher mass coefficient than otherwise. However, the mass contribution from the warm component are about 3 orders of magnitude lower than that of the cold component. One could have fitted the SEDs with an additional component, but this would only introduce even more parameters to an already poorly constrained fit. Omitting the bootstrap would also cause the aforementioned temperature bias on the cold component, which would result in a significantly lower dust mass.

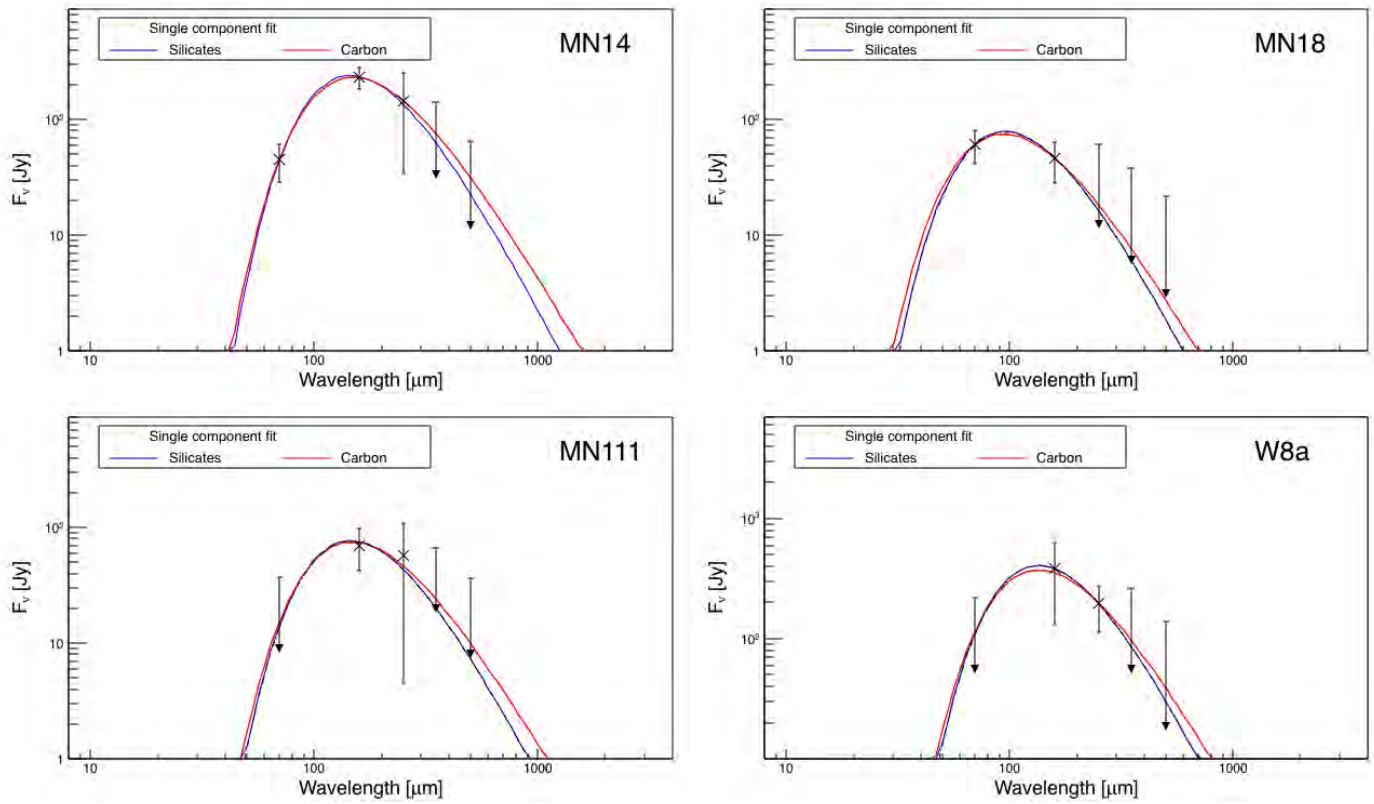

Fig. 5: The SEDs for the outer shells fitted with both the silicate- (blue line) and the carbon-based (red line) dust models. The fit consists only of one dust component. The target name is shown in the upper right corner. Arrows indicate upper limits. Please note that W8a has a slightly different flux scale.

5.2. IMF and Number of High-mass Stars

6. Conclusions

Summarize results. Does it explain the amount of dust in the MW?

Acknowledgements. Special thanks to everybody.

References

Gvaramadze, V. V., Kniazev, A. Y., & Fabrika, S. 2010, MNRAS, 405, 1047
Hirashita, H. & Ferrara, A. 2002, MNRAS, 337, 921
Schneider, R., Ferrara, A., & Salvaterra, R. 2004, MNRAS, 351, 1379
Vamvatira-Nakou, C., Hutsemékers, D., Royer, P., et al. 2013, A&A, 557, A20
Wachter, S., Mauerhan, J. C., Van Dyk, S. D., et al. 2010, AJ, 139, 2330

References

Agliozzo, C., Noriega-Crespo, A., Umana, G., Flagey, N., Buemi, C., Ingallinera, A., Trigilio, C., and Leto, P. (2014). The candidate luminous blue variable G79.29+0.46: a comprehensive study of its ejecta through a multiwavelength analysis. *MNRAS*, 440:1391–1409.

Andersen, A. C., Höfner, S., and Gautschy-Loidl, R. (2003). Dust formation in winds of long-period variables. V. The influence of micro-physical dust properties in carbon stars. *Astronomy and Astrophysics*, 400:981–992.

Bertoldi, F., Carilli, C. L., Cox, P., Fan, X., Strauss, M. A., Beelen, A., Omont, A., and Zylka, R. (2003). Dust emission from the most distant quasars. *Astronomy and Astrophysics*, 406:L55–L58.

Bianchi, S. and Schneider, R. (2007). Dust formation and survival in supernova ejecta. *MNRAS*, 378:973–982.

Bohren, C. F. and Huffman, D. R. (1983). *Absorption and Scattering of Light by Small Particles*. New York: Wiley.

Christensen-Dalsgaard, J. (2008). *Stellar Structure and Evolution*.

Dorschner, J., Begemann, B., Henning, T., Jaeger, C., and Mutschke, H. (1995). Steps toward interstellar silicate mineralogy. II. Study of Mg-Fe-silicate glasses of variable composition. *Astronomy and Astrophysics*, 300:503.

Draine, B. (2011). *Physics of the Interstellar and Intergalactic Medium*. Princeton Series in Astrophysics. Princeton University Press.

Dunne, L., Eales, S., Ivison, R., Morgan, H., and Edmunds, M. (2003). Type II supernovae as a significant source of interstellar dust. *Nature*, 424:285–287.

Gall, C., Hjorth, J., and Andersen, A. C. (2011). Production of dust by massive stars at high redshift. *Astronomy and Astrophysics Review*, 19:43.

Guha Niyogi, S., Min, M., Meixner, M., Waters, L. B. F. M., Seale, J., and Tielens, A. G. G. M. (2014). Dust composition and mass-loss return from the luminous blue variable R71 in the LMC. *Astronomy and Astrophysics*, 569:A80.

Gvaramadze, V. V., Kniazev, A. Y., and Fabrika, S. (2010). Revealing evolved massive stars with Spitzer. *MNRAS*, 405:1047–1060.

Indebetouw, R., Matsuura, M., Dwek, E., Zanardo, G., Barlow, M. J., Baes, M., Bouchet, P., Burrows, D. N., Chevalier, R., Clayton, G. C., Fransson, C., Gaensler, B., Kirshner, R., Lakićević, M., Long, K. S., Lundqvist, P., Martí-Vidal, I., Marcaide, J., McCray, R., Meixner, M., Ng, C.-Y., Park, S., Sonneborn, G., Staveley-Smith, L., Vlahakis, C., and van Loon, J. (2014). Dust Production and Particle Acceleration in Supernova 1987A Revealed with ALMA. *The Astrophysical Journal Letters*, 782:L2.

Lakićević, M., van Loon, J. T., Meixner, M., Gordon, K., Bot, C., Roman-Duval, J., Babler, B., Bolatto, A., Engelbracht, C., Filipović, M., Hony, S., Indebetouw, R., Misselt, K., Montiel, E., Okumura, K., Panuzzo, P., Patat, F., Sauvage, M., Seale, J., Sonneborn, G., Temim, T., Urošević, D., and Zanardo, G. (2015). The Influence of Supernova Remnants on the Interstellar Medium in the Large Magellanic Cloud Seen at 20-600 μm Wavelengths. *The Astrophysical Journal*, 799:50.

Lau, R. M., Herter, T. L., Morris, M. R., Li, Z., and Adams, J. D. (2015). Old supernova dust factory revealed at the Galactic center. *Science*, 348:413–418.

Longair, M. S. (2011). *High Energy Astrophysics*.

Maiolino, R., Schneider, R., Oliva, E., Bianchi, S., Ferrara, A., Mannucci, F., Pedani, M., and Roca Sogorb, M. (2004). A supernova origin for dust in a high-redshift quasar. *Nature*, 431:533–535.

Massey, P. (2013). Massive stars in the galaxies of the Local Group. *New Astronomy Reviews*, 57:14–27.

Matsuura, M., Dwek, E., Meixner, M., Otsuka, M., Babler, B., Barlow, M. J., Roman-Duval, J., Engelbracht, C., Sandstrom, K., Lakićević, M., van Loon, J. T., Sonneborn, G., Clayton, G. C., Long, K. S., Lundqvist, P., Nozawa, T., Gordon, K. D., Hony, S.,

Panuzzo, P., Okumura, K., Misselt, K. A., Montiel, E., and Sauvage, M. (2011). Herschel Detects a Massive Dust Reservoir in Supernova 1987A. *Science*, 333:1258.

Mauerhan, J. C., Smith, N., Filippenko, A. V., Blanchard, K. B., Blanchard, P. K., Casper, C. F. E., Cenko, S. B., Clubb, K. I., Cohen, D. P., Fuller, K. L., Li, G. Z., and Silverman, J. M. (2013). The unprecedented 2012 outburst of SN 2009ip: a luminous blue variable star becomes a true supernova. *MNRAS*, 430:1801–1810.

Mečina, M., Kerschbaum, F., Groenewegen, M. A. T., Ottensamer, R., Blommaert, J. A. D. L., Mayer, A., Decin, L., Luntzer, A., Vandenbussche, B., Posch, T., and Waelkens, C. (2014). Dusty shells surrounding the carbon variables S Scuti and RT Capricorni. *Astronomy and Astrophysics*, 566:A69.

Nozawa, T., Kozasa, T., Habe, A., Dwek, E., Umeda, H., Tominaga, N., Maeda, K., and Nomoto, K. (2007). Evolution of Dust in Primordial Supernova Remnants: Can Dust Grains Formed in the Ejecta Survive and Be Injected into the Early Interstellar Medium? *Astrophysical Journal*, 666:955–966.

Owocki, S. (2000). *Radiatively Driven Stellar Winds from Hot Stars*.

Preibisch, T., Ossenkopf, V., Yorke, H. W., and Henning, T. (1993). The influence of ice-coated grains on protostellar spectra. *Astronomy and Astrophysics*, 279:577–588.

Prialnik, D. (2011). *An Introduction to the Theory of Stellar Structure and Evolution*. Cambridge University Press.

Salamanca, I., Terlevich, R. J., and Tenorio-Tagle, G. (2002). The circumstellar material around SN IIn 1997eg: another detection of a very narrow P Cygni profile. *MNRAS*, 330:844–854.

Smith, N. (2014). Mass Loss: Its Effect on the Evolution and Fate of High-Mass Stars. 52:487–528.

Smith, N., Gehrz, R. D., Hinz, P. M., Hoffmann, W. F., Hora, J. L., Mamajek, E. E., and Meyer, M. R. (2003). Mass and Kinetic Energy of the Homunculus Nebula around η Carinae. *The Astrophysical Journal*, 125:1458–1466.

Vamvatira-Nakou, C., Hutsemékers, D., Royer, P., Nazé, Y., Magain, P., Exter, K., Waelkens, C., and Groenewegen, M. A. T. (2013). Herschel imaging and spectroscopy of the nebula around the luminous blue variable star WRAY 15-751. *Astronomy and Astrophysics*, 557:A20.

Van de Steene, G. C., van Hoof, P. A. M., Exter, K. M., Barlow, M. J., Cernicharo, J., Etxaluze, M., Gear, W. K., Goicoechea, J. R., Gomez, H. L., Groenewegen, M. A. T., Hargrave, P. C., Ivison, R. J., Leeks, S. J., Lim, T. L., Matsuura, M., Olofsson, G., Polehampton, E. T., Swinyard, B. M., Ueta, T., Van Winckel, H., Waelkens, C., and Wesson, R. (2015). Herschel imaging of the dust in the Helix nebula (NGC 7293). *Astronomy and Astrophysics*, 574:A134.

Wachter, S., Mauerhan, J. C., Van Dyk, S. D., Hoard, D. W., Kafka, S., and Morris, P. W. (2010). A Hidden Population of Massive Stars with Circumstellar Shells Discovered with the Spitzer Space Telescope. *The Astrophysical Journal*, 139:2330–2346.

Zubko, V. G., Mennella, V., Colangeli, L., and Bussoletti, E. (1996). Optical constants of cosmic carbon analogue grains - I. Simulation of clustering by a modified continuous distribution of ellipsoids. *MNRAS*, 282:1321–1329.

UNIVERSITY OF COPENHAGEN
FACULTY OF SCIENCE